

A Baroclinic Teleconnection Between the Mozambique Channel and the Makassar Strait

Robby B. C. Huijting¹
Utrecht University

14th July, 2016

Abstract

The Mozambique Channel and the Makassar Strait are very important for the large scale circulation in the Indian Ocean and the water and climate signal exchange between the Indian Ocean and its surrounding oceans. Up to 2004, very little long-term data on transport was available, so it was unknown how it varies and how it is driven. In order to get this data, the LOCO (Mozambique) and INSTANT (Makassar) mooring networks were installed. The data answered many questions, but also brought in new questions. One of these questions is why the Mozambique Channel transport transits from low net and highly variable transport to high net and little varying transport in May 2006. A second question is why at Makassar Strait similar changes occurred in July 2006 and, even though the general flow direction in the Indian Ocean is westward, why the Mozambique Channel transport transits earlier than the transport through Makassar Strait. A Sverdrup model on the flow around an island shows that changing wind patterns can play a role. The velocity field is analysed for the case that wind is blowing over the full ocean, only over the western half and only over the eastern half. For the case that wind stress acts on the entire ocean surface, the velocity field is analysed for different choices of the latitude of minimum wind curl. By analysing data, the influence of the Indian Ocean Dipole and El Nino Southern Oscillation on the wind, the position of the Indian Ocean Subtropical Gyre, the South Equatorial Current and the sea level is investigated. From this, it is found that the transports are significantly determined by equatorial dynamics rather than by the local wind patterns near the Mozambique Channel and Makassar Strait.



Night view of the Indian Ocean in 2012 derived from Suomi NPP satellite data. The Mozambique Channel lies between Mozambique and Madagascar. The Makassar Strait is part of the East Indian Archipelago. Figure adapted from [NASA Earth Observatory/NOAA NGDC](https://www.nasa.gov/content/300920main/indian_ocean_night_view_2012).

¹ Student number: 3692205; supervised by Prof. Dr. W.P.M. de Ruijter, Dr. A.S. von der Heydt and Dr. W. Ridderinkhof

Contents

1. Introduction.....	1
2. Approach.....	5
2.1.Elementary models of the ocean circulation.....	6
2.1.1. Sverdrup balance.....	6
2.1.2. Stommel boundary layer.....	9
2.1.3. General effects of an island on ocean flow.....	10
2.1.4. Baroclinic flow around an island: Island Rule.....	12
2.2.Mechanism for changes in wind-induced transport.....	15
3. Applications.....	19
3.1 Data.....	19
3.2 Methods.....	22
4. Results.....	26
4.1 Transition of the Indian Ocean Dipole.....	26
4.2 Position of the South Equatorial Current.....	27
4.3 Position of the Tropical Gyre and the Subtropical Gyre.....	30
4.4 Sea surface temperature and sea surface wind.....	33
4.5 Kelvin waves: barotropic mode versus baroclinic mode.....	39
4.6 Evolution of the sea level anomalies.....	40
4.7 Model results on baroclinic flow around an island.....	43
5. Conclusions.....	47
6. Discussion.....	49
6.1 Island Rule and wind stress observations.....	49
6.2 Timespan of LOCO and INSTANT.....	51
Appendix.....	52
A. Derivation of the free boundary layer solutions.....	52
B. Madden-Julian Oscillation and equatorial Kelvin wave dynamics.....	54
C. Island Rule applied to wind stress observations.....	57
Acknowledgements.....	61

References.....	63
-----------------	----

1. Introduction

The Indian Ocean is one of the five major oceans on Earth. To the north it is shielded by Asia, to the west by Africa, to the east by the East Indian Archipelago and Australia and finally to the south by the Southern Ocean. The Indian Ocean is a gateway for trade and a vital habitat for all kinds of living creatures. No less relevant, due to its central position between the world oceans, the Indian Ocean also forms an important link in the climate signal distribution over and transport between the Pacific Ocean, Atlantic Ocean and the Southern Ocean. The Indian Ocean is in turn strongly influenced by oceanic and atmospheric climate signals received directly or indirectly from these neighbouring oceans. This paper will discuss how the Indian Ocean circulation is connected to large scale phenomena both within the Indian Ocean itself and surrounding areas.

In order to gain a better understanding on the role of the Indian Ocean and other oceans in the climate system, observations of their properties have to be collected and analysed. Observations can be obtained in situ and by remote sensing. The spatial resolution of long-term datasets obtained with satellites has increased since their first use for ocean monitoring in 1978 (Dijkstra, 2008; Jin *et al.*, 2011; Le Traon, 2013). The coverage and resolution of in situ observations have grown slower than those of the remote sensing (Li *et al.*, 2006; Legler *et al.*, 2015). The ARGO worldwide mooring network, for example, which both functions as a long-term and high spatial resolution in situ monitoring tool, only exists since 2004 (Gould *et al.*, 2004).

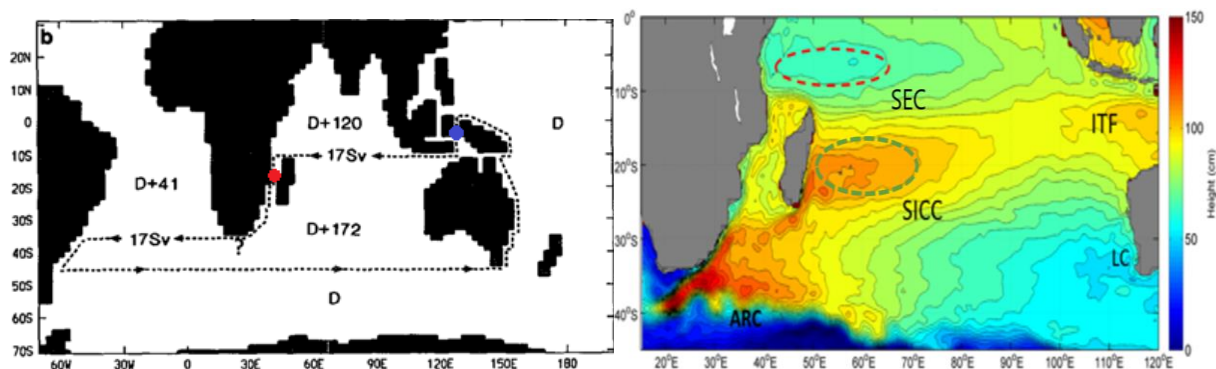


Figure 1 (left) Model of the Sverdrup Indonesian Throughflow (ITF) pathway adapted from Hirst and Godfrey (1989) in a longitude versus latitude frame. The ITF pathway is part of the global thermohaline circulation. D stands for the average streamfunction value. The comments ' $D + \Delta$ ' and ' $D - \Delta$ ' indicate the difference Δ to the mean value D . The red dot indicates the location of the LOCO moorings, the blue dot that of the INSTANT moorings. (right) Long-term mean of the absolute dynamic topography in the southern Indian Ocean in a longitude versus latitude frame. Each contour represents a constant absolute dynamic topography value. The figure is created by combining data of the KNMI Atlas (1951), the Wyrski Atlas (1971) and Palastanga *et al.* (2007). Indicated are the Tropical Gyre (red dotted oval) and Subtropical Gyre (green dotted oval), the Indonesian Throughflow (ITF), South Equatorial Current (SEC), Agulhas Return Current (ARC), South Indian Counter Current (SICC) and the Leeuwin Current (LC). From Makassar Strait, Indonesian Throughflow water enters the Indian Ocean and crosses it as the South Equatorial Current (SEC) to reach Madagascar. The SEC is also the boundary between the Tropical Gyre and the Subtropical Gyre.

At the same time as ARGO was installed, scientists looked for other strategic locations in the world oceans to monitor the large-scale ocean circulation. For choosing these locations, current

knowledge on the inter-oceanic flow structure from observations and models was used. Both models and observations had shown that Makassar Strait (MS) is the most important path of the Indonesian Throughflow (ITF) (Figure 1, left panel). The ITF is a substantial amount of Pacific Ocean water that passes the MS and enters the Indian Ocean via the Lombok Strait, the Ombai Strait and the Timor Strait (Sprintall *et al.*, 2004). The ITF brings in climatic signals of the western Pacific Ocean (e.g., El Nino-Southern Oscillation, Australian monsoon (Feng and Wijffels, 2001)) and forms a freshwater input into the Indian Ocean. This meridional input feeds the meridional flowing South Equatorial Current (SEC), which runs between the clockwise rotating Seychelles Chagos Tropical Gyre, shortly Tropical Gyre, and the anticlockwise rotating Subtropical Gyre. The SEC carries the ITF water towards Madagascar (see both panels of Figure 1), where the water can either follow the eastern coast of Madagascar, pass the island and flow northward along the African coast or tip the island and enter the Mozambique Channel (MC).

The Mozambique Channel was already known to be an waterway in the western boundary of the wind-driven gyre system in the Indian Ocean (Figure 1, right panel). At inter-oceanic scale, people already knew that the channel is a limb of the large-scale ocean overturning circulation system (Figure 1, left panel). The MC transport merges into Agulhas leakage and Agulhas retroflection, which influence the dynamics in the neighbouring Atlantic Ocean and the dynamics in locally in the Indian Ocean, respectively. The Agulhas leakage is warm and salty water entering the South Atlantic, which reinforces the strength and stability of the Atlantic Meridional Overturning Circulation and associated Atlantic climate when mixing up with Atlantic Ocean water (Weijer *et al.*, 1999). The Agulhas retroflection is Indian Ocean water connecting to the large network of connected subtropical gyres in the south Atlantic-Indian-Pacific Oceans (De Ruijter, 1982; Ridgeway and Dunn, 2007; Beal *et al.*, 2011).

At the beginning of the 21st century, estimates of the ITF and its variability are within a wide range due to its strong variability and lack of sustained observations (Sprintall *et al.*, 2004). At the same time, observations had a too short temporal range to tell the fate of ITF transported westward by the South Equatorial Current when reaching Madagascar. It could either tip the northern edge of Madagascar to feed the Mozambique Channel transport, or feed the currents along the eastern coast of Madagascar or the African continent. Indirect estimates from the wind patterns and the difference between the ITF and transports by the currents along East Madagascar show wide variability, making it difficult to derive an estimate of the Mozambique Channel transport (De Ruijter *et al.*, 2002; Sprintall *et al.*, 2004).

Due to their important role within the global thermohaline circulation and the large uncertainty on the seasonal mean and the variability of their throughflow, it was decided to install mooring networks that can monitor the transport properties of the MC and the MS. The network in the MC, spanning the narrow part of the MC at 17°S (Figure 1, red dot in the left panel), is part of the Dutch Long-term Ocean Climate Observations (LOCO) project (Van Haren, 2003; De Ruijter *et al.*, 2006). In the MS, situated at its lower part at 3°S (Figure 1, blue dot in the left panel), two moorings were placed as part of the International Nusantara Stratification And Transport (INSTANT) program (Sprintall *et al.*, 2004).

Since the beginning of LOCO MC and INSTANT MS networks, a wealth of new insights has been gained on both the Indonesian Throughflow and the flow through the Mozambique Channel. For example, the mean and variability of the transport (MS: Schiller *et al.*, 2008; Gordon *et al.*, 2012; MC: Ullgren *et al.*, 2012), the reducing and enhancing effects of eddy kinetics on mixing and the general flow pattern (MS: Shinoda *et al.*, 2012; MC: Palastanga *et al.*, 2006; Ternon *et al.*, 2013), the stagnating and accelerating effects of hydrography on along-channel flow (MS: Gordon *et al.*, 2008; MC: Ullgren *et al.*, 2012), and the combined influence of planetary waves dynamics (MS: Pujiana *et al.*, 2013; MC: Harlander *et al.*, 2009), wind forcing (MS: Schiller *et al.*, 2010; MC: Ternon *et al.*, 2014) and variability of the thermocline (MS: Pujiana *et al.*, 2009; MC: Van der Werf *et al.*, 2009) on the variability of the throughflow are much more understood than 12 years ago.

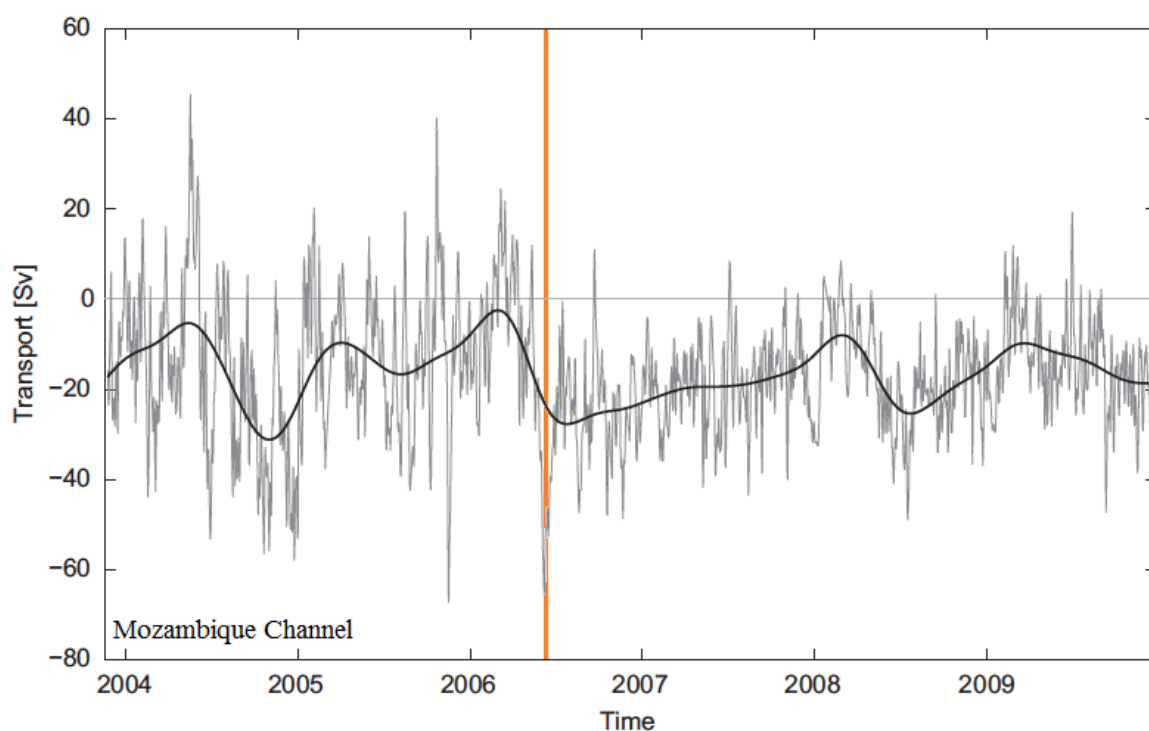


Figure 2 Volume transport through the Mozambique Channel calculated from mooring data via different inter- and extrapolation models. The thin line shows the raw transport data. The thick solid line indicates the same signal, now filtered by a low frequency filter with a 210 days cut-off. The orange line indicates when the transport in the Mozambique Channel approximately transits to a new state with increased southward transport and less variability. Figure adapted from Ullgren *et al.* (2012).

Yet, there still are many questions unanswered about some of the properties of the throughflows of the Mozambique Channel and that of Makassar Strait. The total transport as a function of time through the Mozambique Channel, derived from the LOCO mooring data by Ullgren *et al.* (2012), is shown in Figure 2. The transport signal curve can be divided into two periods. Between 2003 and May 2006, the net transport varies a lot, but the mean transport is small. After May 2006, the variation of the transport is significantly reduced, but the mean transport has increased (Ridderinkhof *et al.* (2010) report values of -13.6 Sv between November 2003

and March 2006 and -20.6 Sv between March 2006 and January 2008; as Ullgren *et al.* (20102), they only mention an exact number on the variability for the entire observation period, which is $\pm 3.1\text{ Sv}$). This lead to the first research question for this thesis:

1. *What caused the sudden transition of the Mozambique Channel transport signal from one with a small mean and large variability to one with a large mean and small variability?*

Figure 3 shows the along-channel flow velocity anomalies in Makassar Strait. It is derived from the INSTANT mooring velocity data by removing the seasonal signal followed by filtering the residual by a seven months running mean. Negative (positive) anomalies represent enhanced (decreased) southward transport. From 2004 to 2006, the anomalies are derived from data from a mooring at the western side of the Makassar Strait and one at the eastern side. The trend after 2006 is calculated from data from the western mooring only since the eastern mooring has been removed in 2006. Figure 3 also shows a transition from positive velocity anomalies to negative anomalies, so from little southward transport to more southward transport, around July 2006. Around March 2008, another transition occurs to more southward flow. The increase of along channel southward depth-integrated velocity between 2006 and 2008 is about 19% of the mean southward depth-integrated along channel velocity between 2004 and 2006 (Gordon *et al.*, 2012).

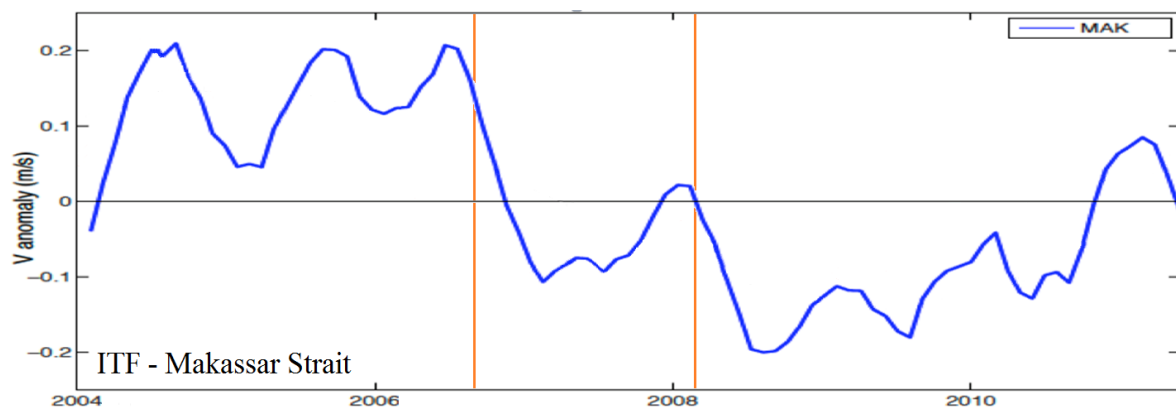


Figure 3 Along strait velocity anomalies for Makassar Strait (MAK) derived from INSTANT data. This graph is obtained by subtracting the seasonal signal from the total along channel flow velocity, after which a 7 months running mean is applied to the residual. The orange lines indicates when the transport in the Makassar Strait approximately transits to a new state with increased mean southward transports. Figure adapted from Gordon *et al.*, 2012.

The effects of the changes in transport are significant, as can be seen in, for example, the large decline in sea surface salinity in the eastern Indian Ocean after the second half of 2006 (see Figure 4; data provided by Andrea Storto (C-GLORS reanalysis; Storto *et al.*, 2015). Although the system tends to return to the former sea surface salinity state, the Indian Ocean seems to have permanently transitioned to a new state after 2006.

For the ITF, the transport transition is about three months after that within the Mozambique Channel. Since the transport of Indo-Pacific water is directed from east to west, it is odd that

the changes first occur in the west and then in the east. The observed similar but time-lagged trend transition in Mozambique Channel volume transport and Makassar Strait along strait flow velocity brings up the second research question:

2. *Are the transport through the Mozambique Channel and the Indonesian Throughflow dynamically connected? If so, how, and what are the main transport and information pathways?*

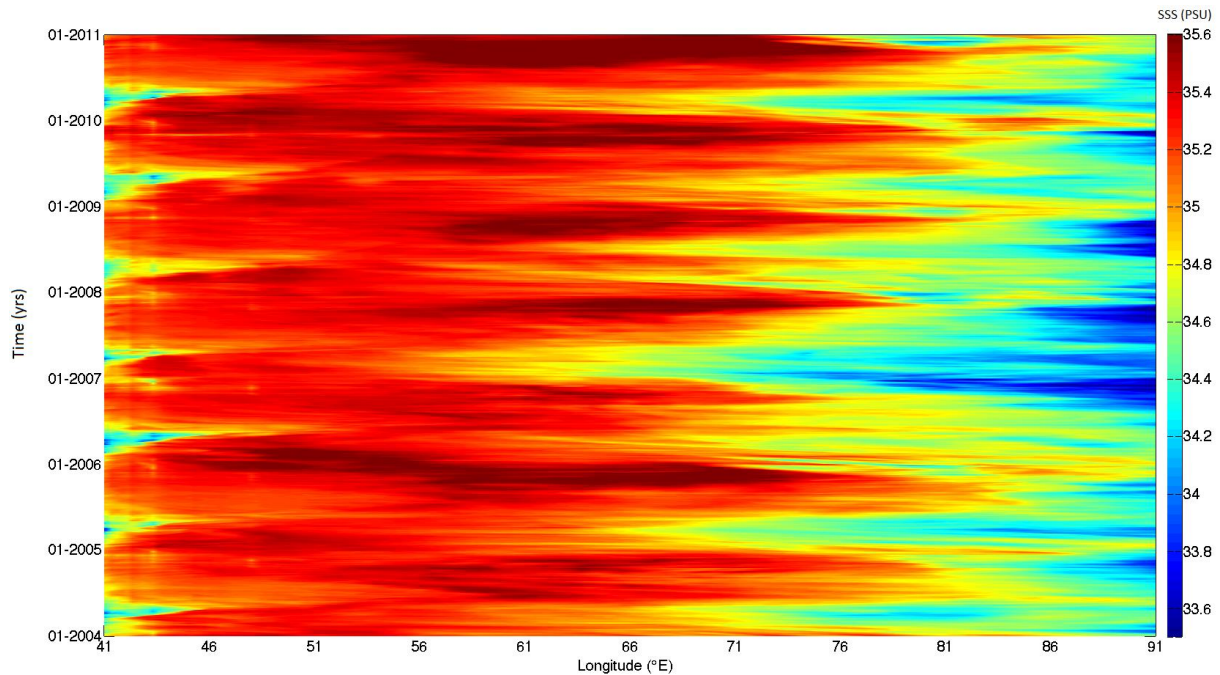


Figure 4 C-GLORS reanalysis sea surface salinity for the period 2004-2011 in practical salinity units (PSU). An increased intrusion of fresh water from the Pacific into the Indian Ocean from 2006 and onwards is clearly visible. This freshening of the eastern Indian Ocean is a clear representation of the increased MS transport.

2. Approach

To find out what causes the flow transitions, it must first be clear what drives the flow in situations like those at Mozambique Channel and Makassar Strait in the first place. The flow through the MC and MS are characterized as flow in an ocean basin which contains a large island (Madagascar at the MC and Australia at the MS). The addition of an island to an ocean basin makes the basin multiply connected. To determine the transport thus created through a channel or strait, one needs an extra criterion. That is the Island Rule.

In Section 2.1, some elementary models on the ocean circulation will be discussed. First, the Sverdrup balance (Section 2.1.1) and Stommel solution for the western boundary layer (Section 2.1.2) will be presented. Then, the flow around an island will be described in contrast to that in an ocean without an island (Section 2.1.3). Finally, an important feature of wind-induced flow around an island will be discussed: the Island Rule (Section 2.1.4).

Section 2.2 is dedicated to a dynamic system to explain the changes in the Mozambique Channel transport and Makassar Strait transport. Important factors will be the Indian Ocean Dipole and the El Nino – Southern Oscillation, sea surface winds, planetary wave dynamics and the double gyre structure of the southern Indian Ocean.

2.1 Elementary models of the ocean circulation

The large scale ocean flow in first order approximation can be split into an inner ocean circulation regime and a western boundary layer where a return current is present that closes the circulation. The flow in these regimes will be described in the following two subsections. After that, two subsections will be on the flow around an island. It will be compared to flow in a basin without islands and an analytical first order representation for the streamfunction will be given for flow around islands.

2.1.1 Sverdrup balance

To first approximation, large-scale flows in ocean basins are baroclinic and non-stationary. But we first present the asymptotic barotropic β -plane model solutions valid for a constant density ocean with small Rossby number ϵ (ratio of timescales on which inertial effects and the Coriolis force vary). The interior ocean is dominated by the hydrostatic and geostrophic balance. The pressure field evolution occurs due to a balance of ageostrophic effects. Such flows are described by the barotropic vorticity equation.

$$\left(\frac{\partial\psi}{\partial x}\frac{\partial}{\partial y} - \frac{\partial\psi}{\partial y}\frac{\partial}{\partial x}\right)(\vec{\nabla}^2\psi - F\psi + \eta_b) + \beta\frac{\partial\psi}{\partial x} = \frac{\alpha r}{2}\vec{\nabla} \cdot (\vec{T} \times \hat{e}_3) - \frac{r}{2}\vec{\nabla}^2\psi + Re^{-1}\vec{\nabla}^4\psi \quad (1)$$

$$u = -\frac{\partial\psi}{\partial y}, v = \frac{\partial\psi}{\partial x} \quad (2)$$

Both equations are non-dimensional. Here, x and y represent the zonal and latitudinal coordinate in a Cartesian frame, where x varies between the western most point of the basin, $x_W = 0$, and the eastern most point of the basin, $x_E = 1$, and $y \in [0,1]$. The streamfunction ψ both represents the zonal velocity component u as well as the meridional component v of the flow velocity, see Equation (2). Furthermore, η_b is the bottom topography with respect to the mean ocean floor, and \vec{T} the wind stress vector, with zonal wind stress component τ^x and meridional wind stress component τ^y . The term $\beta = \frac{\beta_0 L^2}{U}$ represents the relative importance of the Coriolis force to inertia (see Table 1 for the definition and magnitude of each term). The parameters $F = f_0 L^2 / (gD)$ (Froude number), $Re = U / (f_0 L)$ (Reynolds number), $\alpha = 2\tau_0 / (\rho_0 f_0 \sqrt{2A_H / (f_0 L^2)} DU)$ and $r = \sqrt{2A_V / (f_0 L^2)} / Re$, in order, represent the relative importance of Coriolis force to gravity, advection to horizontal shear, wind shear to lateral shear and bottom friction to inertia. Finally, the differential operator is defined as $\vec{\nabla} = (\partial_x, \partial_y, \partial_z)$ and the zonal, lateral and vertical unit vectors are defined as $\hat{e}_1 = (1,0,0)$, $\hat{e}_2 = (0,1,0)$ and $\hat{e}_3 = (0,0,1)$, respectively, in a Cartesian coordinate system.

The left hand side product in Equation (1) represents advection of potential vorticity due to spatial differences in inertia, free surface evolution and bottom topography gradients. The second term left hand side term represents the beta-effect. The right hand side terms represent vorticity input by wind forcing, bottom friction and lateral friction, respectively. The inertia's scale is of $\mathcal{O}(1/\beta)$, the lateral and bottom friction are at most of scale $\mathcal{O}(1/\beta)$. Therefore, only the change in vorticity by wind can compensate that due to the beta-effect. Equation (1) can thus be scaled with a factor β to get the following expression:

$$\frac{1}{\beta} \left(\frac{\partial \psi}{\partial x} \frac{\partial}{\partial y} - \frac{\partial \psi}{\partial y} \frac{\partial}{\partial x} \right) (\vec{\nabla}^2 \psi - F\psi + \eta_b) + \frac{\partial \psi}{\partial x} = \vec{\nabla} \cdot (\vec{T} \times \hat{e}_3) - \frac{r}{2\beta} \vec{\nabla}^2 \psi - \frac{1}{Re\beta} \vec{\nabla}^4 \psi \quad (3)$$

Since large scale flow is considered, the scales of Table 1 can be used. From this, it follows that β is large, $F = \mathcal{O}(1)$, $r = \mathcal{O}(1)$ and $Re^{-1} \ll 1$, which allows the use of $1/\beta$ as a small parameter. This parameter occurs in the highest derivatives so the method of inner and outer expansion can be applied on Equation (3):

$$\psi(x, y) = \psi^0(x, y) + \beta^{-1} \psi^1(x, y) + \dots \quad (4)$$

L	D	ρ_0	U	f_0	A_H	A_V	τ_0	β_0
1000 km	1 km	10^3 kg/m ³	0.01 m/s	7.292×10^{-4} s ⁻¹	$10^2/10^4$ m ² /s	$10^{-4}/10^{-2}$ m ² /s	0.2 N/m ²	2.0×10^{-11} (ms) ⁻¹

Table 1 From left to right: scales of the ocean length, ocean depth, water density, horizontal surface velocity of the ocean flow, first order approximation of the Coriolis parameter (rotation time: 1 sidereal year), horizontal and vertical friction coefficient, wind stress and the meridional gradient of the Coriolis parameter.

The $\mathcal{O}(1)$ result of the expansion of Equation (3) is the Sverdrup balance, which describes the flow in the interior domain. The balancing vorticity terms in this equation must be those due to the Coriolis effect and the wind at the ocean's surface, since the Coriolis term is large and all other terms but the wind forcing are small:

$$\frac{\partial \psi^0}{\partial x} = \vec{\nabla} \cdot (\vec{T} \times \vec{e}_3) \quad (5)$$

The boundary condition for the Sverdrup balance is that $u = 0$ at the eastern coast.

Wind can blow over the entire ocean domain, but this does not have to be the case. It could also be that only one half of the ocean is forced by wind and the other half is unforced. Via model analysis, one can investigate how effectively the wind can influence the entire ocean circulation depending over which domain it is present. From this analysis, it could be deduced where changes in the wind induced flow took place if wind was the driving factor behind the observed changes in MC and MS transport.

The point east or west of which wind will be truncated, called $x = x_A$, is also the longitudinal position where the island will be placed. To keep things simple, all situations under consideration will be with zero meridional wind stress. To keep the jump from present wind to absent wind smooth, which is in order to prevent wind and ocean flow pattern discontinuities, the wind is brought to zero by use of a tangent hyperbolic (see Figure 5).

The wind will vary with latitude and the point at which the wind stress curl is zero, can be varied via a parameter. Once chosen, this point of zero wind stress curl is fixed. This parameter allows to model the effect of a shifting gyre boundary due to a shift in the wind forcing on the ocean circulation and thus on transport. This is based on earlier research on the effects of the shift of the Tropical Gyre and Subtropical Gyre on the transport through the Mozambique Channel (Palastanga *et al.*, 2006; Ridderinkhof *et al.*, 2010), which is too found to be a consequence of changes in the wind forcing on the Indian Ocean.

The wind stress is thus given by the following expression:

$$\tau^x = -\frac{1}{2\pi} \cos(2\pi\{y + n\})F_i(x), \quad (6)$$

$$\tau^y = 0 \quad (7)$$

In Equation (6), n indicates the latitude of minimum wind stress in degrees (negative: south). Equation (6) and Equation (7) are both dimensionless. The term F_i represents the damping factor that puts down the wind at the desired way: no damping (F_1), damping east of $x = x_A$ (F_2) or damping west of $x = x_A$ (F_3).

$$F_1(x) = 1, F_2(x) = \frac{1}{2} \left\{ \tanh\left(\frac{x_A - x}{0.01}\right) + x \right\}, F_3(x) = \frac{1}{2} \left\{ \tanh\left(\frac{x - x_A}{0.01}\right) + x \right\} \quad (8)$$

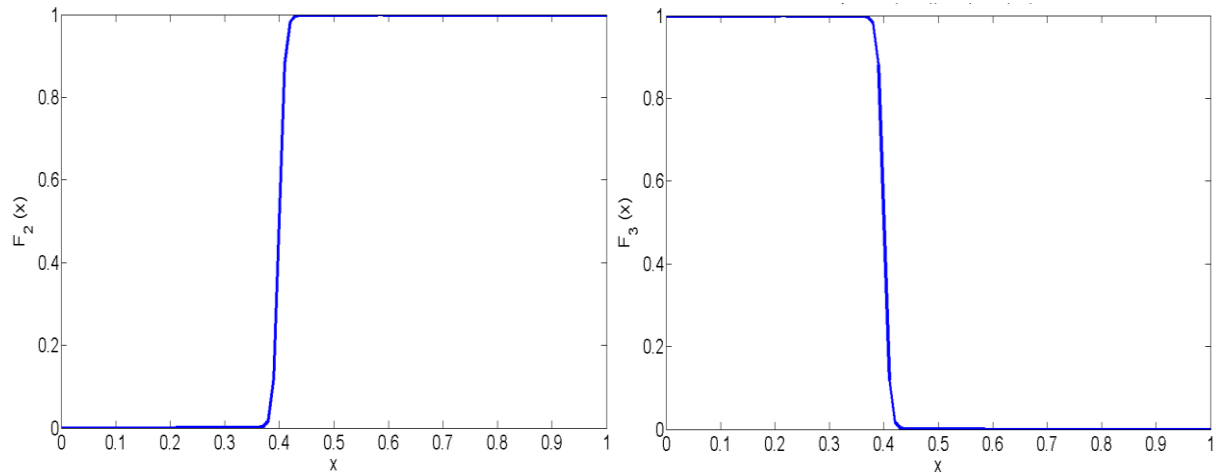


Figure 5 Functions as a function of longitude x by which the wind over the ocean basins is cut-off via a tangent hyperbolic at $x = x_A$: (left) for the case that wind only blows over the area east of x_A and (right) for the case that wind only blows west of x_A . A reference case which will also be investigated is $F_1(x) = 1$, which means that wind is present over the entire ocean basin.

With the representations of the streamfunction and wind stress via Equation (5) to Equation (8), the following solution can be found:

$$v_i^0(x, y) = -\sin(2\pi\{y + n\})F_i(x) \quad (9)$$

$$\psi_i^0(x, y) = -\sin(2\pi\{y + n\})G_i(x) + \Psi_i^0(y) \quad (10)$$

$$u_i^0(x, y) = 2\pi \cos(2\pi\{y + n\})G_i(x) + U_i^0(y) \quad (11)$$

The subscript i indicates what case is at the attention: full wind ($i = 1$), only wind at the eastern domain ($i = 2$) or only wind at the western domain ($i = 3$). The terms $\Psi_i^0(y)$ and $U_i^0(y)$ result from the boundary condition that $u = 0$ at $x = x_W$; the term $G_i(x)$ results from the integration of $F_i(x)$ over x , where the constant resulting from this integration is put into the expressions for $\Psi_i^0(y)$ and $U_i^0(y)$. The constant resulting from the integral of $-\frac{\partial \psi^0}{\partial y}$ over y can be put to zero without loss of generality, since the coast encloses the entire ocean basin for our ocean model. Putting this integration constant to zero when applying the integral to an island cannot just be done, since an island is surrounded by water that can flow around it. This problem will be the main subject of the next two subsections.

$$\Psi_i^0(y) = \sin(2\pi\{y + n\})G_i|_{x=1} \quad (12)$$

$$U_i^0(y) = 2\pi\cos(2\pi\{y + n\})G_i|_{x=1} \quad (13)$$

$$G_1(x) = x \quad (14)$$

$$G_2(x) = \frac{1}{200} \left\{ \log \left(\cosh \left(\frac{x_A - x}{0.01} \right) \right) + \frac{1}{2} x^2 \right\} \quad (15)$$

$$G_3(x) = \frac{1}{200} \left\{ -\log \left(\cosh \left(\frac{x - x_A}{0.01} \right) \right) + \frac{1}{2} x^2 \right\} \quad (16)$$

The meridional net wind induced transport is proportional to the meridional wind velocity and simply follows from the integral of Equation (9) over the zonal and meridional domain over which the transport is desired to be known.

2.1.2 Stommel boundary layer

In order to realize the condition that the flow is parallel to the western coast, a Stommel boundary layer is introduced. The solution can be found in literature like Dijkstra (2008).

For a Stommel boundary layer, the bottom friction boundary layer thickness is larger than the maximum layer thickness for both lateral friction and inertia at the same location. This means that the barotropic vorticity equation reduces to the balance between vorticity by the Coriolis effect, wind stress and lateral friction. The lateral friction layer thickness can be written as $\delta_S = \frac{r}{2\beta} L$. For the Stommel solution, the barotropic potential vorticity equation reduces to:

$$\frac{\delta_S}{L} \vec{\nabla}^2 \psi = -\frac{\partial \psi}{\partial x} + \vec{\nabla} \cdot (\vec{T} \times \hat{e}_3) \quad (17)$$

It is convenient to introduce a local boundary layer coordinate, $\lambda = (x - x_W)/\ell = x/\ell$, which ranges between 1 at $x = x_W$ and 0 at $x = x_W + \ell$:

$$\frac{\delta_S}{\ell^*} \left(\frac{\partial^2 \psi}{\partial \lambda^2} + \frac{\ell^2 \partial \psi}{\partial y^2} \right) = -\frac{\partial \psi}{\partial \lambda} + \ell \vec{\nabla} \cdot (\vec{T} \times \hat{e}_3) \quad (18)$$

Using the values $E_V \sim 1.0 \cdot 10^{-6}$ (vertical Ekman number, representing relative importance of friction in the vertical direction to Coriolis force), $\beta \sim 1.6 \cdot 10^2$ and $\epsilon \sim 1.0 \cdot 10^{-4}$ (taken from Table 5.1 of Dijkstra (2008)), the following scale for the Stommel boundary layer thickness ℓ can be found:

$$\frac{\delta_S}{L} = \frac{\ell}{L} = \frac{r}{2\beta} = \frac{\sqrt{E_V}}{2\beta\epsilon} = \frac{\sqrt{2E_V}}{2\beta\epsilon} \Rightarrow \frac{\ell}{L} = \frac{\sqrt{2}}{32} \approx 0.0442 \quad (19)$$

The above result actually states that the Stommel boundary layer thickness equals about 4% of the total basin width (so about 44 km, see Table 1). Using an inner expansion ($\tilde{\psi}(\lambda, y) = \tilde{\psi}^0(\lambda, y) + \ell\tilde{\psi}^1(\lambda, y) + \dots$), Equation (18) reduces to:

$$\frac{\partial^2 \tilde{\psi}^0}{\partial \lambda^2} + \frac{\partial \tilde{\psi}^0}{\partial \lambda} = 0 \quad (20)$$

To solve Equation (20), boundary conditions are necessary. The first boundary condition is that $\psi^0 = 0$ at $x = x_W$ (or in terms of the local boundary layer coordinate: $\tilde{\psi}^0 = 0$ at $\lambda = 0$). The second boundary condition is a transition boundary condition, which states that the Stommel boundary layer should smoothly transit into the inner ocean Sverdrup region: $\lim_{\lambda \rightarrow \infty} [\tilde{\psi}^0(\lambda, y)] = \lim_{x \downarrow x_W} [\psi^0(x, y)]$.

The general solution of Equation (20) is:

$$\tilde{\psi}^0(\lambda, y) = C_1 \exp(-\lambda) + C_2(y) \quad (21)$$

The boundary condition that $\tilde{\psi}^0 = 0$ at $\lambda = 0$ results in $C_1 = -C_2$; the matching boundary condition implies that $C_2 = \Psi_i^0(y)$. Combining these outcomes gives the Stommel boundary solution:

$$\tilde{\psi}_i^0 = \psi_i^0(x, y)|_{x=x_E+\ell} \left\{ \exp\left(-\frac{x}{\ell}\right) - 1 \right\} \quad (22)$$

This far, only flow in a closed square ocean basin without obstacles has been treated. In the case of the Indian Ocean and the Pacific Ocean, there are obstacles, like ridges and islands. The presence of islands and ridges has important consequences for flow in the ocean. These will be treated next.

2.1.3 General effects of an island on ocean flow

Makassar Strait is located between a large network of islands and other channels and strait. The flow through such networks is very complex and has been the subject of other researches. Here, emphasis will be made to the effect of islands on transport through the Mozambique Channel, which is influenced by only one island: Madagascar.

In a square basin without an island, the general flow exists of an inner region, where flow is governed by the Sverdrup balance, and a western boundary layer, where the flow in first order approximation, is governed by the bottom friction and beta effect. Adding an island to an ocean will further separate the ocean into smaller regions with their own dominant flow patterns (see, for example, LaCasce and Isachsen (2007)). This is schematically shown in Figure 6.

A first consequence of the island is that the inner ocean splits into two Sverdrup regions. The regions east, north and south of the island still follow the original Sverdrup solution. The region west of the island follows the Sverdrup balance for a situation as though the eastern mainland

boundary is shifted towards the zonal position of the island. This behaviour is of course also found back in the western Stommel layer near the mainland west of the island.

A second important effect of the presence of an island is the appearance of a boundary layer east of the island. This layer, in first order approximation, obeys the same Stommel dynamics valid for the western Stommel boundary layer. Two differences exist between these two Stommel layers: first of all, the island's Stommel layer acts as though the western mainland coast has been shifted towards the island's zonal position, and second, other than at the mainland's coast, the streamfunction does not need to be zero at the island's coast. What value it should have is discussed in the next subsection.

A third important effect of the island is the appearance of two diffusion layers west of the island, one at the northern tip of the island and one at the southern tip. These layers are also called free boundary layers, since they form a transition layer between two water regions. These two layers ensure a smooth transition between flow at the region west of the island towards flow at the region northwest and southwest of the island.



Figure 6 Schematic representation of the effects of an island on the flow in a square ocean basin. It causes the separation of the ocean into two Sverdrup regions (blue and purple) with accompanying Stommel boundary layers along the western coast (darker blue and darker purple). Further, it is accompanied by the appearance of a Stommel boundary layer east of the island. And finally, the island causes the presence of two free boundary layers west of the northern and southern tip of the island such that the flow west of the island smoothly transits towards the flow northwest and southwest of the island.

In a square ocean basin, flow going north in the inner Sverdrup region goes southward in the Stommel region and vice versa. If an island is present, the flow between the meridians of the islands tips east of the island can recirculate in two ways. Flow going north-westward (south-

westward) can go recirculate either via the Stommel layer east of the island or via the Sverdrup region west of the island. Since the flow in a western boundary layer is rather turbulent, it is easier for the water to tip over the island and to recirculate via the Sverdrup region west of the island. If one would measure the southward volume transport west of the island, the value obtained will thus be the sum of two sources: a source which is outside the ocean of interest (like the ITF, which is brought to Madagascar via the SEC) and a local source which is the wind induced recirculation due to pressure difference at the island's tips.

This separation of the total transport west of island into a remote source and a term due to wind-induced recirculation is the basis of the Island Rule of Godfrey (1989). It gives a new constraint to the streamfunction on the boundary. On the mainland, it has to be zero since no flow can go through the boundary. On the island, it does not have to be zero since water can circle around it and therefore create a pressure difference between the island's tips. In the next section, the Island Rule will be discussed and its role in an analytical model setting will be given.

2.1.4 Baroclinic flow around an island: Island Rule

Flows around islands are an active field of research (De Ruijter, 1982; Wajsowicz, 1992; Pedlosky *et al.*, 1997; Spall, 2002; LaCasce and Isachsen, 2007). As described before, due to the pressure difference that can exist between the tips of an island, the streamfunction value on an island does not have to be zero. If the island is Madagascar, this constant represents the addition of wind forcing on the Indian Ocean to the flow through the Mozambique Channel. This forms an extra constraint to the flow. The streamfunction will tend to a real valued constant at the island which is not necessarily zero. Godfrey (1989) has derived a general expression for this constant, which has become known as the linear Island Rule.

Godfrey (1989) derived his rule for a reduced gravity model so that the ocean is stagnant below some specific depth, which is such that topographic features like ridges are below it. Godfrey started from the stationary, depth-integrated momentum equations (existing of the Coriolis force in a β -plane, the pressure gradient force, wind forcing and lateral and bottom friction) and the continuity equation for incompressible fluids. His boundary conditions are that the normal and tangential velocity components are zero at all lateral boundaries. The western boundary current width is taken to be smaller than length scales on which coast lines and wind vary. Both the pressure head and consequent mass transport are assumed to be independent of the friction coefficients. All vorticity entering the western boundary is assumed to immediately dissipate at the latitude where it is created. Finally, the pressure is assumed to be continuous. That is, there are no hydraulic jumps.

Godfrey (1989) then uses these boundary conditions and the momentum and continuity equations to retrieve the Sverdrup balance in the ocean interior. He also derives the balance between pressure gradients and wind forcing near the island's western coast. Another balance is derived between the same forces near the nearest (mainland) coast that is located east of the island. From these three balances, he derives his Island Rule, which gives the transport along the western coast of an island in terms of the wind stress field over the ocean and the latitudinal positions of the island's northern ($y = y_N$) and southern ($y = y_S$) tip. We will use the non-

dimensional form (Spall *et al.*, 2002) when deriving the analytical solutions for simplified theoretical situations.

$$\psi_I = -\frac{1}{\rho_0(y_N - y_S)} \oint_{ABCD} \tau^{(l)} dl \quad (23)$$

The integration goes along the path indicated in Figure 7. The trajectory A to B goes along the latitude of the southern tip of the island. The trajectory B to C is along the nearest coast east of the island. Trajectory C to D is along the latitude of the northern tip of the island, back from the nearest coast east of the island towards the island. Finally, trajectory D to A runs along the western coast of the island, back to the starting point.

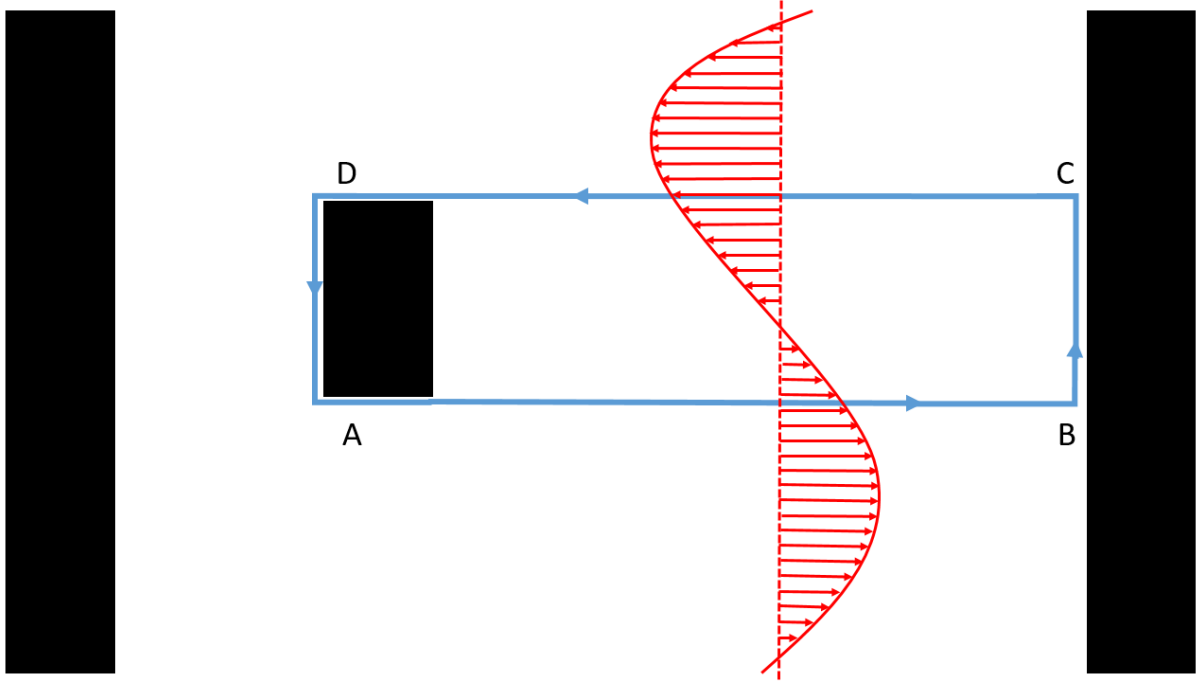


Figure 7 The Island Rule implies that the transport around an island in first order follows directly from the integration of the wind stress (in red, with arrows indicating the theoretical wind stress pattern, the curve a fit through the arrows and the dotted line the line of zero wind stress for this longitude) along a closed curve. This curve exists of four parts. The first part (A to B) runs from the island's southern tip to the nearest coast at the west along the latitude of the southern tip. Then, the curve follows this coast up to the latitude of the northern tip of the island (B to C). The curve then loops back to the island along the latitude of the northern tip (C to D). Finally, the curve loops back to the southern point of the island along the island's western coast (D to A).

In the previous section, three important consequences of an island to the ocean flow have been highlighted. Now that the expression of the Island Rule is known (Equation (23)), expressions for the four new regions can be determined.

First of all, a look is taken at the new Sverdrup region west of the island. West of the island, thus for $x \in [x_W + \ell, x_A]$ and $y \in [y_S + \delta/2, y_N - \delta/2]$, the inner flow streamfunction is described by a Sverdrup solution, which has the boundary condition that the streamfunction equals the Island Rule value ψ_I at $x = x_A$. The Sverdrup solution west of the island thus becomes:

$$\psi^0 = -\sin(2\pi\{y + n\})\{G_i(x_A) - G_i(x)\} + \psi_I \quad (24)$$

The effect of the island on the Sverdrup solution at its west is of course of direct influence on the Stommel layer solution at the west coast for the meridional band between the island's tips via the term $\psi_i^0(x, y)|_{x=x_E+\ell}$ in Equation (22).

Next is the expression of the Stommel boundary layer solution east of the island. This layer is described by Stommel dynamics like in Section 2.1.2, this time with the difference that the value of the streamfunction should not be zero at the transition point to land but equal to the constant value ψ_I :

$$\check{\psi}_i^0 = \left(\psi_I - \psi_i^0(x, y)|_{x=x_E+\ell}\right) \exp\left(\frac{x-x_A}{\ell}\right) + \psi_I \quad (25)$$

Finally, the focus is turned to the transition layers east of the northern and southern tip of the island. As has been noted by the meridional boundaries of the region where the Sverdrup region west of the island is located, the Sverdrup solution region west of the island does not extend totally up to the island's tips. The Sverdrup flow east of the island must transit into the flow beyond the tips in a smoothed way since the barotropic flow does not support hydraulic jumps. In Appendix A, the derivation of the solutions for the diffusion layers in the ocean interior region are discussed.

For the northern tip of the island, the free boundary layer solution is given by:

$$\hat{\psi} = \frac{\left(\lim_{y \downarrow y_1} \psi_{sv,1}\right)}{2} \operatorname{erfc}\left(-\frac{y-y_0}{2\sqrt{\delta(x_A-x)}}\right) + \frac{\left(\lim_{y \uparrow y_2} \psi_{sv,2}\right)}{2} \operatorname{erfc}\left(\frac{y-y_0}{2\sqrt{\delta(x_A-x)}}\right) \quad (26)$$

The terms $\psi_{sv,1}$ and $\psi_{sv,2}$ represent the Sverdrup streamfunction solutions at the Sverdrup domain north of the island at the upper diffusion layer boundary y_1 and the Sverdrup solution west of the island at the lower diffusion layer boundary y_2 , respectively. Using a free boundary layer thickness of $\delta = \frac{\ell}{5}$, where the factor 1/5 is chosen by trial and error, these boundaries are parameterized as:

$$y_1 = y_n + 2\sqrt{\delta(x_A - x)} \quad (27)$$

$$y_2 = y_n - 2\sqrt{\delta(x_A - x)} \quad (28)$$

For the southern tip, the solution is very similar. With $\psi_{sv,1}$ now representing Sverdrup flow south of the island at y_1 and $\psi_{sv,2}$ Sverdrup streamfunction solutions west of the island at y_2 , respectively, the solution is given by:

$$\hat{\psi} = \frac{\left(\lim_{y \downarrow y_1} \psi_{sv,2}\right)}{2} \operatorname{erfc}\left(-\frac{y-y_0}{2\sqrt{\delta(x_A-x)}}\right) + \frac{\left(\lim_{y \uparrow y_2} \psi_{sv,1}\right)}{2} \operatorname{erfc}\left(\frac{y-y_0}{2\sqrt{\delta(x_A-x)}}\right) \quad (29)$$

$$y_1 = y_s + 2\sqrt{\delta(x_A - x)} \quad (30)$$

$$y_2 = y_s - 2\sqrt{\delta(x_A - x)} \quad (31)$$

In the Stommel boundary layer at the main coast west of the island, between $y_S - \delta/2$ and $y_N + \delta/2$, $\psi_{sv,1}$ and $\psi_{sv,2}$ should simply be replaced by $\psi_{st,1}$ and $\psi_{st,2}$, the Stommel boundary layer solutions at these latitudes, respectively.

Up till now, models for the relation between the curl of surface wind and the ocean surface flow has been investigated. In these models, no feedback is included between the ocean and the atmosphere nor is the ocean divided into layers. However, the ocean can exist of layers, allowing baroclinic and barotropic processes to act separately, and the ocean and atmosphere in general do feedback to each other. In the next section, a mechanism will be proposed for to explain the changes observed in the MC and MS transport based on baroclinic and non-stationary processes.

2.2 Mechanism for changes in wind-induced transport

Back in 2006, the transports through the Makassar Strait and the Mozambique Channel changed. The changing transport signals might be covariation signals since, at least at an annual scale, the transports show similar behaviour. Changes in oceanic volume transports can either be driven by atmospheric processes, oceanic processes or a combination of both.

One of the possible coupled ocean-atmosphere processes that can influence the wind velocity, and thus the wind forcing on the ocean flow and back, is the coupling between sea surface temperature and surface winds. Since numerous studies have found that the sea surface temperature state of the Indian Ocean has changed in the period that the transport transitions in the MC and the MS occurred (Vinayachandran *et al.*, 2007; Horii *et al.*, 2008; Luo *et al.*, 2008; Rao *et al.*, 2008, Qiu *et al.*, 2012), this mechanism could be a cause of the observed transport transitions.

The way that the sea surface temperature and sea surface winds can influence each other is shown in Figure 8. If one side of an ocean surface heats up and the other side cools down, the spatial temperature gradient can lead to convection of air at the heating and cooling areas. Due to this convection, advection of air occurs over the ocean's surface. In other words: wind will blow over the ocean's surface in the direction of the temperature gradient (Nihoul, 1985; Wilson *et al.*, 2013; McPhaden *et al.*, 2015). This process can lead to even larger temperature gradients due to the sinking of warm water at the warmer areas and rising of cool water at the cold areas due to the convection of air, which can lead to even stronger convection and advection. This process is known as the Bjerknes feedback (Cai *et al.*, 2013).

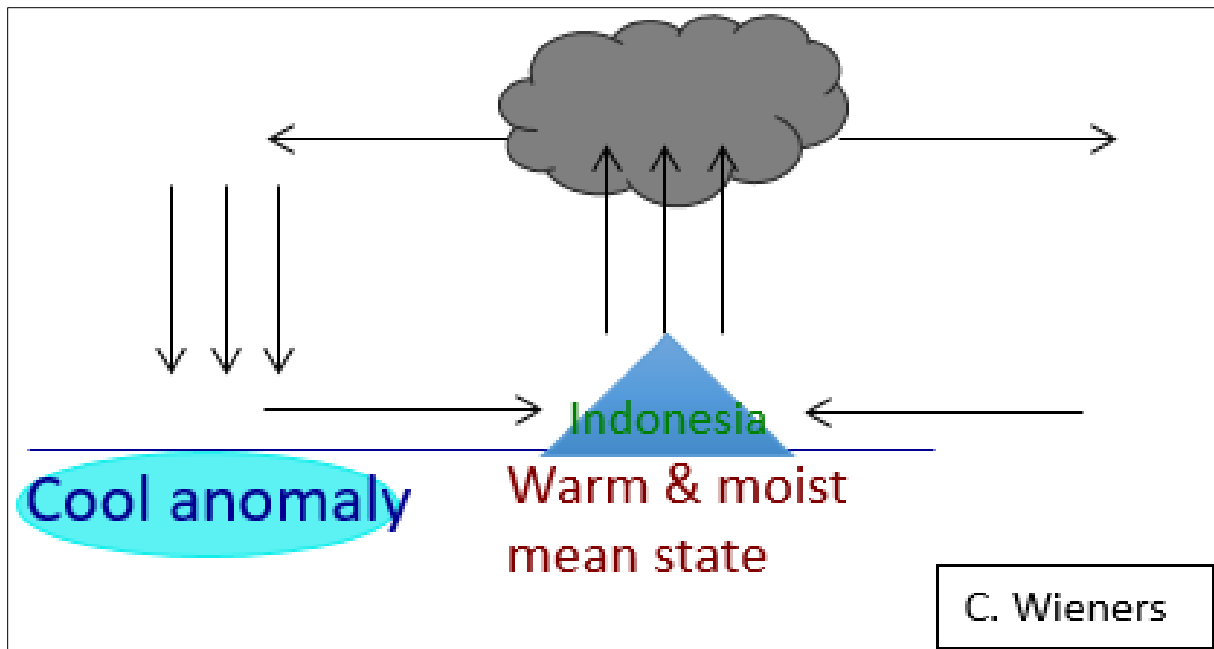


Figure 8 Schematic depiction of the Bjerknes feedback at the Indian Ocean and Pacific Ocean. A change in temperature gradient over one of the oceans can lead to anomalous convective process above the cooler and warmer areas. This will lead to advection in the direction of the temperature gradient. The anomalous wind patterns thus created can then lead enhancement of the temperature gradient by causing rising and sinking at the cooler and warmer areas, respectively, which leads to stronger winds, et cetera.

Changes in the wind forcing force the ocean to adapt. There are several ways via which this adaption can occur. The Mozambique Channel is located in the subtropics, the Makassar Strait in the tropics. The adaptation to changing wind forcing over a tropical-subtropical region can first of all occur via advection of flow along the coasts and gyres. Second, it can occur via changes in subtropical Rossby wave processes and via changes in the dynamics of equatorial Kelvin waves, equatorial Rossby waves and related coastal Kelvin wave formation along the East Indian Archipelago.

In order to find a plausible adaptation wind-forced mechanism related to the changing transports in 2006, one must note that the Mozambique Channel transport transits earlier than that at Makassar Strait. Equatorial Kelvin waves travel from west to east, so in the same direction as the direction of the changing transports chronology. There is thus a matching west to east chronology between the transport transitions in the MC and the MS and the influence on oceanic flow by equatorial Kelvin waves and the mechanism that causing them. This match makes equatorial Kelvin waves a plausible adaptation mechanism.

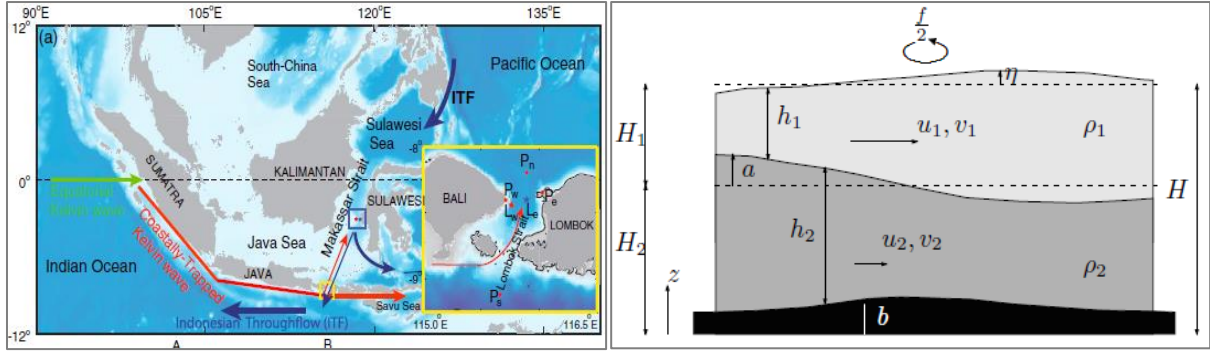


Figure 9 (left) Possible pathway for equatorial Kelvin waves towards Makassar Strait. Once they hit the coast of Sumatra, the equatorial Kelvin waves travel further eastward as coastally bounded Kelvin waves. These Kelvin waves follow the Indian Archipelago and, if capable to do so, cross Lombok Strait to reach the Makassar Strait. Figure from Pujiana *et al.* (2013). (right) Definition of the bathymetry (total sea mean sea depth H), the mean thermocline depth (H_1), the sea level anomaly (η_1) and the thermocline elevation anomaly (a) in a 2-layer model in (densities ρ_1 and ρ_2 , zonal velocities u_1 and u_2 and meridional velocities v_1 and v_2 for the surface and bottom layer, respectively) in a rotating frame with Coriolis parameter f . In such a model, H_2 is the mean thickness of the layer below the thermocline, b is the bottom topography, and $h_1 = H_1 - a + \eta$ and $h_2 = H_2 + a - b$ are the actual thicknesses of the two layers separated by the thermocline. Figure adapted from Cushman-Roisin & Becker (2011).

The question is whether a Kelvin wave can bring signals from the western Indian Ocean to the eastern Indian Ocean within two to three months, which is the observed delay between the transition of the MC transport and the MS transport. To find out, one must determine how long such a wave will take to reach Makassar Strait. Equatorial Kelvin waves can be initiated everywhere along the east African coast and travel towards and over the Equator. They could also directly be initiated on the Equator itself and then cross the ocean. Whether being created on the Equator or at the African coast, at some time they will reach the coast of Sumatra. There they can split up into reflected near-equatorial Rossby waves that travel westward and coastal Kelvin waves that follow the coast of the East Indian Archipelago. If strong enough, these waves could partly pass the narrow gateways of the East Indian Archipelago and travel towards and through Makassar Strait, as is shown in the left panel of Figure 9 (Drushka *et al.*, 2010; Joseph *et al.*, 2012). While passing the gateways, the Kelvin wave initiates a subtropical Rossby wave, which will travel towards Madagascar.

There are two sorts of equatorial Kelvin waves: the faster barotropic Kelvin waves, whose velocity depends on the full ocean depth, and the slower baroclinic Kelvin waves, whose velocity depends on the depth of the thermocline (see right panel of Figure 9). Their velocities are given in Equation (32) and Equation (33), respectively. In Equation (32), $g = 9.81 \text{ m/s}^2$ is the gravitational acceleration and H is the mean ocean depth in meters. In Equation (33), the reduced gravity g' in m/s^2 and thermocline depth H_0 in meters are present (Dijkstra, 2008; Cushman-Roisin and Becker, 2011). The reduced gravity is given by Equation (34), with $g = 9.81 \text{ m/s}^2$ as in Equation (32), reference density $\rho_0 = 10^3 \text{ kg/m}^3$ and difference in density between the layers separated by the thermocline $\Delta\rho$ in kg/m^3 . In literature (Valsala, 2008; Nagura and Masumoto, 2015), values range between 2 kg/m^3 and 3 kg/m^3 , so it is convenient to choose the middle of this range: $\Delta\rho = 2.5 \text{ kg/m}^3$.

$$c = \sqrt{gH} \quad (32)$$

$$c = \sqrt{g'H_0} \quad (33)$$

$$g' = \frac{\Delta\rho}{\rho_0} g \quad (34)$$

If Kelvin waves indeed form the adaptation mechanism of the ocean, the question then is how the adaptation will be. The effect of Kelvin waves on the Makassar Strait throughflow has been studied already quite extensively. Two types of Kelvin waves can be created on the Equator: downwelling Kelvin waves by westerly trade winds and upwelling Kelvin waves by easterly trade winds (Nihoul, 1985; Rao *et al.*, 2008; Van der Werf, 2009; Iskandar 2012; Yan *et al.*, 2012). Kelvin waves tend to influence both the sea surface elevation and the thermocline depth elevation. Upwelling (downwelling) Kelvin waves lower (lift) the sea surface and lift (lower) the thermocline. The shape of the sea surface elevation is mirroring that of the thermocline. By this influence on the elevation of the ocean water layers, upwelling (downwelling) Kelvin waves increase (decrease) the southward flow in the Makassar Strait (Drushka *et al.*, 2010; Gordon *et al.*, 2012; Susanto *et al.*, 2012; Pujiana *et al.*, 2013; Susanto and Song, 2015). A change in the Indian Ocean trade winds will thus lead to a change in the type of Kelvin waves travelling towards Makassar Strait and by that, to a change in the ocean water layers elevation and eventually to a change in the MS transport.

A special fluctuation in the wind, known as the Madden-Julian Oscillation, is often connected to the initiation process of equatorial Kelvin waves in the oceans. A short intermezzo on this relation is given in Appendix B.

One big difference between the Makassar Strait and the Mozambique Channel is that the latter is only directly connected to one ocean, whereas the former is connected to two oceans: the Indian Ocean and the Pacific Ocean. It is therefore possible that not only changing conditions in the Indian Ocean have led to changes in the ITF, but also changes in the Pacific Ocean's dynamical state.

Also in the Pacific Ocean, a changing sea surface temperature state can lead to changing trade winds. This can be a self-strengthening process due to Bjerknes feedback. The Pacific Ocean can then adapt to changes due to this feedback mechanism by the production of Kelvin waves. In this way, if the Pacific Ocean is in a La Nina (El Nino) state, easterlies (westerlies) trade wind anomalies will occur. These can lead to stronger (weaker) upwelling Pacific Ocean equatorial Kelvin waves. The result is that the sea level in the eastern Pacific may show positive (negative) anomalies accompanied by a shoaled (deepened) thermocline (Llovel *et al.*, 2010; Tillinger and Gordon, 2010; Becker *et al.*, 2011; Gordon *et al.*, 2012; Gordon and Huber, 2013; Siedler *et al.*, 2013). The consequence would be an increased southward Makassar Strait throughflow.

Earlier studies on the southern Indian Ocean resulted in a link between changes in the sea surface temperature and the position of the Tropical Gyre and the Subtropical Gyre. Numerous publications (DiMarco *et al.*, 2002; Palastanga *et al.*, 2006; Ridderinkhof *et al.*, 2010) state that a positive (negative) west to east sea surface temperature gradient can lead to a northward (southward) shift of the Tropical Gyre and Subtropical Gyre, a weakening (strengthening) of the South Equatorial Current and an increased (decreased) southward Mozambique Channel

transport. Most likely, this is due to changes in wind-forcing over the southern Indian Ocean due to changes in the sea surface temperature gradient and accompanying changes in the advection and convection patterns. This could namely lead to a change in the double gyre structure of the southern Indian Ocean flow, as can be seen from the elementary wind-driven oceanic flow solutions in Section 2.1.1 to 2.1.4.

When concluding that the SEC reduced, scientists pointed at a reduced zonal westward flow within the band 10°S to 15°S at 80°E (Ridderinkhof *et al.*, 2010). Earlier observational and model studies however have found that the main source of the Mozambique Channel throughflow is the Indonesian Throughflow, which is transported towards the MC via the SEC (Van der Werf, 2009; Le Bars *et al.*, 2013; Viebahn *et al.*, 2015). Therefore, since both the MS throughflow and MC throughflow are found to increase, it is more likely that the SEC also shifts northward instead of getting weaker. The possibility of a shifting SEC is supported by earlier research (Qu *et al.*, 2007; Valsala *et al.*, 2010; Du *et al.*, 2015).

The Mozambique Channel throughflow is thus thought to have changed due to a change in the Bjerknes feedback between the sea surface temperature and the sea surface winds, which is than accompanied by a consequent shift of the Indian Ocean gyres and the SEC. The changes in the along-channel flow velocity anomaly observed in the Makassar Strait is now supposed to be due to a combined effect of changes in the sea surface temperature state of the Indian Ocean and that of the Pacific Ocean. In the next sections, data and methods will be given in order to support these suggestions.

3 Applications

In the next subsection, the data used in this research will be described. The following subsections gives a description of the methods, like the use of running mean filters and making of Hovmoller diagrams used to analyse the data.

3.1 Data

Table 2 gives a short summary of the most important properties of the datasets described in this section (name, variables included in the datasets and resolution). A column is added that gives references to papers, handbooks and websites that give more details on the datasets, for example on how they are produced, what limitations they have and how they are distributed.

Dataset	Variables (units)	Resolution	Specifications
SSALTO/DUACS, AVISO	H_G, η (m)	1 day \times 0.25° \times 0.25°	SSALTO/DUACS User Handbook (CNES, 2015)
(NGDC) ETOPO2v2c	H (m)	0.25° \times 0.25°	National Geophysical Data Center, 2006; Amante and Eakins, 2009
IFREMER Top of Thermocline Depth (ttd_DTm02_c1m_reg2.0)	H_1 (m)	1 month \times 2° \times 2°	De Boyer Montégut <i>et al.</i> , 2007; Mignot <i>et al.</i> , 2007
State of the Ocean/IRI Data Library	DMI, NINO 3.4 (°C)	5 days	Reynolds <i>et al.</i> , 1988; Reynolds, 2002
ECMWF/ERA-Interim	U, V (m/s)	1 day \times 0.25° \times 0.25°	Berrisford <i>et al.</i> , 2011
OSCAR	u, v (m/s)	1 day \times 2.5° \times 2.5°	Bonjean <i>et al.</i> , 2002; Johnson <i>et al.</i> , 2007

Table 2 Summary of the properties of the datasets listed in this section. In the final column, references are given for the interested reader to get more information on the data processing, gathering, accuracy and distribution. Note that some of the datasets contain more variables than those listed here. Only the variables that are used for processing in this report are raised.

Already 17 years ago, Saji *et al.* (1999) discovered that the western tropical Indian Ocean sea surface temperature anomaly often has an opposite sign compared to that of the southeast tropical Indian Ocean. This phenomenon can be seen as a dipole structure in the Indian Ocean's surface temperature, which they called the Indian Ocean Dipole (IOD) or Zonal Mode. Saji *et al.* (1999) represent the sea surface temperature in the Western Tropical Indian Ocean by its mean over the box [50°E, 70°E] \times [10°S, 10°N], which is known as the WTIO. The mean sea surface temperature for the South-East Tropical Indian Ocean is represented by the mean value over the box [90°E, 110°E] \times [10°S, 0°S], which is known as the SETIO (see Figure 10). From these mean sea surface temperature values, the east to west sea surface temperature gradient, which is the Dipole Mode Index (DMI), can be calculated. The DMI was downloaded from the Ocean Observations Panel for Climate – State of the Ocean (OOPC) [website](#) and is provided by the International Research for Climate and Society (IRI) Data Library with a resolution of five days. To derive this index, IRI has used the Reynolds OIv2 SST analysis. The Dipole Mode Index is calculated as:

$$\text{DMI} = \text{WTIO} - \text{SETIO} \quad (35)$$

In some way, the IOD has a similar meaning in the Indian Ocean as the El Nino Southern Oscillation (ENSO) has for the Pacific Ocean. As the IOD represents the sea surface temperature structure of the Indian Ocean, ENSO partly represents the sea surface temperature structure of the Pacific Ocean. There are several indices that represent the ENSO. One of these is the NINO 3.4 index. This index is defined as the denotation from the 1982-2005 seasonal cycle of the sea surface temperature over the box [170°W, 120°W] \times [5°S, 5°N] (Barnston *et al.*, 1997), see right panel of Figure 10. If the NINO 3.4 index stays larger than 0.5°C (smaller than -0.5°C) for at least five consecutive months, the month centred in this time window is an El Nino (La Nina) month according to the [Climate Prediction Centre – Cold and Warm](#)

[Episodes by Season](#) webpage. This index is derived from the Reynolds OIv2 SST analysis and 5-days resolution values are downloaded from the [OOPC website](#).

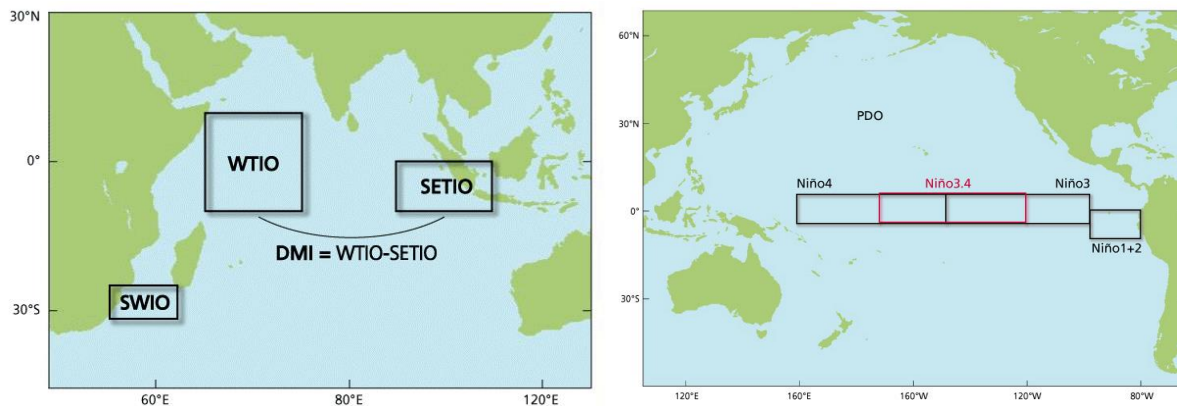


Figure 10 (left) Longitude versus latitude map indicating the locations of the regions whose average sea surface temperature represent the Western Tropical Indian Ocean sea surface temperature (*WTIO*) and the South-East Tropical Indian Ocean sea surface temperature (*SETIO*). The east to west sea surface temperature gradient is given by the Dipole Mode Index (*DMI*). Figure from [OOPC](#) (right) Longitude versus latitude map indicating the region over which the sea surface temperatures is used to calculate the NINO 3.4 index: the NINO 3.4 is given by the mean sea surface temperature over $[170^{\circ}\text{W}, 120^{\circ}\text{W}] \times [5^{\circ}\text{S}, 5^{\circ}\text{N}]$ with respect to the 1982-2005 seasonal cycle for that same area (red box). Figure from [OOPC](#).

The third dataset consists of absolute dynamic topography (H_G). The absolute dynamic topography is the sea surface height relative to the Earth's geoid, which on its turn is the shape the oceans would have if the oceans would not be in motion. The data is provided by Archiving, Validation and Interpretation of Satellite Oceanographic (AVISO) and is part of the Ssalto/Duacs along-track multi-mission altimeter products. The data has a temporal resolution of 1 day and a spatial resolution of 0.25° in both latitude and longitude direction. The data is accessed via the AVISO [website](#). The altimeter products were produced by Ssalto/Duacs and distributed by AVISO, with support from [CNES](#) (Centre National d'études Spatiales).

Another AVISO dataset used in this report is the AVISO along-track daily near-real-time sea level anomaly data. This data is, too, part of the Ssalto/Duacs along-track multi-mission altimeter products and has the same temporal and spatial resolution as the AVISO absolute dynamic topography data described above. It is accessed via the AVISO [website](#). The Ssalto/Duacs altimeter products were produced and distributed by the Copernicus Marine and Environment Monitoring Service ([CMEMS](#)).

To analyse the wind velocity over the Indian Ocean and Pacific Ocean, European Reanalysis (ERA) – Interim daily zonal (U) and meridional (V) velocity data are used. These datasets are download from [website](#) of the European Centre for Medium-Range Weather Forecasts (ECMWF). Each velocity component is gathered at 1 day resolution and has a 0.25° resolution in both zonal and meridional direction.

To derive the estimate of the time needed to travel the same distance by barotropic Kelvin waves, the bathymetry (H) data of the National Geophysical Data Center (NGDC) is used. The data consists of 2-Minute Gridded Global Relief Data, composed in June, 2006 and distributed by the [World Data Service for Geophysics](#). As the name of the dataset says, the zonal and lateral resolution is $1/30$ of a degree.

Another depth-related dataset used in this report is the top of thermocline depth (H_1) data from the Institut Français de Recherche pour l'Exploitation de la Mer (IFREMER). This dataset is part of the [IFREMER/LOS Surface Warm Layer Climatology](#) data collection. The data consists of long-term monthly values for the period 1961-2008 with a 2 degrees resolution in both zonal and meridional direction. IFREMER defines the top of the thermocline as the depth at which the oceanic potential temperature is 0.2°C lower than the potential temperature at 10 meters below the surface.

The final dataset used is the near-global Ocean Surface Current Analysis Real-time ([OSCAR](#)) dataset. This dataset is derived from both satellite altimeter and scatterometer data and has a 1-degree resolution in zonal and meridional direction. The OSCAR data was developed by Gary Lagerloef, Fabrice Bonjean, and Kathleen Dohan from Earth and Space Research (ESR). OSCAR data as originally developed at and provided by JPL Physical Oceanography DAAC was obtained at 2.5 degrees grid resolution for January 1993 – December 2015 from the [Integrated Climate Data Center](#) (ICDC) University of Hamburg, Hamburg, Germany.

3.2 Methods

To follow the development of the Indian Ocean Dipole and the El Niño Southern Oscillation, the DMI and NINO 3.4 index are used, respectively. The data will be filtered with a running mean to investigate the long-term signals.

The upper panel of Figure 11 shows the absolute dynamic topography averaged over the full temporal range of the dataset (1993-2014) for a part of the southern Indian Ocean. This graph is made after Figure 11c of Palastanga *et al.* (2006) (shown in the lower panel of Figure 12). The authors, used a different definition of the absolute dynamic topography: they used a different reference geoid, resulting in different H_G values. Their values for the region shown in Figure 11 are least 161 cm, in the graph below the values are no more than 140 cm. Palastanga *et al.* (2006) defined their boundary between the Tropical Gyre and Subtropical Gyre as the 203 cm contour, which extends to 93°E and, on average, 14°S. In the graph below, the line that runs closest to that position is the 85cm contour. To follow the extend of the gyres, Hovmöller diagrams are made of the absolute dynamic topography as a function of time between 5°S and 22°S at longitudes between 40°E and 115°E, one at each longitude that is of 5°E more to the east than the former. Further, a box is drawn in Figure 11 below, which ranges from 22°S to 5°S and from 72.5°E to 77.5°E. This longitudinal range is approximately centred in the west to east region where the Tropical Gyre on average is located. Within this box, the longitudinally averaged latitudinal position of some values of the absolute dynamic topography are followed as a function of time. The Hovmöller diagrams and line plots of specific positions of H_G contours in the box can be used to follow the development of the gyres.

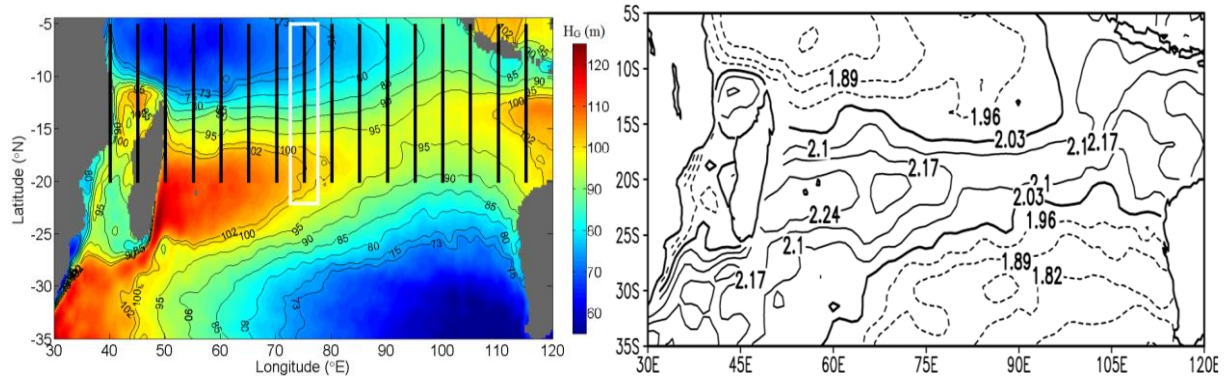


Figure 11 (left panel) Longitude versus latitude colour map of the 1993-2014 mean absolute dynamic topography (H_G), with units in cm. The contours also represent the absolute dynamic topography in cm. The absolute dynamic topography is used to investigate the position of the Tropical and Subtropical Gyre. Along the dotted lines, spaced by 5° and running between 22°S and 5°S , Hovmoller diagrams of H_G are made as a function of time and latitude. Within the white box, covering the area between $[72.5^\circ\text{E}, 77.5^\circ\text{E}] \times [20^\circ\text{S}, 5^\circ\text{S}]$, the latitudinal position of absolute dynamic topography equal to 73 cm, 75 cm, 80 cm, 85 cm, 90cm, 95 cm, 100cm and 102cm are retrieved as a function of time. The 85cm contour resembles the 203 cm contour in the lower panel. (right panel) Figure 11c of Palastanga *et al.* (2006), which represents the H_G in 2000 in meters. Dotted lines indicate the contours of absolute dynamic topography smaller than 203 cm, solid lines indicate contours values larger than 203 cm. The thick solid line marks the $H_G = 203$ cm line, which Palastanga *et al.* (2006) define as the boundary between the gyres. Each contour is spaced by 7 cm.

To track down changes in the equatorial winds as a function of time, the ERA-Interim dataset is used. This data will be filtered by a running mean to find the long-term signal. From the same dataset, wind differences between specific years over the entire southern ocean are determined to compare the wind field over the southern Indian Ocean before the MC and MS transports changed and after that time. These differences indicate where the surface winds have changed direction and/or magnitude in one year relative to the other.

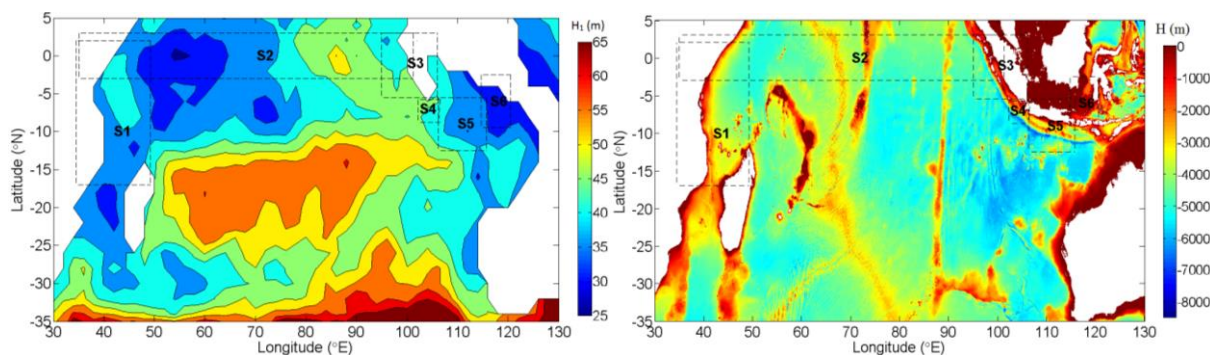


Figure 12 In order to derive the theoretical time Kelvin waves need to cross the Indian Ocean and reach Makassar Strait, bathymetry and thermocline data are used (see also Figure 9). For both baroclinic and barotropic Kelvin waves, the total track is divided in six parts. These are indicated in both panels. For each box, which is centred around one part of the total track, an average value of H_1 (left panel) and H (right panel) is determined and used to calculate the total ocean crossing time. (left panel) For baroclinic waves, 1961-2008 monthly mean top of thermocline depth (H_1) from IFREMER are used. Contours and colours in this longitude versus latitude map indicate constant values of H_1 . Contours are shown for values between 15 m and 65 m in steps of 5 m. Units of

the colour bar are in meters. (right panel) For the barotropic waves, bottom topography (H) from NOAA's National Centers for Environmental Information is used. The units in the longitude versus latitude map are in meters.

The total path for the Kelvin waves to travel is divided into six parts (see Figure 12). Over each part, the mean H_1 (baroclinic case) and H (barotropic case) is calculated within 2 degrees off the coast or Equator. The top of thermocline depth data is yearly averaged before it is used for further calculations. From H_1 and H , the mean travelling speed of the waves is calculated for the corresponding track according to the equations given in Section 2.4. Each track shown in Figure 12 is assumed to be linear and the distance travelled is calculated from the begin point and end point longitude/latitude pairs $[\phi_1, \theta_1]$ and $[\phi_2, \theta_2]$, respectively, via Equation (35) (Surowski (2011), with $R = 6378100$ m the mean radius of the Earth).

$$dr = 2R \operatorname{asin} \left(\sqrt{\sin^2 \left\{ \frac{\theta_2 - \theta_1}{2} \right\} + \cos\{\theta_1\} \cos\{\theta_2\} \sin^2 \left\{ \frac{\phi_2 - \phi_1}{2} \right\}} \right) \quad (35)$$

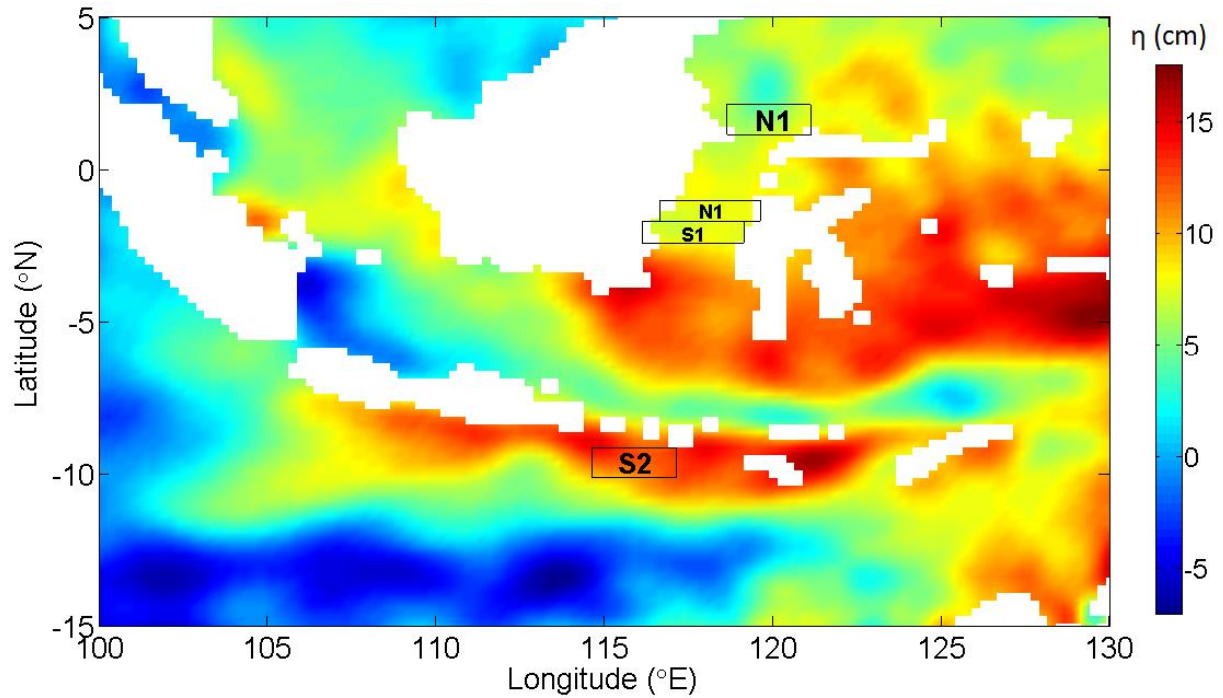


Figure 13 Longitude versus latitude map of the sea level anomaly averaged between January 2006 to April 2006. Units are in centimetres. The difference in AVISO sea level anomaly for Makassar Strait as a function of time is determined between two sets of boxes: between the location of the INSTANT moorings, N1, and just below that, S1, and between the northern entrance of Makassar Strait, N2, and below Lombok Strait and Timor Strait, S2.

To follow the changes in the sea level elevation anomaly, AVISO sea level anomaly (η) data is used. First of all, snapshots of the southern Indian Ocean ($[35^\circ\text{E}, 125^\circ\text{E}] \times [30^\circ\text{S}, 5^\circ\text{N}]$) running mean filtered sea level anomaly at specific times are analysed. Second, differences between the spatial averages of different areas close to the INSTANT moorings are determined

as a function of time and filtered by a running mean. There are two sets between which the differences in η is analysed (see Figure 13):

1. Between the Makassar Strait INSTANT moorings site and one degree southward, so between 3°S (N_1) and 4°S (S_1)
2. Between the northern edge of Makassar Strait (N_2) and south of Lombok Strait and Timor Strait, where the most of the ITF enters the southern Indian Ocean (S_2).

The difference in sea level anomaly between N_1 and S_1 represents the change in sea level close to the moorings, which is most likely having the most direct effect on the transport observed at 3°S . The sea level anomaly difference between N_2 and S_2 represents the changes over the entire strait. The resulting difference can be seen as a robustness test of the sea level anomaly difference over the entire Makassar Strait.

In this report, sea surface current zonal (u) and meridional (v) velocity data from OSCAR will be used to monitor the changes in volume transport by the southern Indian Ocean currents. By doing this, the assumption is made that currents in these regions are linear. Since the SEC and equatorial currents are large scale phenomena and are far from the coasts and tips of islands and continents, this is a reasonable assumption. Further, it is assumed that the sign and the magnitude of the surface current velocities represent the surface volume transport direction and magnitude, respectively.

The OSCAR data is used to derive the yearly mean difference in u and v between specific years over the southern Indian Ocean. These differences indicate where the surface flow has changed direction and/or magnitude. Differences are derived between $[30^{\circ}\text{E}, 150^{\circ}\text{E}]$ and $[35^{\circ}\text{S}, 5^{\circ}\text{N}]$.

OSCAR data will also be used to monitor the strength and position of specific currents. By averaging the zonal velocity over a meridional transect, the strength of a zonal current can be followed in time. Figure 14 shows the transects used to follow the strength of the equatorial zonal currents. The figure also shows SEC1 and SEC2, which are two bands between which the South Equatorial Current is thought to be present. The SEC is usually assumed to be positioned between 10°S and 15°S (the line indicated as SEC1, see Ridderinkhof *et al.*, 2010; Aguilar-González *et al.*, 2016), which gives SEC1. However, the SEC can vary its meridional position and if the gyres shift northward, the SEC could shift northward too (Aguilar-González *et al.*, 2016). In order to take the possibility into account that the SEC could shift, the flow velocity between 5°S and 10°S (SEC2) is also tracked, which gives SEC2.

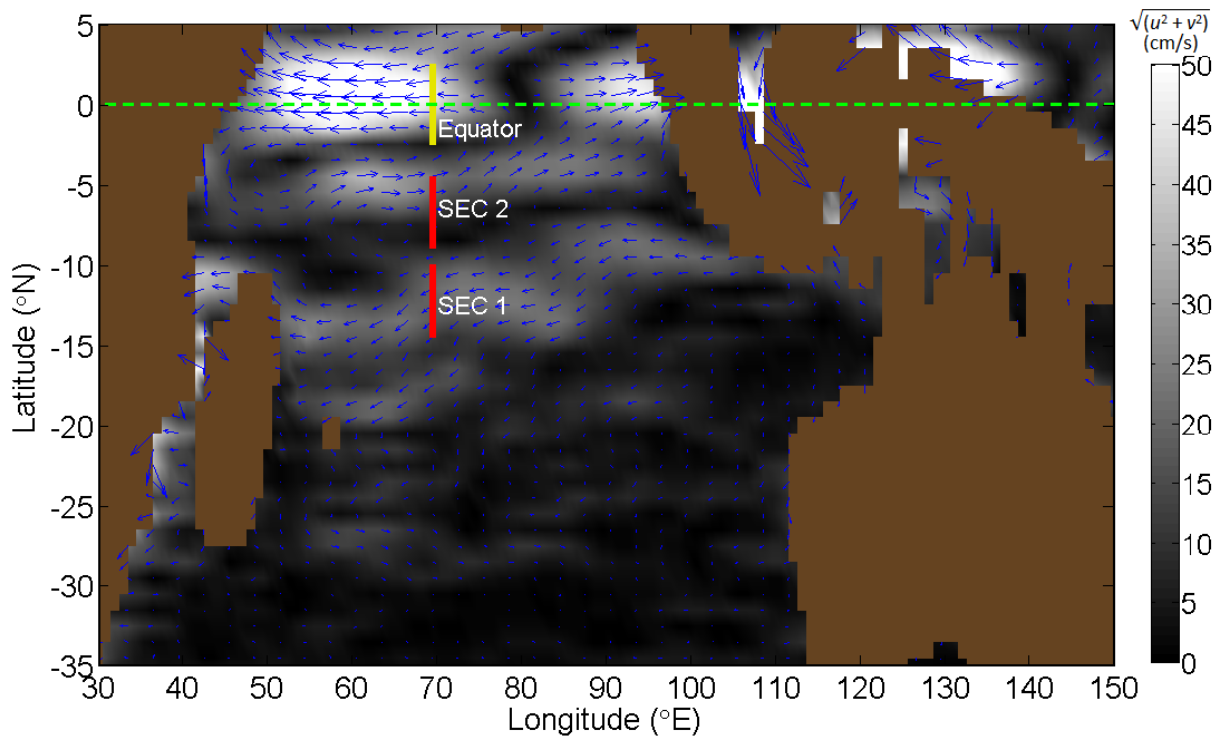


Figure 14 Longitude versus latitude snapshot of the monthly mean OSCAR surface current velocity magnitude (indicated in cm by the white-grey colour map) and direction (indicated by the blue vectors; the vectors scale with flow magnitude) for March 2006. The current velocity is analysed via longitude versus latitude plots, having the same zonal and meridional range as this panel, of differences between specific years for the southern Indian Ocean. Transect averages are analysed for the SEC (red sections) at its usual position (SEC1, between 10°S-15°S) and 5 degrees north of that (SEC2, between 5°S-10°S). Also for the equatorial currents, the zonal surface velocity is determined over a meridional section (between 2°S and 2°N). All three sections are located near the centre of the southern Indian Ocean, at 70°E.

4. Results

The main part of this section is dedicated to analysis of observational data. The Dipole Mode Index will be analysed (Section 4.1), as well as the position of the SEC (Section 4.2), the position of the gyres (Section 4.3), the feedback between IOD, ENSO and surface wind (Section 4.4), the Indian Ocean crossing time of equatorial Kelvin waves (Section 4.5) and the evolution of the sea surface elevation near Makassar Strait (Section 4.6). Section 4.7 is reserved for analysis of model data on wind-forced ocean circulation and the connection of these results to actual observations.

4.1 Transition of the Indian Ocean Dipole

From 2004 to 2010, the weekly Dipole Mode Index is shown in Figure 15. The 210 days running mean represents the general pattern of the original data. The 210 days running mean shows a strong transition in the first half of 2006. The long-term DMI signal changes from being weakly negative into strongly positive values. This transition starts a few weeks before the MC transport is changing and the actual sign change is at about the time the MC transport is changing. Initially, these positive values are of large magnitude, and after a year, the DMI

evolves into an alternating signal of moderately to weekly positive values. 2008 is an exception year, in which the DMI is weekly negative at the beginning of the year.

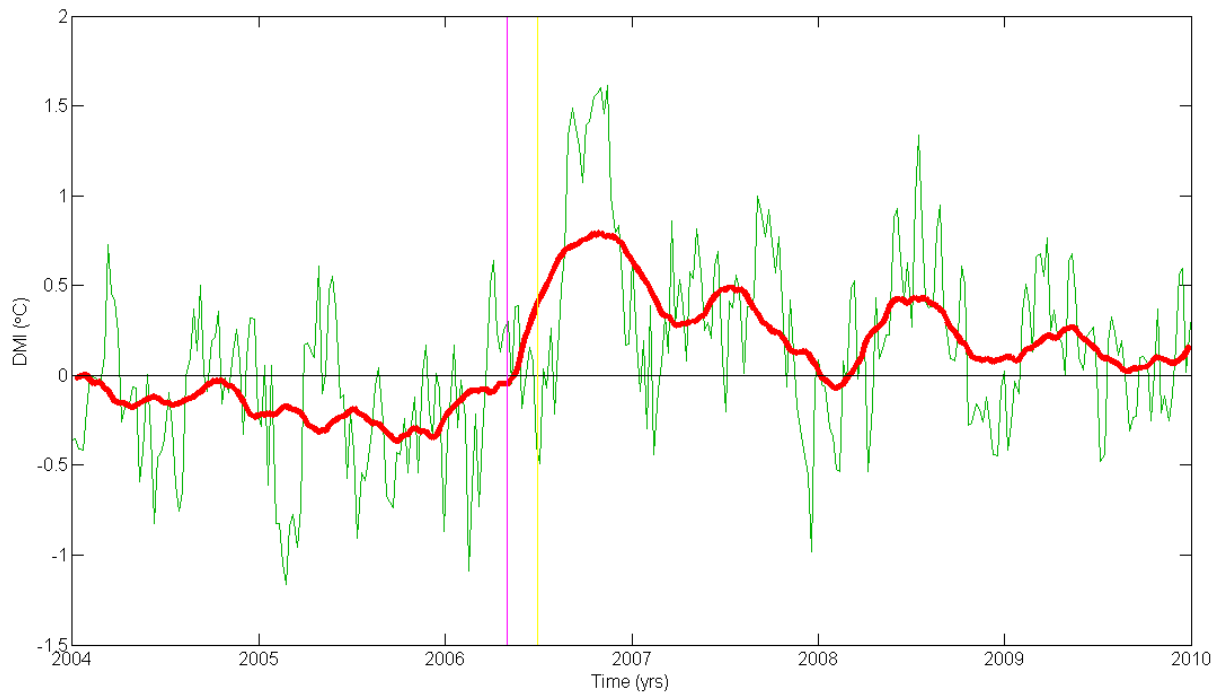


Figure 15 Dipole Mode Index (DMI) in degrees Celsius as a function of time in years. The thin green line shows weekly raw DMI, the thick red line the 210 days running mean of the DMI. The magenta and yellow line indicate the approximate timing of the transition of Mozambique Channel throughflow and Makassar Strait throughflow, respectively.

Overall, the long-term behaviour of the DMI has thus changed in the first half of 2006. Before that time, the DMI was negative. After that time, the DMI signal turned into a signal with, in general, positive values.

4.2 Position of the South Equatorial Current

In literature, a direct link is made between the weakening of the SEC and a positive IOD east to west temperature gradient. In this report, it is however suggested that the SEC makes a meridional shift rather than getting weaker (see further Section 2.2).

To get a first clue on whether or not the strength and/or the position of currents like the South Equatorial Current has changed, the surface current velocities over the entire southern Indian Ocean are investigated after 2006 in contrast with those before 2006.

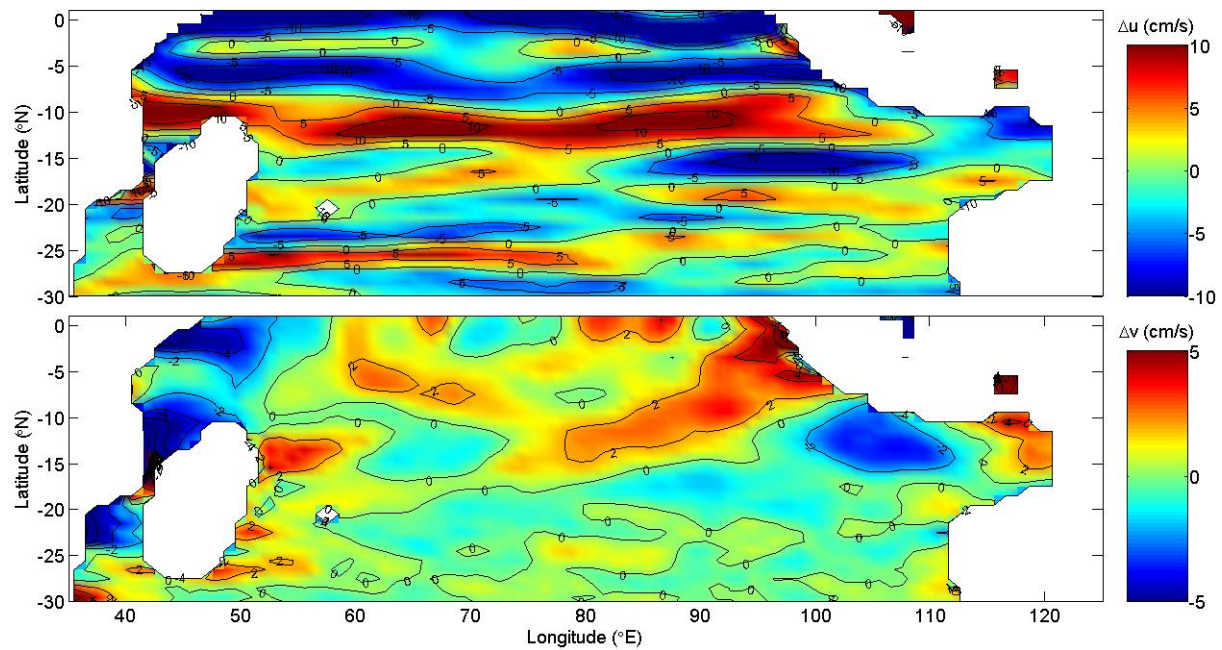


Figure 16 Latitude versus longitude map of the annual difference in zonal (top: Δu) and meridional (bottom: Δv) velocity for 2007 with respect to 2005. Units are in cm/s. Negative/positive values for the zonal (meridional) velocity component indicate more west(south)ward/ east(north)ward velocities in 2007 compared to 2005.

Figure 16 shows the annual difference in the zonal and meridional surface currents of 2007 with respect to 2005. In general, meridional current velocities at latitudes more north than 12°S have become more northward, except for a band of a few degrees off the coast of Africa. The latter resembles the increased southward transport in and around the Mozambique Channel.

For the zonal currents, the most notable patterns in surface velocity differences can be found at the Equator and between 15°S and 5°S. First, the latter region will be investigated. Compared to 2005, the 2007 zonal currents have become more eastward at the band 15°S-10°S, whereas the zonal currents between 10°S-5°S have become more westward. For both bands, the annual difference of the 2007 zonal currents with respect to those of 2005 is of the same sign for the entire width of the Indian Ocean. There is thus a basin wide uniform sign contrast between these two latitude bands concerning the difference of the annual zonal surface velocity for 2007 with respect to that of 2005. This is a hint for a possible shift of the SEC.

If the SEC did indeed shift between 2005 and 2007, the changes in the zonal velocity found in Figure 16 between 10°S-5°S and 15°S-10°S should occur approximately simultaneously. To see whether that did actually happen, the meridional mean u at SEC1 and SEC2 (15°S-10°S at 70°E and 10°S-5°S at 70°E, respectively, see also Figure 14) is monitored. The 3 months running mean curves of the SEC1 and SEC2 zonal currents are shown in Figure 17. The graph shows a clearly increased (reduced) westward surface flow velocity at the SEC2 (SEC1) section just before the transitions in MC and MS transports occur.

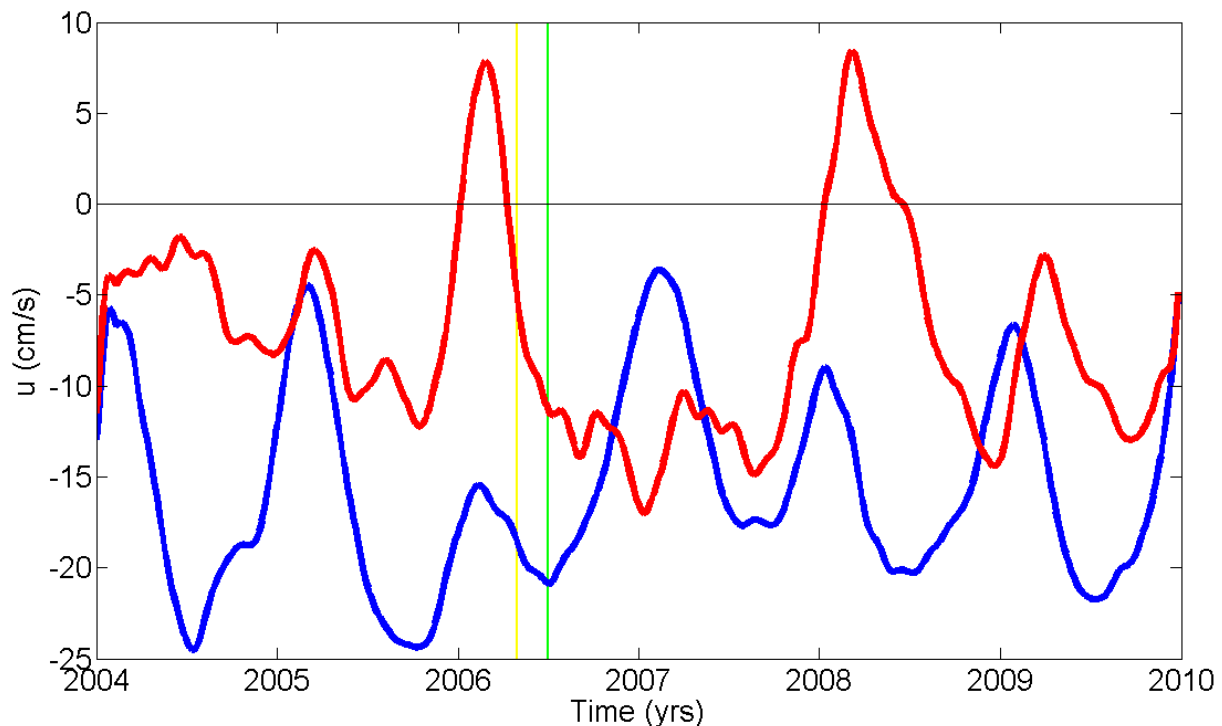


Figure 17 Zonal velocity through SEC1 (blue) and SEC2 (red) (see Figure 15), both in cm/s and as a function of time in years (see also Figure 14). The values are filtered by a 90 days running mean. For clearness, the raw data is not shown (it is found to show similar but more fluctuating patterns). The yellow and green line indicate the approximate timing of the transition in MC transport and MS transport, respectively. The SEC1 and SEC2 zonal velocities show out of phase behaviour most of the time.

The signal in the SEC1 shows a tendency to recover from the transition, but on average it stays less westward than before the changes occurred. A short reduction in westward flow in the SEC2 section is seen around the beginning of 2008, after which the signal turns back to increased westward zonal velocity. Together, Figure 16 and Figure 17 indicate a shift of the latitude band of strong westward flow between 2005 and 2007 from 15°S-10°S to 10°S-5°S over the entire width of the southern Indian Ocean and by that a shift of the SEC.

The annual mean zonal currents at the Equator in Figure 16 also show a basin wide westward anomaly in 2007 with respect to 2005. This is a strong indicator of changes in the equatorial dynamics. It is also an indicator that the mechanism that drives equatorial Kelvin waves has changed between 2005 and 2007.

Figure 18 shows that the changes in the surface currents start approximately a few months before the Mozambique Channel and Makassar Strait transports start to change. The weakening of the equatorial zonal surface currents is an indication that the clockwise circulation has reduced in the Tropical Gyre, possibly due to a northward shift of the Tropical Gyre. A further analysis on the positioning of the Tropical Gyre and Subtropical Gyre as a function of time will follow in the next section.

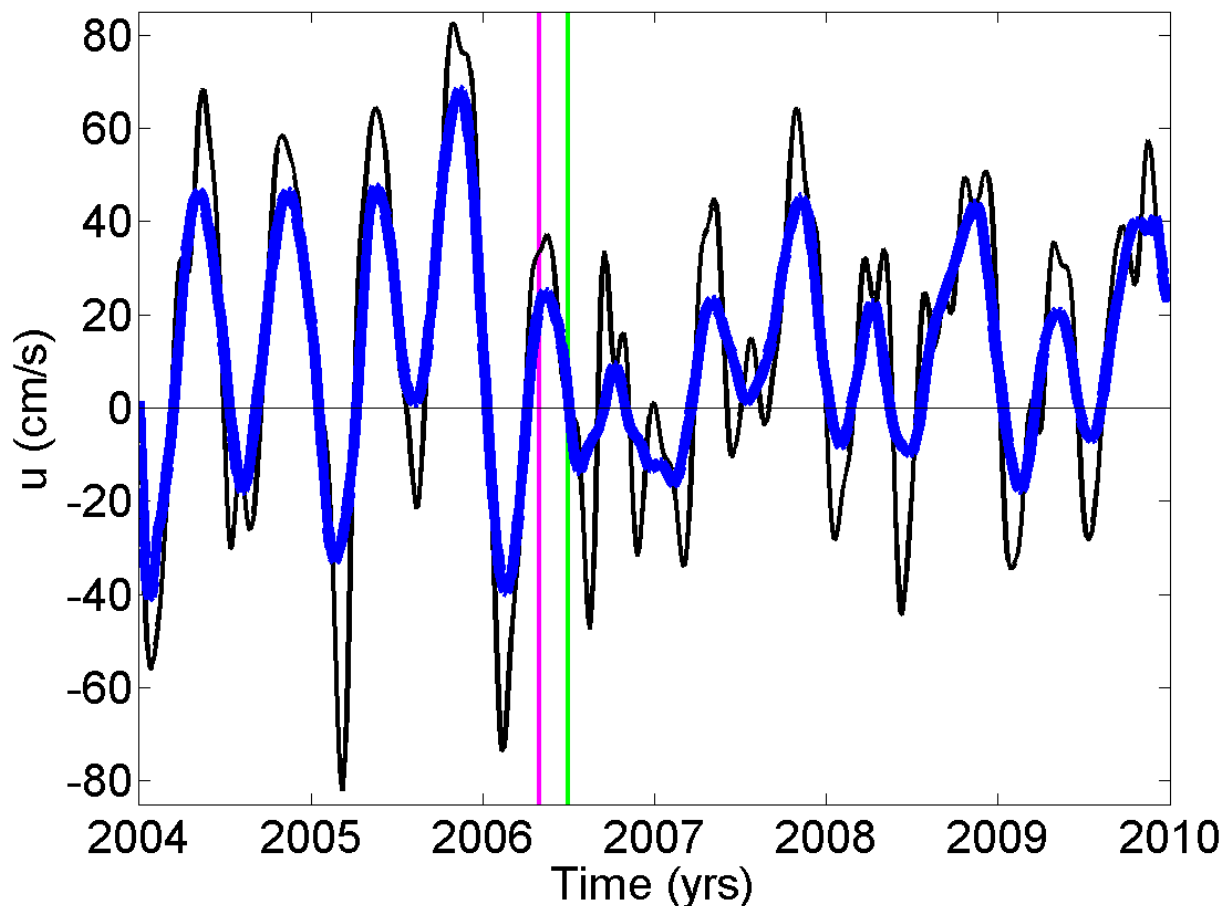


Figure 18 Zonal velocity at the Equator in cm/s. It exists of the meridional mean zonal current at 70°E between 2.5°S and 2.5°N (see also Figure 14). The black thin line shows the raw data, the thick blue line the data filtered by a 3 months running mean. The magenta line and blue line indicate, respectively, the approximate timing of the transition of the Mozambique Channel transport and Makassar Strait transport, respectively.

4.3 Position of the Tropical Gyre and Subtropical Gyre

To track the development of the position of the Tropical and Subtropical Gyre, the absolute dynamic topography in the southern Indian Ocean is tracked as a function of time. This is done both in the form of H_G Hovmoller (latitude versus time) and plots of the zonally averaged temporal latitudinal positions of specific H_G contours. See also Figure 11 for the track along which the latitude versus time Hovmoller diagrams will be made and the box within which the temporal latitudinal positions of the H_G contours will be determined.

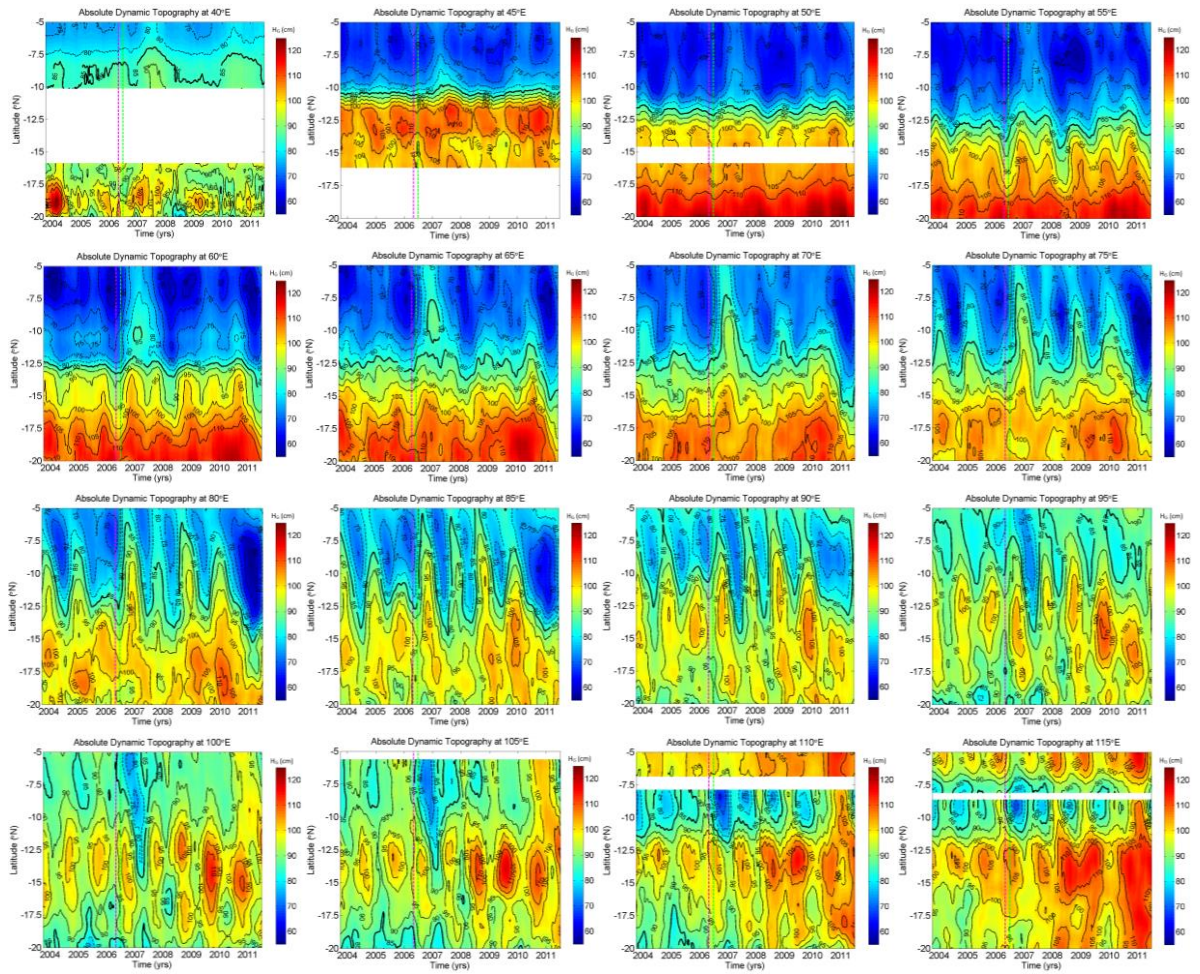


Figure 19 Latitude versus time Hovmöller diagrams of the absolute dynamic topography in cm at longitudes spaced by 5 degrees between 40°E and 115°E (see Figure 11). The data is filtered by a 210 days running mean and covers the latitude band 20°S-5°S and time period between January 2004 and July 2011. Magenta lines indicate when the Mozambique Channel transport approximately transits, green lines when the Makassar Strait transport approximately transits. The approximate boundary between the two gyres, the 85 cm contour, is indicated as a thick contour. Values smaller than 85cm are given by dotted contours, values larger than 85 cm are denoted by solid contours.

The latitude versus time Hovmöller diagrams of H_G are shown in Figure 19. At most longitudes, the contours smaller or equal to 85cm, and thus the Tropical Gyre and the SEC, show a northward shift. Between 40°E and 70°E, this shift is constant and lasts up to beginning 2008. East of 70°E, up to 90°E, the positions of the SEC and Tropical Gyre do also shift. Here however, the SEC and Tropical Gyre do not a shift that is constant in time. For longitudes between 70°E and 90°E, the Tropical Gyre and SEC are more northward between January-June and more southward between July-December. The trend of more northward positioning of the Tropical Gyre and the SEC during the first half of the year does however last until 2009.

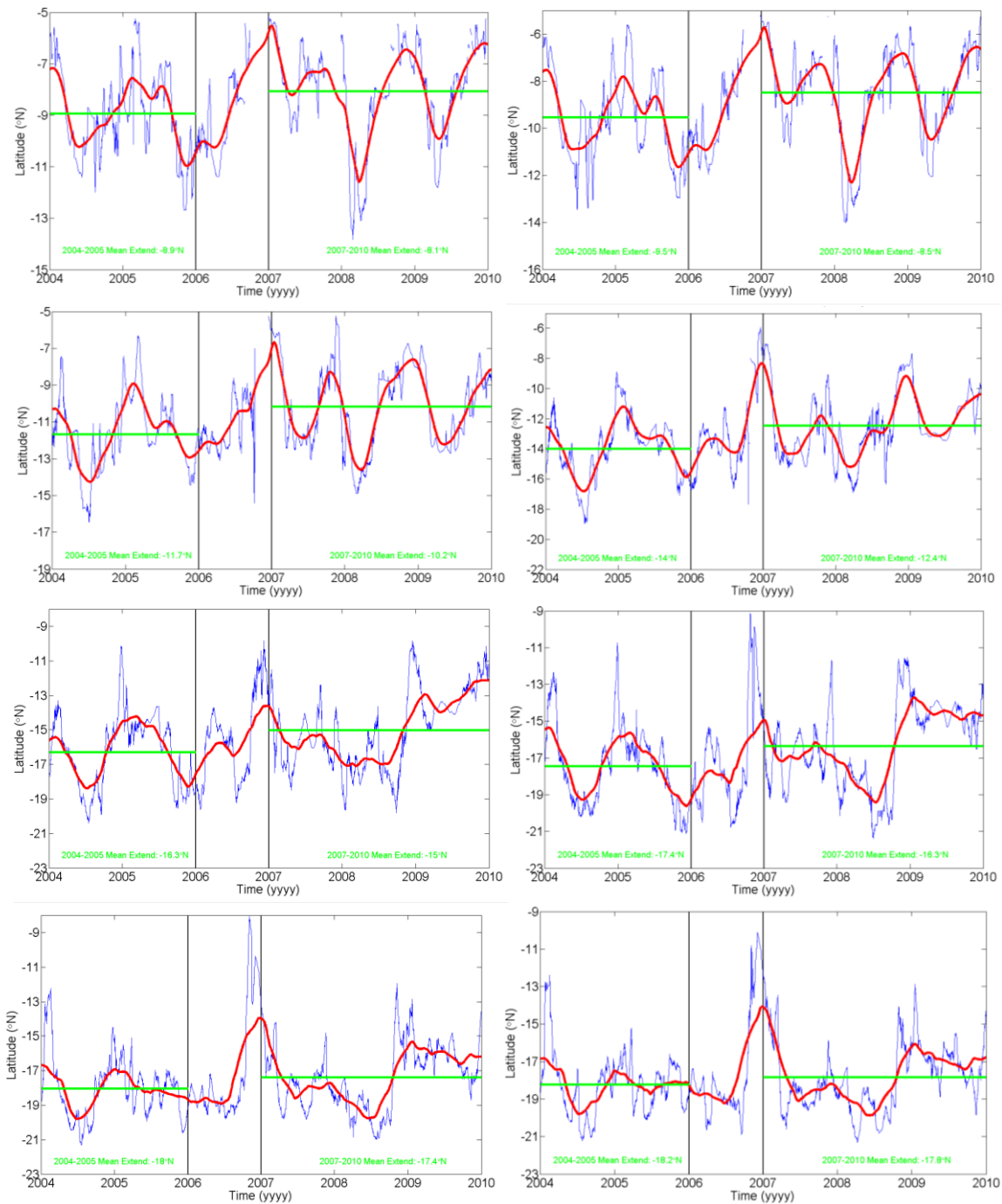


Figure 20 Time-evolution of the latitudinal extent of specific absolute dynamic topography contours in the range $[72.5^{\circ}\text{E}, 77.5^{\circ}\text{E}] \times [5^{\circ}\text{S}, 22^{\circ}\text{S}]$: (left column, top to bottom) 73cm, 80cm, 90cm, 100cm, (right column, top to bottom) 75cm, 85cm, 95cm and 102cm. The blue lines indicate daily values and the red lines 210 days running mean daily values. The green lines between 2004-2006 and 2007-2010 indicate the average positions of the contours for the accompanying period. Note that the limits on the vertical axis differ since the mean position of each contour shifts northward the smaller the H_G value followed becomes.

Most of contours larger than 85cm in Figure 19, and therefore the Subtropical Gyre, do not show a (semi) permanent shift to the north or to the south. It seems as though only a small part of this gyre undergoes a shift.

Figure 20 supports these findings. Contours that on average were positioned north of 12°S before the 2006, and thus in the region where the Tropical Gyre on average is located, show a permanent northward shift. The boundary between the gyres, the 85cm contour, makes a shift, but it is very small. The contours that, on average, are positioned south of the 85cm contour make a sharp northward jump in 2006, but also rapidly fall back to their original mean position. For many of these contours, a more or less permanent northward shift only takes place around 2009. This makes the mean position of these contours indicated in Figure 20 for the period 2007-2010 a little bit suggestive. The positions of the H_G contours larger than 85cm position show much fluctuation in this period and their annual mean temporal latitude even seems to undergo a northward transition around 2009. This difference in behaviour makes the total mean latitudinal extent of these contours over the entire period 2007-2010 to lose much of its meaningfulness. For contours positioned north of the 85cm contour, the curve has a more consistent temporal behaviour in the period 2007-2010, making its mean position for that time much more meaningful. On average, these contours show an annual mean northward shift of about 1.5 degrees.

Figure 19 and Figure 20 thus imply that the Tropical Gyre and SEC underwent a northward shift around May 2006. Apart from 2006, the Subtropical Gyre seems to stay where it used to be up to at least 2009.

4.4 Sea surface temperature and sea surface wind

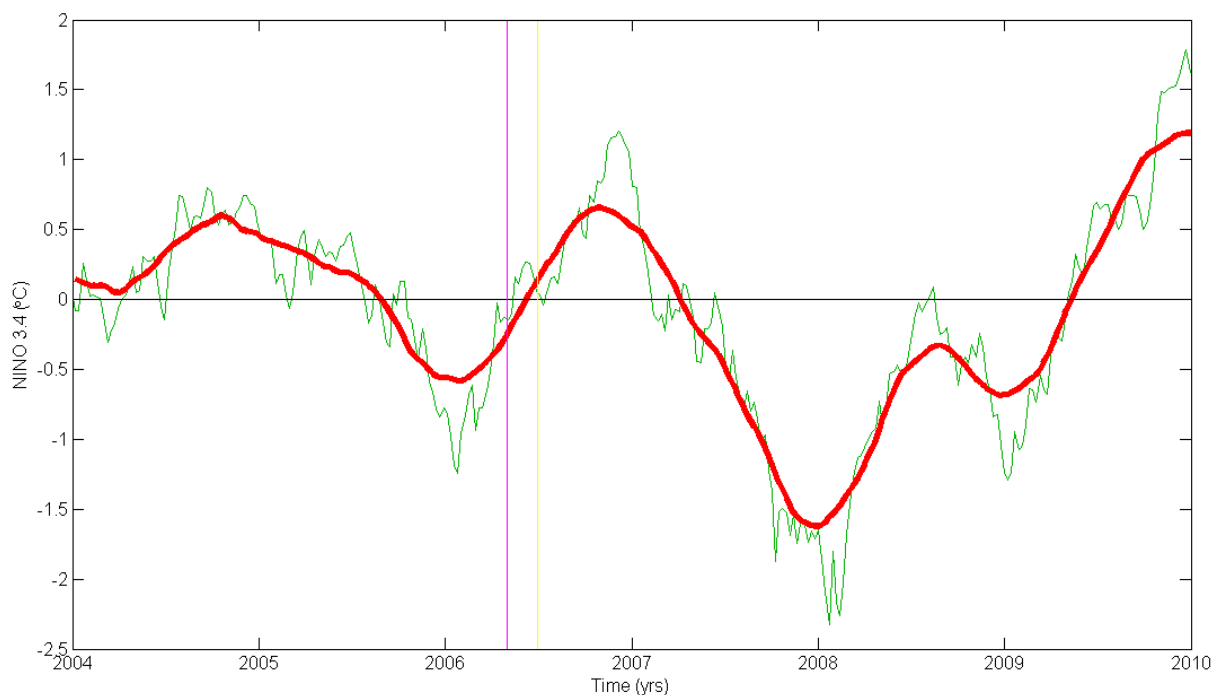


Figure 21 5-days mean values of the NINO 3.4 index in degrees Celsius as a function of time. The raw values are plotted in green and the 210 days running mean NINO 3.4 values are given by the thick red line. The magenta and yellow lines represent, respectively, the timing of the transitions in Mozambique Channel transport and Makassar Strait transport.

Now that the link between the IOD and the position of the gyres has been investigated, attention can be turned to the link between the IOD and the sea surface winds. Since for Makassar Strait also the relation between the ENSO and the Pacific Ocean surface winds will be analysed and IOD serves a similar role in the Indian Ocean as ENSO does in the Pacific Ocean, first the long-term evolution of ENSO will be analysed. Then, attention will turn to both relations between IOD (ENSO) and Indian (Pacific) Ocean sea surface winds.

In Figure 21, both the raw and 210 days running mean NINO 3.4 index is shown as a function of time. The long-term signal shows a fluctuation around near zero up to 2006 and a fluctuation around negative values between 2007 and 2009, so about one year before the Makassar Strait undergoes its second transition to increased southward flow.

Since the state of both ENSO and IOD can be important for the transport through the Makassar Strait, the long-term evolution of their accompanying climate indicators is investigated. Figure 22 shows the time variation of the 7 months running mean filtered DMI and NINO 3.4 index under each other. Up to 2006, the DMI is mainly negative. The NINO 3.4 index is just fluctuating from year to year between 2004 and 2006. In 2006, both indices are positive. The two years after that, the DMI and NINO 3.4 index are out of phase, with the DMI in general being positive and the NINO 3.4 index mainly being negative. Thus, starting in 2006, the DMI is mainly positive and from 2007 on, the mainly positive DMI is accompanied by a mainly negative NINO 3.4 index. The states of the oceans only change again around the second half of 2009 (ENSO) and beginning of 2010 (DMI).

In literature noted in Section 3.1, one generally looks up the NINO 3.4 index that is smaller (larger) than -0.5°C ($+0.5^{\circ}\text{C}$) for at least 5 consecutive months. All months that are two months of the beginning and end of the period with NINO 3.4 smaller (larger) than -0.5°C ($+0.5^{\circ}\text{C}$) are defined as La Nina (El Nino) months. Other months are seen as neutral. A similar constraint can be defined for the DMI to indicate positive and negative IOD events: if it is smaller (larger) than -0.25°C ($+0.25^{\circ}\text{C}$) (the smaller magnitude of 0.25°C is chosen since DMI rarely exceed 0.5°C) for at least 5 months, then the months of this full period except the outer two are defined as negative (positive) IOD event months. Other months can be seen as neutral IOD events.

Via these two constraints and accompanying definitions, the above findings on Figure 20 can be formulated in general terms of La Nina and El Nino and positive and negative IOD event periods. Up to 2006, both IOD and ENSO are neutral. In 2006, a positive IOD event is accompanied by an El Nino state. The two years after that, the Indian Ocean and Pacific Ocean are characterized by a positive IOD event and a La Nina state, respectively, so the sea surface temperature state of the two oceans are out of phase. The states of the Indian Ocean changes again around into a neutral IOD event state in the first half of 2008, which stays like that except for the second half of 2010 (negative IOD event). The Pacific Ocean undergoes two more changes after 2008: it turns into an El Nino state in the second half 2009 and a La Nina state beginning of 2010.

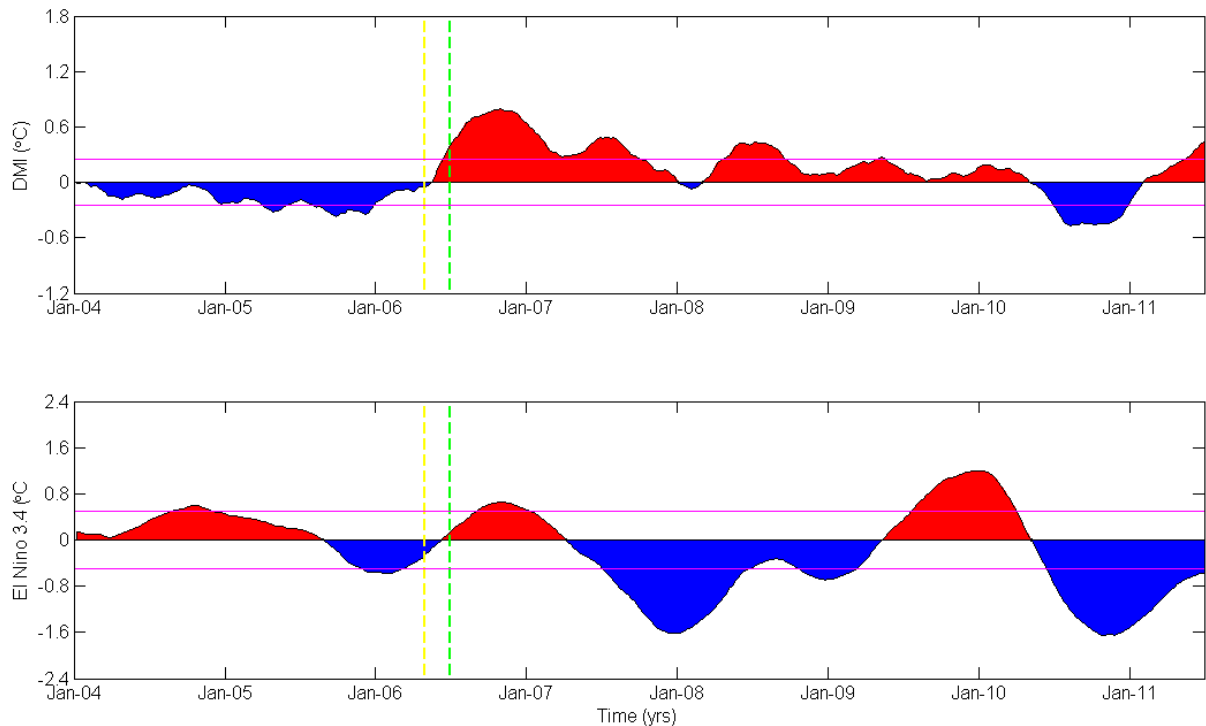


Figure 22 Weekly Dipole Mode Indices (top panel) and weekly NINO 3.4 indices (bottom panel), both filtered with a 210 days running mean. Yellow and green lines indicate when the MC transport and MS transport, respectively, approximately transit. The magenta lines indicate the $[-0.5^{\circ}\text{C}, 0.5^{\circ}\text{C}]$ range. Periods longer than 5 months with indices below/above this range are characterized as La Nina/El Nino periods.

To link the trade wind velocity over the specific oceans to the long-term IOD (210 days running mean DMI) or ENSO (210 days running mean NINO 3.4 index) state, it should be represented well too by a 210 days running mean. Figure 23 shows the zonal wind velocity along the Equator at the western and eastern half of the Indian Ocean. Figure 23 shows two things. First of all, it indicates that the 210 days running mean is a good representation of the shape and magnitude of the zonal wind velocity pattern. Secondly, Figure 23 shows that the equatorial zonal wind undergoes a transition around May 2006, from being mainly eastward to being mainly westward. The transition occurs earlier in the western half than in the eastern half, so any influences that are caused by the changing wind are induced in the western Indian Ocean first. The changes in the equatorial wind occur in the west earlier than in the east, and thus closer to the MC than to the MS. Therefore, it is possible for an event that follows from these changing winds or the mechanism causing the wind changes to first influence the MC transport and then the MS transport.

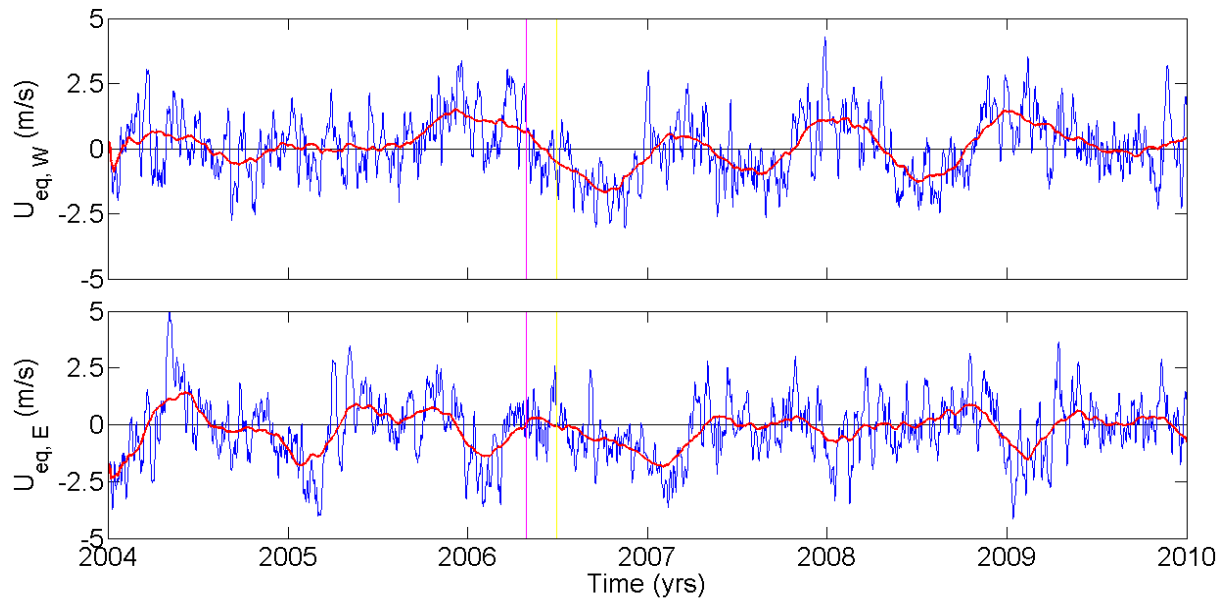


Figure 23 Trade wind velocity in m/s over the Indian Ocean averaged for (upper panel) the western Indian Ocean ($U_{eq,W}$: 30°E and 80°E) and (lower panel) the eastern Pacific Ocean ($U_{eq,E}$: 80°E and 120°E) as a function of time in years. Meridional zonal wind averages are taken between 5°S and 5°N. Blue lines indicate raw daily values, thick red lines 210 day running mean daily values. The magenta and yellow lines mark the approximate timing of the transport transition in the Mozambique Channel and Makassar Strait, respectively.

Figure 24 shows the Pacific Ocean trade winds averaged over the Pacific Ocean. It can be seen that the long-term wind, as do the Indian Ocean trade winds in the first half of 2006, also becomes stronger westward, in this case starting in the third quarter of 2006. The Pacific trade winds stay stronger westward up to at least mid-2010.

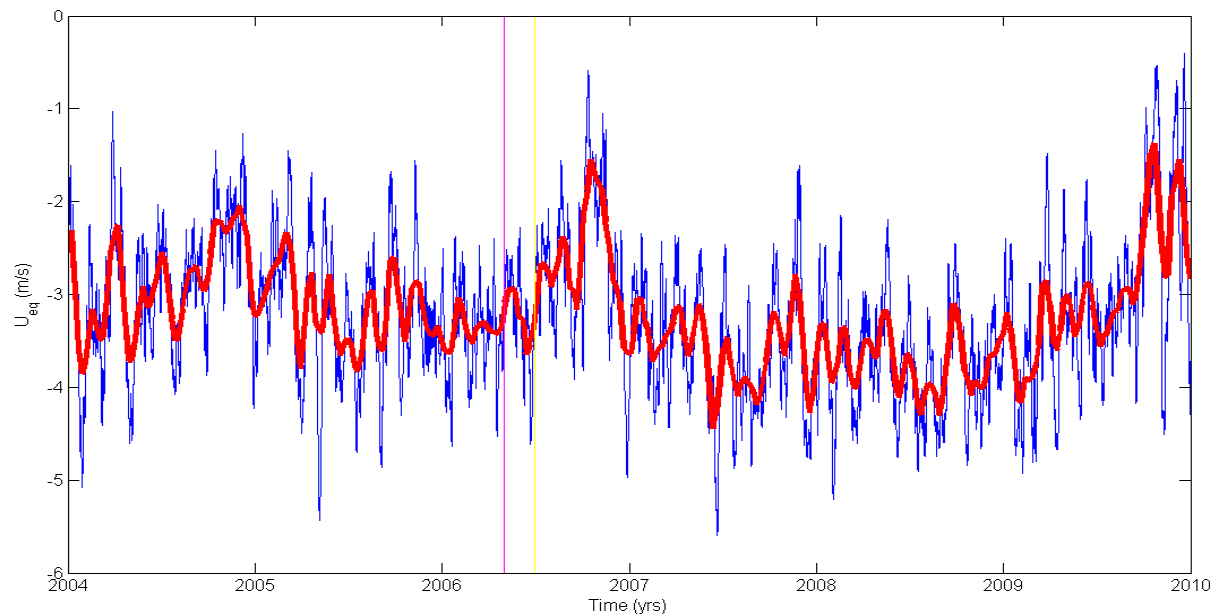


Figure 24 Zonal equatorial wind velocity over the Pacific Ocean averaged between [120°E, 285°E] and [5°S, 5°N]. The blue line indicates daily values, the red line 210 day running mean values. The magenta and yellow lines mark the approximate timing of the transport transition in the Mozambique Channel and Makassar Strait, respectively.

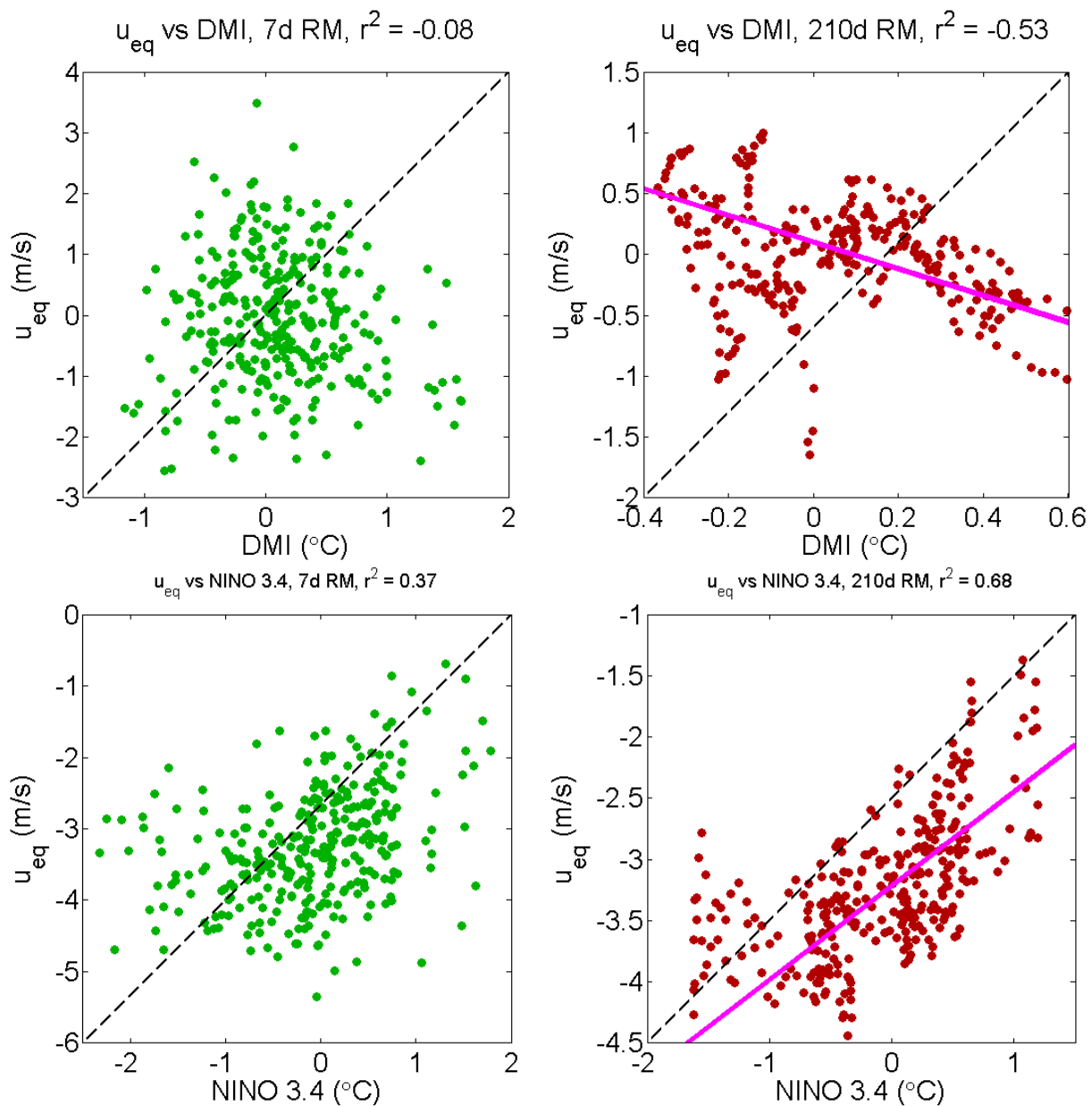


Figure 25 Scatter plots of (top left panel) weekly values and (top right panel) 201 days running mean values of the equatorial Indian Ocean zonal wind, averaged between 30°E and 120°E , and the DMI and between (bottom left panel) weekly values and (bottom right panel) 210 days running mean values of the equatorial Pacific wind, averaged between 120°E and 285°E , and the NINO 3.4 index. The magenta lines in the top right and bottom right panels indicate the best linear fit to the data plotted in red. The correlation coefficients mentioned on top of the panels are valid for all the data in the unfiltered case and for the data in red for the filtered case.

Figure 23 and Figure 24 have shown that the equatorial winds over the western half of the Indian Ocean and Pacific Ocean stay westward for a long time. These westward winds could initiate upwelling Kelvin Waves in the oceans. Over the eastern half of the Indian ocean, the equatorial winds keep seasonally fluctuating between being westward and eastward. For at least two years, however, the westward winds are enhanced whereas eastward winds are weakened.

The eastern Indian Ocean equatorial winds might thus either strengthen upwelling Kelvin waves for times with westward winds or weak down upwelling or create weak downwelling Kelvin waves for the weak eastern winds present over parts of the Indian Ocean. The combined effect of the overall westward trade winds is that both over the Indian Ocean and Pacific Ocean upwelling Kelvin waves could be initiated.

The basis of the mechanism proposed for explaining the changes in the MC transport and MS throughflow in Section 2.2 is Bjerknes feedback between sea surface heating and sea surface wind patterns. It is thus important to know whether or not the winds over the Indian Ocean (Pacific Ocean) correlate to the IOD (ENSO) state. To find out, Figure 25 is created. It shows scatter plots of the DMI (NINO 3.4 index) and the Indian Ocean (Pacific Ocean) trade winds, both for raw data and long-term data.

On short time-scales, the winds over the Indian Ocean and Pacific Ocean seem not to be correlated to the IOD and ENSO, respectively, based on Figure 25. On longer time-scales, however, a strong anti-correlation is found between the IOD and Indian Ocean equatorial winds and a strong correlation between the ENSO and the western Pacific Ocean equatorial winds. The changes in IOD state and ENSO state (see Figure 22) occur earlier than in the equatorial winds over the accompanying oceans (see Figure 23 and Figure 24). The Indian Ocean and Pacific Ocean sea surface temperature distribution thus co-vary with the trade winds over the corresponding ocean at a lack of a few weeks. The changes in the trade wind seem to enhance the strength of the IOD and ENSO and vice versa, which is an important characteristic of the Bjerknes feedback.

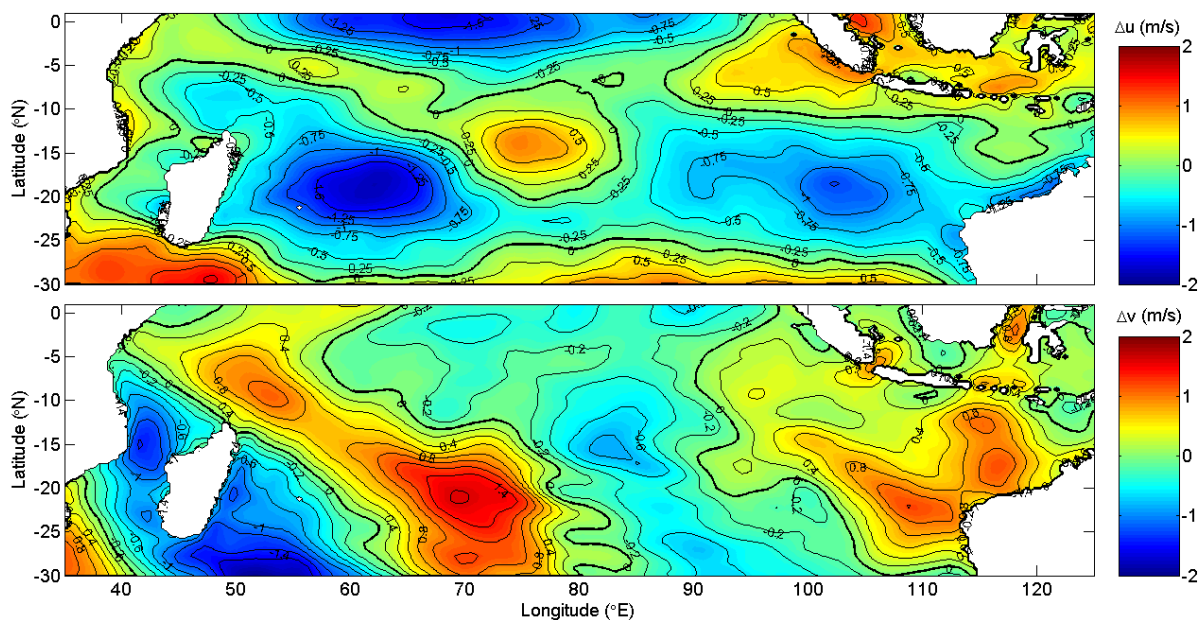


Figure 26 Latitude versus longitude map of the annual differences in ERA-Interim zonal wind velocity (ΔU) in m/s (top panel) and meridional wind velocity (ΔV) in m/s (bottom panel) for 2007 with respect to 2005. Positive values in the upper panel (lower panel) indicate that the velocity component in 2007 was more eastward or less westward (more northward or less southward) than in 2005 and vice versa.

To finally look if there might be other locations on the Indian Ocean where important changes in the wind occur between the period before the transports in MC and MS change and the period after that, Figure 26 is presented. Figure 26 shows the annual changes in the wind over the Indian Ocean zonal and meridional sea surface wind for 2007 with respect to those for 2005. The changes in equatorial zonal wind extend up to 5 degrees in latitude. This is far enough to cover the entire width of a equatorial Kelvin wave, which has an average width of about 2 to 5 degrees (see for example, Dijkstra, 2008; Cushman-Roisin and Becker, 2011) and thus to have a wind forcing over the entire width of an equatorial Kelvin wave.

There is also a small band of more eastward wind which extends, on average, between 10°S and 5°S. Slightly more westward winds are found, on average, between 20°S and 10°S. These zonal wind differences are however much weaker than those on the Equator.

The meridional wind, which for completeness is also shown, does not show one zonally uniform annual difference between 2005 and 2007: some zonal bands are subject to more northward wind in 2007, others to more southward wind. Far to the east, surface wind differences between 2007 and 2005 are even depending on latitude. Due to a lack of ocean wide uniformness, the meridional wind is thus not thought to have one general basin wide influence on the wind-driven circulation.

4.5 Kelvin Waves: barotropic mode versus baroclinic mode

The route which the Kelvin waves are assumed to take has been shown in Figure 12. To summarize the path: along the east African coast, the Equator, the Indonesian Archipelago and through the Makassar Strait. Using the bathymetry dataset described in Section 3.1, it is possible to calculate the time necessary to travel from one site to the other for first order barotropic Kelvin waves. For each part of the track, a separate value for H , c and t is determined. The latter quantity, t , is the time necessary to travel a specific part of the track. The results are shown in Table 3. Table 3 shows that the first order barotropic Kelvin wave cover the full distance within less than a day (last column of Table 3: total travel time, t_{tot}), making it way too fast to be the cause for the transport changes.

	H/H_1 (m)				c (m/s)				t (d)				t_{tot} (d)
	A	E	I	M	A	E	I	M	A	E	I	M	
BT	2413	4045	2334	707	154	199	151	83	0.10	0.52	0.14	0.11	0.87
BC	38	40	42	33	0.98	1.00	1.00	0.91	15	104	22	10	150

Table 3 Mean total ocean (H)/top of thermocline (H_1) depths, Kelvin wave travel speeds (c), and travel time (t) for the six tracks on the trajectory Mozambique Channel to Makassar Strait. Results for barotropic Kelvin waves are given in the row for BT, those for baroclinic Kelvin waves in the row for BC. Values belonging to the track Mozambique Channel to the equatorial coast at Somali are denoted by A (track 1), those for the equatorial western Indian Ocean to equatorial eastern Indian Ocean by E (track 2), those for the equatorial Sumatra coast to Lombok-Bali by I (mean result for track 3, track 4 and track 5) and those belonging to the track Lombok Strait to Makassar Strait by M (track 6). Between brackets, the tracks denoted in Figure 12 are mentioned. Values are valid for a first order Kelvin wave. Also mentioned is the total travel time (t_{tot}) for the two types of Kelvin waves.

The next step is to look at the first order baroclinic Kelvin waves by making use of the thermocline depth dataset which is described in Section 3.1. Table 3 shows the derived values of H_1 , H , c and t . This time, the derived total travel time t_{tot} is very close to the observed transport change delay: about half a year.

A first order baroclinic Kelvin wave is thus, in terms of timing, a possible candidate for being the cause of the observed transport changes. Possibly, the dynamics of the Kelvin waves has changed more gradually, since the IOD state already started to changes a few months before the MC transport was changing (see Figure 15).

4.6 Evolution of the sea level anomalies

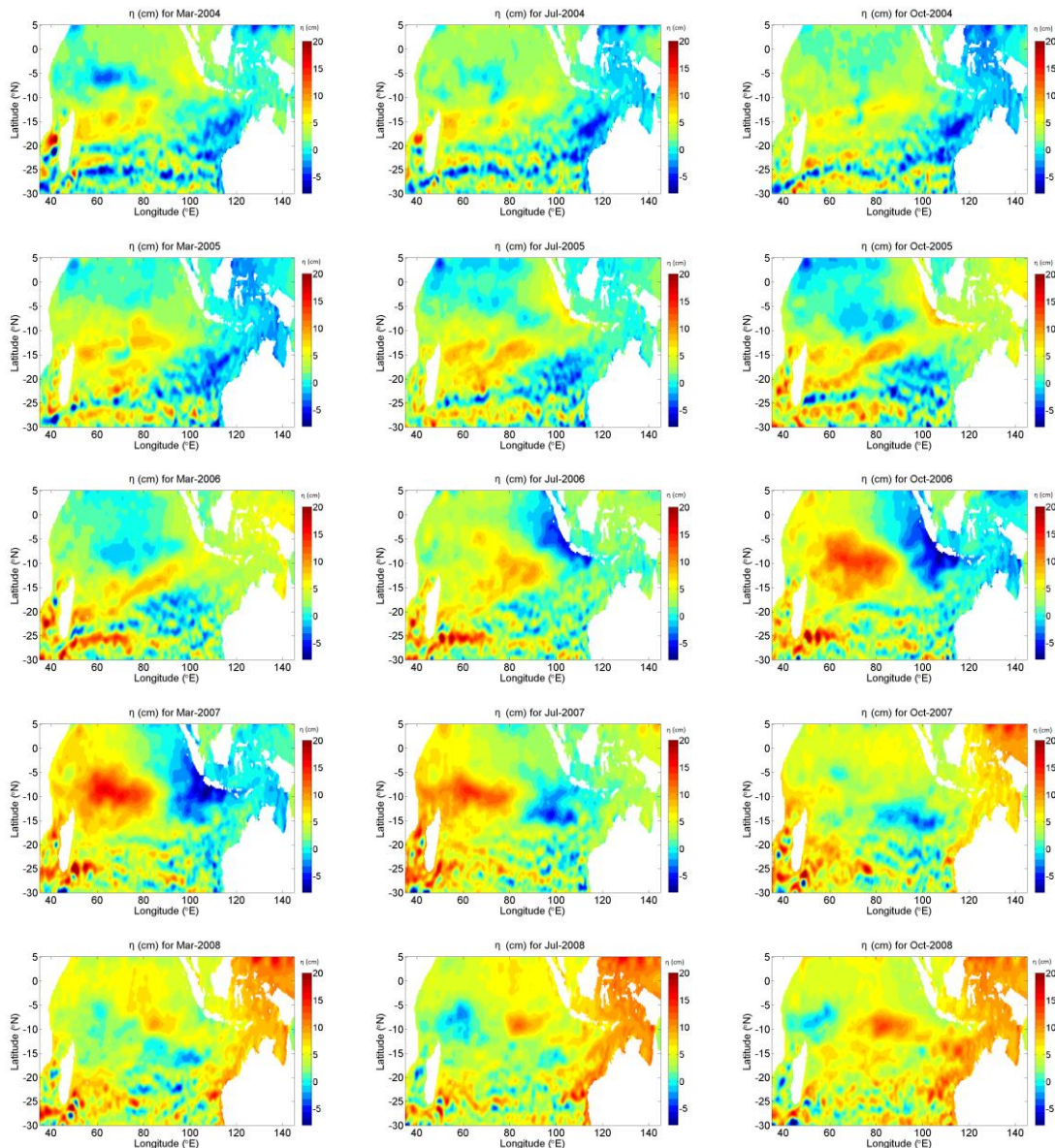


Figure 27 Sea level anomalies (η) in cm for the period 2004–2012. Each row represents one year. Each column contains yearly averaged values centred around a specific month for a specific year: May (left column), July (middle column) and October (right column). The maximum magnitude of the negative η is smaller than those of the positive η . Therefore, to easier distinguish the two and to keep the transition of the colour bar from cold colours to warm colour at zero, the colour bar is not put symmetric around zero, but has a larger tale for positive values.

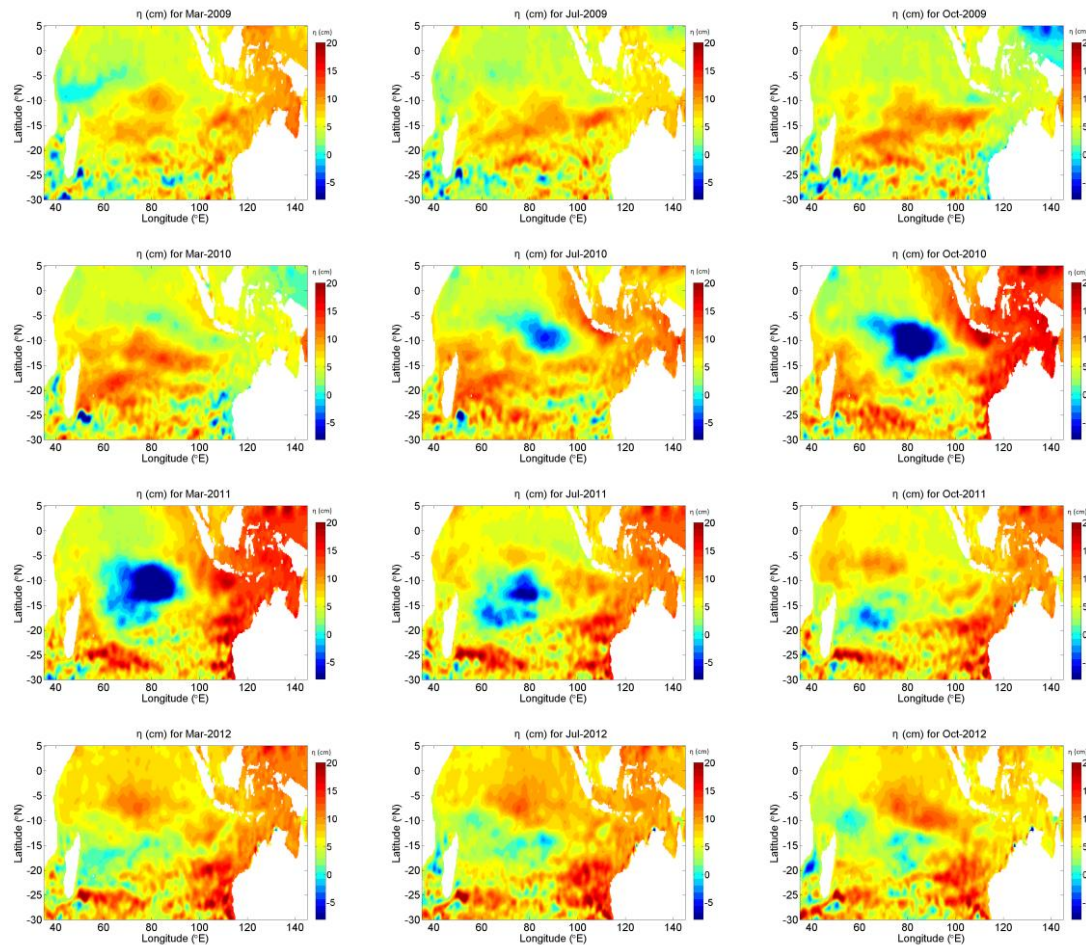


Figure 28 Continuation of Figure 27.

Figure 27 and Figure 28 show annual sea level anomalies over the Indian Ocean and a small piece of the western Pacific Ocean for different months around which the annual mean is taken. Up to March 2006, the sea level anomalies were mainly negative along the Equator, through the Makassar Strait and northwest of the southern Pacific Ocean. A trend of positive sea level anomalies can be seen east of northern Madagascar.

Between 2006 and 2007, a large pattern of negative sea level anomalies crossed the Equator to travel along Indonesia. When arriving at the East Indian Archipelago, this pattern of negative sea level anomalies lowered the sea level at the thoroughfares for ITF into the Indian Ocean. The anomaly seemed to partly pass the gateways south of the East Indian Archipelago into the Makassar Strait and to partly reflect on the coast around these gateways into a large pattern of positive sea level anomalies which travelled slowly towards northern Madagascar. This chronology of events indicates the splitting of a coastal Kelvin wave into a reflected baroclinic Rossby wave and a baroclinic Kelvin wave continuing its way to Makassar Strait at the gateways through the East Indian Archipelago.

At the same time the sea level began to get lower at Indonesian throughflow gateways, the sea level north of Makassar Strait began to rise. The timing was in phase with the onset of the La

Nina (see Figure 22) and the sudden rise in sea level anomaly north of Makassar Strait seemed to reach a maximum at the beginning of 2008.

The effect of the changes in sea level south of the ITF entrances into the Indian Ocean and north of Makassar Strait was the creation of a sudden increase of the north minus south sea level anomaly difference over the Makassar Strait in the first half of 2006 and at the start of 2008.

After the second half of 2008, the sea level anomalies turned into a more and more uniform field of positive sea level anomalies throughout the western Pacific Ocean, Makassar Strait and the eastern Indian Ocean. A big pattern of negative sea level anomalies travelled towards Madagascar, which eventually fell apart into smaller patterns of sea level anomalies which vary between values close to zero. Both the pattern of large negative sea level anomalies and the pattern of values close to zero did not seem to travel through the Mozambique Channel, which is in contrast to what the big pattern of positive sea level anomalies did in 2007.

The consecutive north to south difference at the MS in sea level anomaly ($\Delta\eta$ in the figures) due to changes in sea level anomaly pattern in the southern Indian Ocean and western Pacific Ocean is shown in the two panels of Figure 29. The figure shows, first of all, a sign change in the mean north to south difference in η during the transition in ITF in 2006. This can both be seen in the difference in η between the INSTANT moorings site and one degree to the south (the N1 minus S1 difference) and the difference in η between the northern entrance of Makassar Strait and the entrance region of ITF into the southern Indian Ocean (the N2 minus S2 difference). The sign change is larger for the N2 minus S2 difference than for the N1 minus S1 difference. After the sudden shift to a positive mean, the mean value of both the N2 minus S2 difference and the N1 minus S1 difference slowly decreases in time.

Secondly, Figure 29 shows that, at the beginning of 2008, the mean N2 minus S2 difference and the mean N1 minus S1 difference make another transition to large positive values. These mean values stay more or less the same up to the second half of 2009, when the mean values stagnate again to turn into negative values.

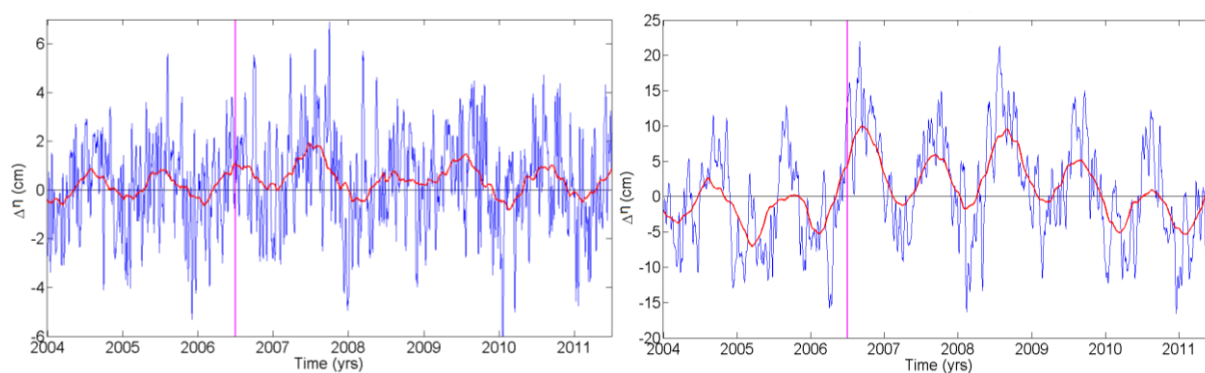


Figure 29 (left panel) Difference in sea level anomaly ($\Delta\eta$) in cm as a function of time in years between the boxes N1 and S1 in Figure 14. It represents the difference in sea level anomaly between the northern entrance of the Makassar Strait and the ITF entrance into the Indian Ocean. (right panel) Difference in sea level anomaly ($\Delta\eta$) in cm as a function of time in years between the boxes N2 and S2 in Figure 14. It defines the differences in sea level anomaly between the site of the INSTANT moorings and one degree more to the south. In both panels, the blue line indicates daily values and the thick red line 210 days running mean daily values. The magenta line indicate the approximate time of transport transition in the Makassar Strait (July 2006).

Figure 29 thus indicates, given the relation between η and the thermocline elevation, a reversal in north to south tilt of the thermocline depth at the MS in July 2006 and an increase of this south to north (north to south) elevation of the sea level (thermocline) elevation at the beginning of 2008. Near 2009, these elevations turn slowly seem to turn back to their original states.

4.7 Model results on baroclinic flow around an island

Introduced in Section 2.1 was the formulation of the interior Sverdrup flow and Stommel boundary layer dynamics, both for oceans with and without an island. The first step in investigating flow around an island is to reproduce the flow in a basin without an island, which only has a Stommel boundary layer in the west and interior Sverdrup flow elsewhere.

Figure 30 shows a plot of the Sverdrup/Stommel flow in a square basin on the northern hemisphere. The figures are made by Dijkstra (2008) (left) and by the author (right), respectively. The figures show much resemblances. Most notably, both graphs show the double gyre structure in the interior of clockwise rotation in the north and anticlockwise rotation in the south, the wide band of southward (northward) flow at the west in the clockwise (anticlockwise) gyre and narrow northward (southward) return flow at the east in the Stommel boundary layer at the west for the northern (southern) gyre. The sign difference between the transport in the gyres in the model is due to the symmetry of the wind stress, which results in negative wind curl above the southern gyre and positive wind curl above the northern gyre. The sign difference in wind curl above the ocean basin is also found to be the cause for the double gyre structure in the real southern Indian Ocean (Aguigar-González *et al.*, 2016 and references within). The model formulation used to produce the figures in this report is thus at least able to reproduce the basic properties of the large-scale ocean circulation as is described in literature.

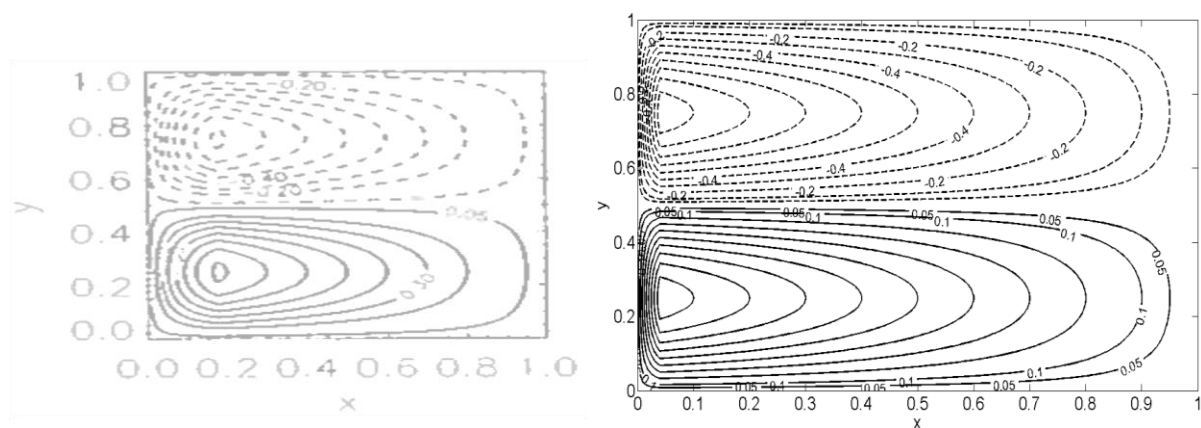


Figure 30 (left panel) Figure 6.4b of Dijkstra (2008), showing the non-dimensional streamfunction as a function of longitude x and latitude y for the conditions and solutions described in Section 2.1 (Sverdrup interior flow) and Section 2.1.2 (Stommel boundary layer). Dotted lines represent negative values, solid lines positive values. (right panel) Attempt to replicate the Sverdrup/Stommel solutions shown in the left panel. Definitions of the lines are the same as for the left panel. Since these graphs represent flow on the southern hemisphere, the values for y are positive.

The flow shown in Figure 30 could be thought of as being a representation of flow in the Indian Ocean without Madagascar, in which the flow would just exist of the Tropical Gyre and Subtropical Gyre. The bottom friction layer east of the ocean basin abruptly slows down the flow when the wind hits the coast, causing divergence of the water towards the north and the south, creating two gyres which are anti-symmetric around the line $y = 0.5$, which is also observed near Madagascar and the African western coast.

In this report, a strong emphasis has been put to investigating whether changes in the atmosphere-ocean dynamics could have caused changes in the Mozambique Channel throughflow and the Makassar Strait along-channel flow velocity. Up to now, only observations have been used to investigate whether this is the case. Although they are a simplified representation, analytical models can be used to investigate the role of specific processes in a physical system, such as the flow in an ocean basin.

Wind forcing on an ocean surface does not necessarily have to be equally strong over the entire ocean. In many cases, major wind forcing only acts on specific parts of the ocean surface. The question is whether the forcing on a specific part of the ocean could influence the entire ocean circulation. This could be investigated by the baroclinic Sverdrup model for flow around an island introduced in Section 2.1.4, where a tangent hyperbolic is used to turn off the wind at either the area west of an island or east of it.

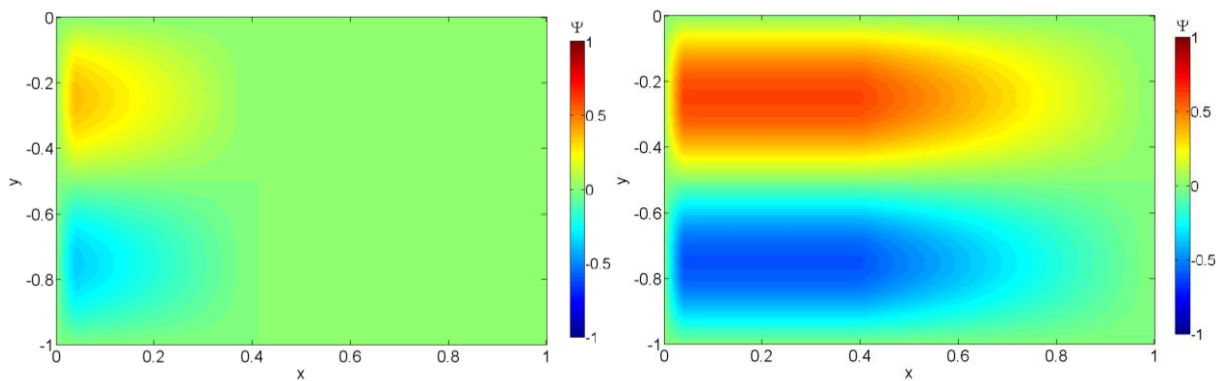


Figure 31 Non-dimensional streamfunction as a function of longitude x and latitude y for Sverdrup flow in a basin with a western Stommel boundary layer. Since these graphs represent flow on the southern hemisphere, the values for y are negative. The plots are made for an ocean where (left) wind only blows over the western half of a square ocean and (right) wind only blows over the eastern half of a square ocean. The wind stress, which is only a function of latitude, is minimum at the centre of the basin. In both panels, blueish colours represent negative values, reddish colours positive values and everything in between is between -1 and 1.

Figure 31 shows the flow in a square ocean basin in which the wind only blows everywhere at one side of the island. The figure clearly shows that if wind only blows over the western half of the basin, its effect is limited to that half. At the point where the wind reduces to zero, the flow also reduces to zero and a return flow occurs just close to the point of zero wind stress. On the other hand, if wind blows over the eastern half only, the entire ocean basin is influenced by that wind. The Sverdrup flow increases up to the point where the wind reduces to zero and continues as a zonally constant flow to the west until it reaches the Stommel boundary layer, where it speeds up again to form a return flow. Figure 32 shows a similar story, now for an ocean basin with the presence of an island. It shows that the use of a tangent hyperbolic to cut-

off the wind is less useful in the case wind only blows west of the island since its smoothed way of turning off the wind then gives a relatively large addition to the streamfunction value at the island calculated via the Island Rule.

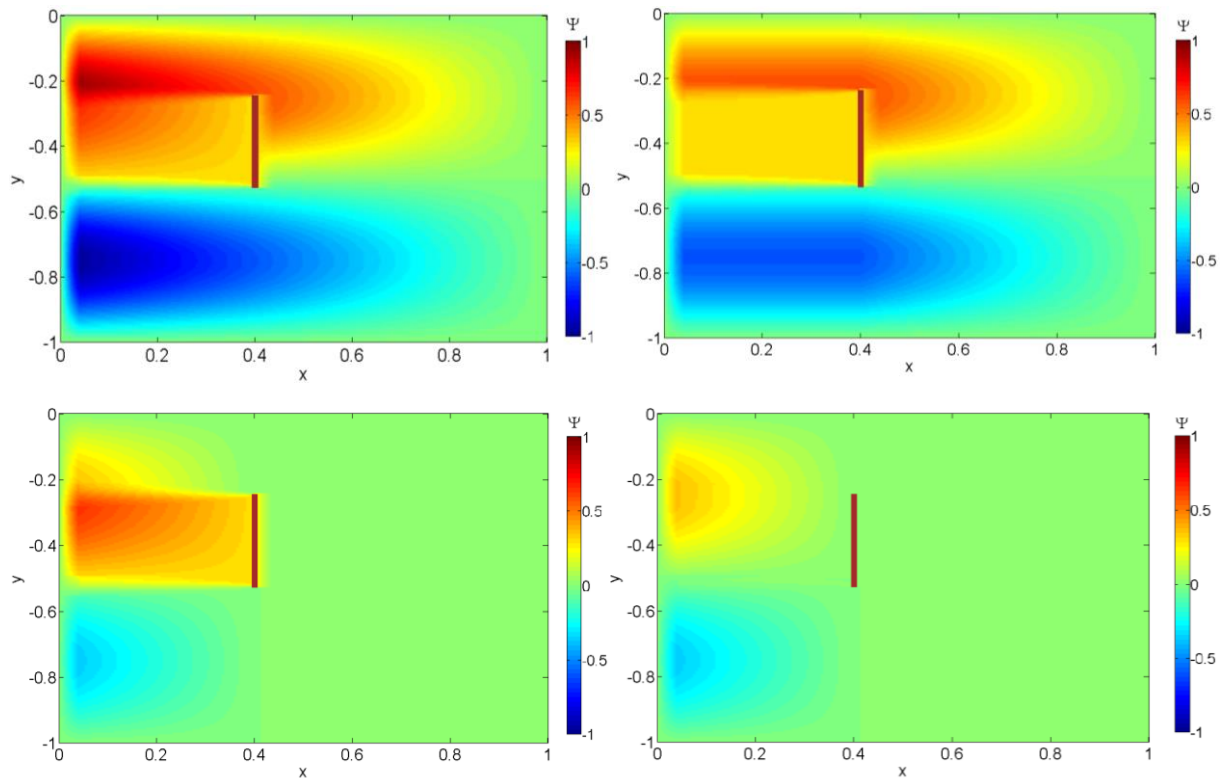


Figure 32 Non-dimensional streamfunction as a function of longitude x and latitude y for flow in an Indo-Pacific Ocean where the only island present is Madagascar. Since these graphs represent flow on the southern hemisphere, the values for y are negative. The island is represented by the brown bar; it is only 1 zonal grid thick, but a wider bar is shown for clearness). The flows shown are for (upper left) wind blowing over the entire Indian Ocean, (upper right) wind blowing only over the eastern half of the Indian Ocean, (lower left) wind blowing only over the western half of the Indian Ocean and (lower right) wind blowing only over the western half of the Indian Ocean that is corrected for the effects of gently sloping wind instead of an instantly truncated wind at $x = x_A$. In all panels, blueish colours represent negative values, reddish colours positive values and everything in between is between -1 and 1.

The most important point to take away from Figure 31 and Figure 32 is that, in case of laminar flow, a forcing over the eastern half of the basin gives a response by the flow of the full basin, while a forcing only over the western half of the basin does not influence the flow at the east. This is because of the beta effect: Rossby waves that are initiated by the vorticity balance between beta effect and wind can only travel westward and thus must be initiated east of the basin to induce full-ocean covering effects. The boundary layers, which are at first order governed by friction, only have a very local effect and do not significantly affect the open ocean flow.

The findings on the observed changes in the Indian Ocean trade winds are in agreement with above findings. As is shown in Figure 23, the trade winds first turn westward at the western half of the basin, and thus could only have influenced flow west of the basin, like the Mozambique Channel flow. Later, the eastern trade wind turn westward too, so the entire

southern Indian Ocean basin, and thus both transport through the MC and MS, could be influenced by the same wind pattern directly.

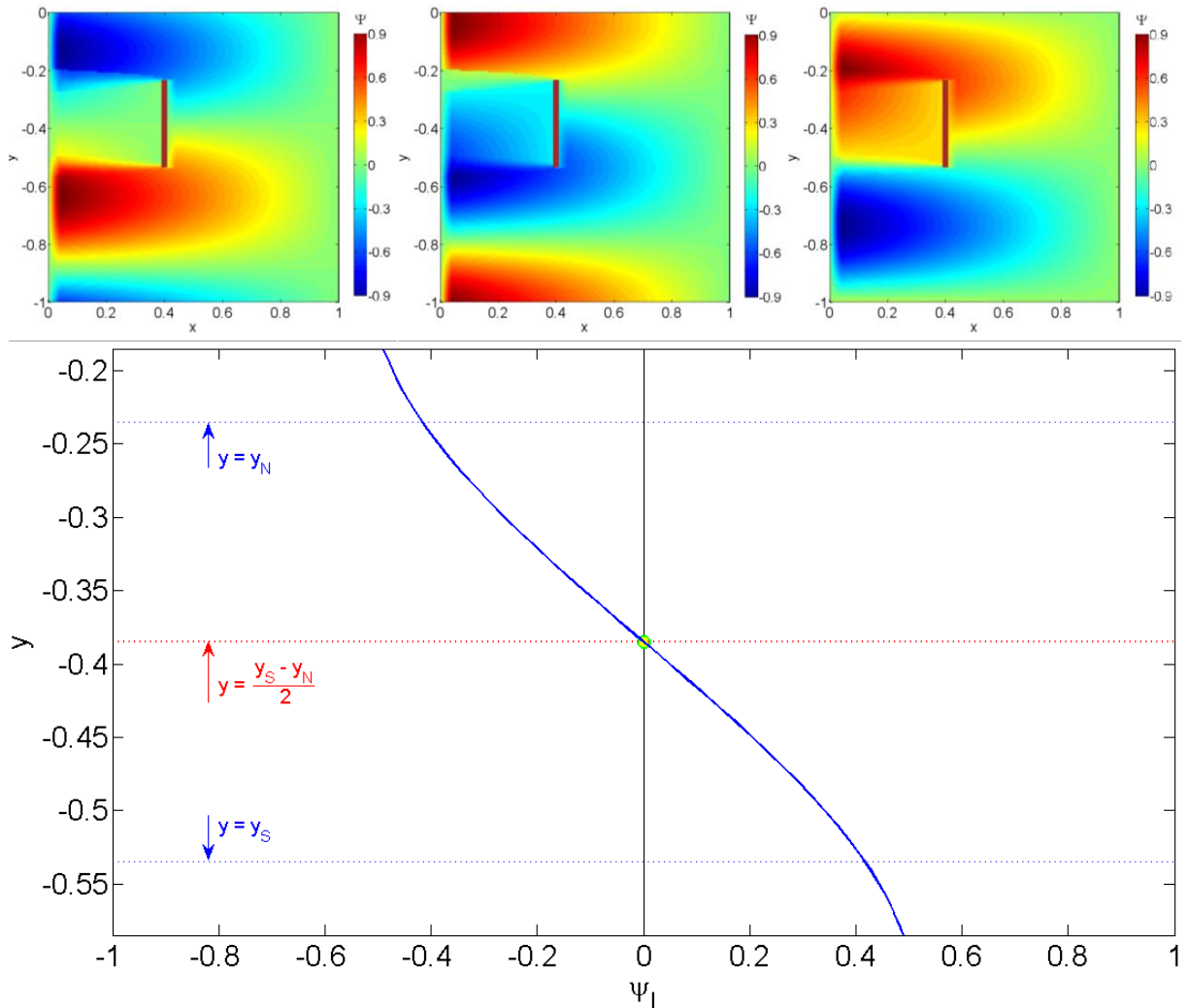


Figure 33 Upper panels: Non-dimensional streamfunction as a function of longitude x and latitude y for Sverdrup flow in a rectangular ocean basin with an island, which is 1 zonal grid thick, placed at $x = x_A$ and between $y = y_S$ and $y = y_N$. The wind stress curl is zero at (left panel) the middle of the island, (middle panel) the northern tip of the island and (right panel) the southern tip of the island, respectively. In all top panels, blueish colours represent negative values, reddish colours positive values and everything in between is between -1 and 1. Note that these plots are valid for the southern hemisphere (negative meridional values). (bottom panel) The wind induced transport around the island (Ψ_I) as a function of latitude of zero wind curl (y). Indicated are the meridians of the island's northern tip (y_N) and southern tip (y_S) in dotted blue lines and the meridian of the island's central latitude ($\frac{y_N - y_S}{2}$) by a red dotted line and a green dot on the (Ψ_I, y) curve.

Figure 33 demonstrates the effect of the latitude of zero wind curl on the flow west of an island. It shows that the more north the latitude of zero wind curl lies, the more wind-induced southward transport will be created west of Madagascar and vice versa. Figure 33 actually demonstrates that changes in the position of the boundary between the ocean gyres, for example

due to changes in the latitude of zero wind curl, could be responsible for the transition in the Mozambique Channel transport.

The shift of the two wind-induced gyres in Figure 33 may be retrieved partly from in situ observations. The Tropical Gyre and the South Equatorial Current, the latter being located at the boundary between the two gyres, are both found to shift northward. The Subtropical Gyre does, however, not shift northward. Also the possibility of the Tropical Gyre crossing the Equator instead of only having its southern boundary shifting to the north or the south is not meeting observations. These two mismatches are the reason for the annotation ‘partly’ when noting that the model and the observations agree.

5. Conclusions

In 2006, the Mozambique Channel throughflow has been observed to change. It changed from having a large temporal variability and small annual southward mean into a trend with small temporal variability and large southward mean. About two months later, the southward Indonesian Throughflow is also found to increase. Another increase of the southward Makassar Strait throughflow is found to occur in the beginning of 2008.

In this report, for different wind forcing profiles, model research has been performed on transports around an island due to wind-driven gyre circulation systems. Furthermore, observations with respect to the Indian Ocean sea surface temperature, Indian Ocean and Pacific Ocean surface winds, sea surface currents and gyre movement on basin scales have been analysed. Based on these, several findings have been done that can be combined into a mechanism which can be linked to the increased transport through the Mozambique Channel and the possible teleconnection with the increased southward transport through Makassar Strait. A teleconnection is a mechanism that is able to transport signals to distant sites, as are the MC and the MS.

This physical mechanism is summarized in Figure 34. Around May 2006, the west to east temperature gradient of the Indian Ocean Dipole became positive. Via Bjerknes feedback, the Indian Ocean trade winds turned westward which strengthened the east to west temperature gradient in the Indian Ocean. Likely, the Indian Ocean adapted to this new state by the initiation of upwelling equatorial Kelvin waves. Once reaching the Makassar Strait, these waves changed the tilt of the sea surface and the thermocline. These changed slopes are the likely cause of the observed increase of the southward along channel flow velocity in the strait near July 2006.

At a later time, around May 2007, the Pacific Ocean turned into a La Nina state and stayed like that for about two years. The consequence was, too via Bjerknes feedback, that the Pacific trade winds became more westward. The Pacific Ocean adapted to that by lifting the south to north difference in sea level even more. This is a likely cause for the second transition observed in the Makassar Strait along channel flow velocity to a more southward one. The effects of the change in IOD and ENSO added up in 2008.

After two years, the state of the oceans seems to turn back to one with more fluctuations between negative and positive temperature indices, explaining the observed slow evolution of

the along channel Makassar Strait flow velocity anomaly to positive values again after the first half of 2009.

For the Mozambique Channel, the changes in the transport observed in 2006 are most likely linked to a northward shift of the South Equatorial Current and a weakening of the Tropical Gyre. The former is likely linked to the observed simultaneous northward shift of the Tropical Gyre. The latter is based on the observation of weakened zonal equatorial sea surface currents prior to the observed throughflow increase. As the SEC is shifting northward, less of it flanks the eastern coast of Madagascar and a larger part of the SEC reaching Madagascar can tip its northern tip. By this, more ITF transported by the SEC can tip around northern Madagascar into the Mozambique Channel. The Mozambique Channel throughflow thus seems to have increased due to a combination of changes in the wind-driven gyre structure of the southern Indian Ocean both at the Equator and at the subtropical regions.

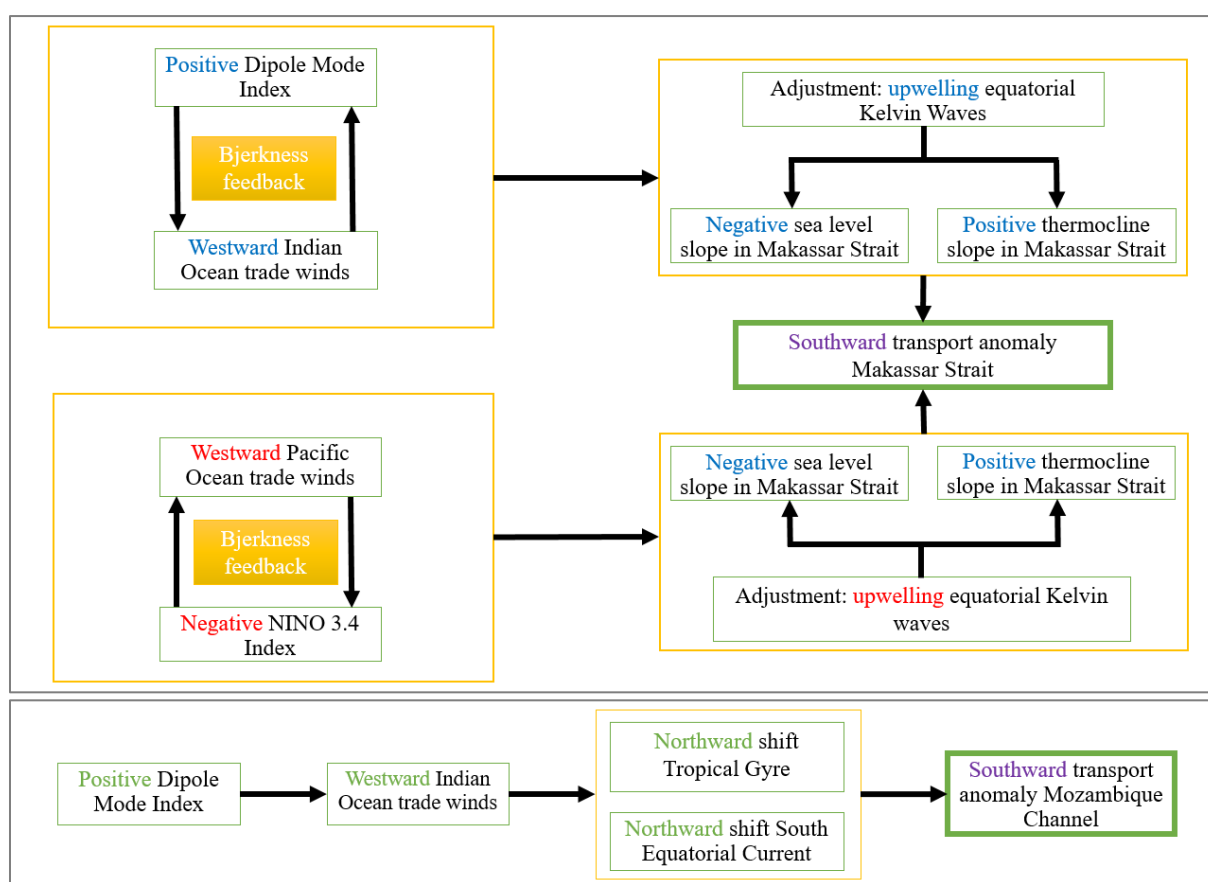


Figure 34 Schematic representation of the processes that likely have caused transport transitions observed in the Mozambique Channel and Makassar Strait. A positive DMI leads to westward equatorial winds in the Indian Ocean. These winds cause the ocean to adjust via upwelling Equatorial Kelvin waves. These Kelvin waves cause differences in the sea level anomalies at the Indian archipelago and in the MS, and thus a negative north to south difference between the northern edge of the MS and the waterways of the ITF into the Indian Ocean and between the location of the MS moorings and a little to the south of that. Changes in the NINO 3.4 index also lead to westward winds and adjustment via upwelling equatorial Kelvin waves, now at the Pacific Ocean, which also leads to negative north to south differences in η at the indicated sites. Both induced differences in η lead to more southward transport in the Makassar Strait. At the Mozambique Channel, the change to a positive DMI seems to lead to a northward shift of the latitude of zero wind curl. This leads to a northward shift of the Tropical Gyre and the South Equatorial Current. These two shifts lead to increased southward transport in the Mozambique Channel.

The change in sea level state within and around the Makassar Strait and the northward shifts of the Tropical Gyre and the South Equatorial Current are thought to have led to the MS transport and the MC transport transitions, respectively. These processes seem to have a shared origin. This origin, which is thus a teleconnection between the Mozambique Channel transport and the Makassar Strait throughflow, is the Bjerknes feedback between the changes in the in southern Indian Ocean surface temperature gradient and the changes in the southern Indian Ocean surface zonal winds.

The ITF and Mozambique Channel transport are, however, not entirely driven by the same mechanism. The MS transport is not only driven by processes within the Indian Ocean, but also by those on the Pacific Ocean. The transport through the Mozambique Channel can not only be influenced by processes within the Indian Ocean, but also by processes within the Atlantic Ocean and over the South-African continent (not investigated here). That the transports through the channel and the strait are not only driven by the same processes could be recognized in the evolution of the transport signals of the two waterways after 2006. The Mozambique Channel transport keeps having an increased mean southward transport, whereas the Indonesian Throughflow seems to evolve to a signal with a mean southward transport similar to that of the Makassar Strait transport before 2006. The transports through the two waterways can thus be driven partially by one or more teleconnections and partially by one or more local processes.

6. Discussion

6.1 Island Rule and wind stress observations

Back in section 2.1.4, the Island Rule had been introduced. Up till now, it has only been applied in this report in the model studies. The Island Rule implies that a change in the level of zero wind stress curl might lead to a change in the meridional transport through the Mozambique Channel.

In Appendix C, an in depth description of the water circulation through the Mozambique Channel as derived via the Island Rule is given. The time evolution of the latitude of zero wind stress curl (θ_0) east of Madagascar (averaged between 48°E-68°E) and that of the Island Rule transport are shown in the top panel and bottom panel of Figure 35, respectively. The Island Rule transport is applied over several regions of the southern Indian Ocean, in order to be check what effects the Ninety East Ridge and the coasts of Madagascar and the mainland east of Madagascar have on the wind induced recirculation through the Mozambique Channel.

Figure 35 shows a rapid decline in θ_0 after May 2006 and although the signal seems to evolve back towards its previous trend, the strong southward shift holds at least up to 2010. This would suggest that a wind-induced transport change would occur in the Mozambique Channel which can be found back in the values derived via the Island Rule.

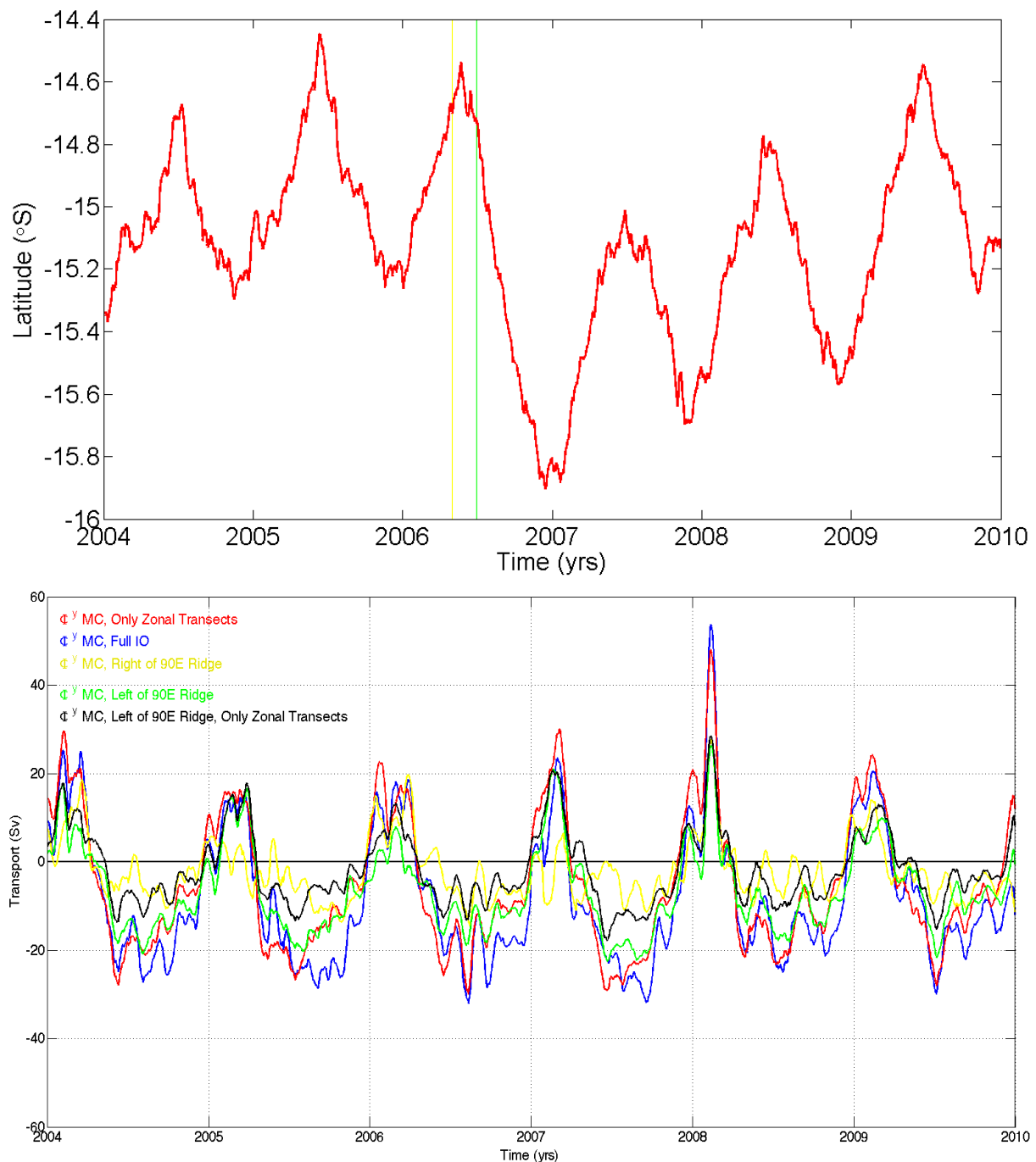


Figure 35 (top panel) Latitude of zero wind curl averaged between [52.5°E, 60°E] as a function of time in years. The values are filtered by a 210 day running mean. The yellow line indicates the approximate time at which the Mozambique Channel transport starts to transit and the green line when the Makassar Strait transport starts to transit. (right panel) Meridional transport in Sverdrup as a function of time in years through the Mozambique Channel as calculated via the Island Rule. The curves represent the transport following from the Island Rule if applied over the entire ocean east of Madagascar (blue), only up to the Ninety East Ridge (green), only east of that ridge (yellow), only over the zonal transects between Madagascar and the Ninety East Ridge (black) and only over the zonal transects up to the eastern boundary of the southern Indian Ocean (red). Wind stress values smaller than -10 Pa and larger than 10 Pa are excluded from the calculations. To leave out small-scale oscillations, the wind stress has been filtered by a 30 days running mean before the Island Rule was applied. A further in depth description on the derivation of these graphs is given in Appendix C.

The right panel of Figure 35 shows the Island Rule transport derived for several paths through the southern Indian Ocean. The graphs show that the effects of the coast on the recirculation through the Mozambique Channel is minor, whereas that due to the wind both east and west of the Ninety East Ridge is significant. Although the order of magnitude of the transport derived via the Island Rule matches that of the observed transport through the Mozambique Channel, it does not represent much of the further characteristics of the Mozambique Channel transport. In the light of the aims of this report, the most notable mismatch between Island Rule transport and observed transport through the MC is that the Island Rule does not and the observed transport does show a transition towards less variability and a more negative mean value.

It might seem contradictory that the latitude of zero wind curl does shift but the mean behaviour of the wind induced circulation around Madagascar does not. This is however not necessarily the case. Figure 35 and Figure 36 have shown a shift of the latitude of zero wind, but only between 48°E and 68°E within the latitudinal region of Madagascar. This is also the area at which the Subtropical Gyre is located. The finding the latitude of zero wind curl in this area does shift and the wind induced circulation does not change indicates that the area of the Subtropical Gyre is a lee: an area of which the flow is isolated of the rest of the domain. It could also explain why the Tropical Gyre and the SEC are found to shift northward at the time that the transport through the Mozambique Channel and Makassar Strait are changing whereas the Subtropical Gyre is not shifting northwards. As far as known by the author, this finding has not yet been found in earlier researches and could be a topic of future research.

It has thus been found that the wind driven dynamics in the subtropics do not change in the period of changing transports through the MC and MS, while the wind driven dynamics of the tropical region do change in that same period. Earlier (see Figure 26), it had already been observed that the zonal winds at the Equator show stronger westward anomalies in 2007 with respect to 2005 than the subtropical zonal winds do. These findings strongly indicate that the changes in the MC transport and MS throughflow are caused by equatorial dynamics rather than by locally changing wind forcing.

6.2 Timespan of LOCO and INSTANT

The conclusion that MC transport and ITF are subject to a teleconnection by the feedback between sea surface wind and sea surface temperature is supported by both model results and observations. Despite that, it must be remembered that the period covered by the transport data for both the Mozambique Channel and Makassar Strait only covers at max 8 years (respectively, November 2003-December 2009 and January 2004-July 2011, respectively). This is a rather short period to judge on signal changes on an inter-annual scale. The models and the data analysis techniques used in this report are also rather simple. These two facts make our conclusion a little suggestive if taken as a quantitative one, so it is better to take it as a qualitative one instead.

For now, we are not able to make a well-supported quantitative analysis on the processes in the Indian Ocean and Pacific Ocean in relation to the throughflows through the Makassar Strait and the Mozambique Channel. We will only be able to make qualitatively conclusions, both on

volume transport and on the interoceanic transport of climate signals between the world's oceans, if data gathering will be continued, such that the continuous time period covered by in situ observations will become sufficiently long.

Appendix

A. Derivation of the free boundary layer solutions

An important effect of an island on the ocean flow is the introduction of two diffusive flow layers, one at the west of each tip of the island. These layers form the transition between the two Sverdrup flow regions surrounding the island. For the northern tip, for example, the solution for the diffusive layer must ensure that at the upper boundary the streamfunction is equal to $\psi_{sv,1}$ and at the lower boundary that it is equal to $\psi_{sv,2}$.

To derive the equation governing the streamfunction in the diffusive layers, we can use the same methods as those used to derive the Stommel boundary layer solution. Here, the steps made by Dijkstra (2008), section 6.2 and further are followed.

The starting point is the barotropic vorticity equation (Equation (3)) with a flat bottom, constant positions of the zonal basin boundaries and a non-deformable atmosphere-ocean interface:

$$\frac{1}{\beta} \left(\frac{\partial \psi}{\partial x} \frac{\partial}{\partial y} - \frac{\partial \psi}{\partial y} \frac{\partial}{\partial x} \right) (\nabla^2 \psi - F\psi + \eta_b) + \frac{\partial \psi}{\partial x} = \vec{\nabla} \cdot (\vec{T} \times \hat{e}_3) - \frac{r}{2\beta} \nabla^2 \psi - \frac{1}{Re\beta} \nabla^4 \psi \quad (A1)$$

We now assume that lateral friction and inertia are negligible compared to bottom friction concerning vorticity input: the maximum length scale on which inertia and lateral friction are important is much smaller than that on which bottom friction is important. This reduces the barotropic vorticity equation to:

$$\frac{\delta_S}{L} \nabla^2 \psi = -\psi_x + \vec{\nabla} \cdot (\vec{T} \wedge \hat{e}_3) \quad (A2)$$

The free boundary layer exists along a line of constant longitude instead of constant latitude, along which the already analysed Stommel boundary layers exists. Therefore, we will now stretch the meridional coordinate instead of the zonal coordinate near the boundary layer. The stretched zonal boundary layer coordinate at the northern tip of the island is given by ($\delta_* = \delta L$):

$$\zeta = \frac{y-y_n}{\delta} \Leftrightarrow \frac{\partial}{\partial y} = \frac{1}{\delta} \frac{\partial}{\partial \zeta} \quad (A3)$$

Similarly, the island's southern tip's stretched zonal boundary layer coordinate is given by:

$$\zeta = \frac{y-y_s}{\delta} \Leftrightarrow \frac{\partial}{\partial y} = \frac{1}{\delta} \frac{\partial}{\partial \zeta} \quad (A4)$$

Using that $\vec{T} = \tau^x \hat{e}_1$, we can use that $\vec{\nabla} \cdot (\vec{T} \wedge \hat{e}_3) = -\frac{\partial}{\partial y} \tau^x = -\frac{1}{\delta} \frac{\partial}{\partial \zeta} \tau^x$. This allows us to write the above equation as ($\frac{1}{L} = \frac{\delta}{\delta_*}$):

$$\frac{\delta_S}{\delta_*} \left(\delta \psi_{xx} + \frac{1}{\delta} \psi_{\zeta\zeta} \right) = -\psi_x - \frac{1}{\delta} \frac{\partial}{\partial \zeta} \tau^x \quad (A5)$$

We now put $\delta_S = \delta_*$ and multiply both sides with δ to get:

$$\delta^2 \psi_{xx} + \psi_{\zeta\zeta} = -\delta \psi_x - \frac{\partial}{\partial \zeta} \tau^x \quad (\text{A6})$$

The next step is to make an inner expansion of our simplified barotropic vorticity equation. The expansion of the streamfunction is given by:

$$\hat{\psi}(y, \delta) = \hat{\psi}^0(y) + \delta \hat{\psi}^1(y) + \mathcal{O}(2) \quad (\text{A7})$$

Performing the inner expansion to our simplified barotropic vorticity equation results in the following equation, which is of second order precision:

$$\delta^2 (\hat{\psi}_{xx}^0 + \delta \hat{\psi}_{xx}^1) + (\hat{\psi}_{\zeta\zeta}^0 + \delta \hat{\psi}_{\zeta\zeta}^1) = -\delta (\hat{\psi}_x^0 + \delta \hat{\psi}_x^1) - \frac{\partial}{\partial \zeta} \tau^x \quad (\text{A8})$$

This provides the $\mathcal{O}(1)$ system, using that $\delta^3 \hat{\psi}_{xx}^1 \ll \delta \hat{\psi}_{\zeta\zeta}^1$:

$$\delta \hat{\psi}_x = -\hat{\psi}_{\zeta\zeta} \quad (\text{A9})$$

The boundary conditions for this equation are:

$$\hat{\psi}(x_A, y_s) = \psi_{sv,1}(x_A, y_n) \quad (\text{A10})$$

$$\lim_{\zeta \rightarrow \infty} \{\hat{\psi}(x, \zeta)\} = \lim_{y \downarrow y_1} \{\psi_{sv,1}(x, y)\} \quad (\text{A11})$$

$$\lim_{\zeta \rightarrow -\infty} \{\hat{\psi}(x, \zeta)\} = \lim_{y \uparrow y_2} \{\psi_{sv,2}(x, y)\} \quad (\text{A12})$$

Where y_1 and y_2 are the upper and lower boundaries of the diffusive layer at the northern tip of the island, respectively. At the west, at $x = \ell$, the layer transits into the Stommel boundary layer for the western coast. For the southern tip's diffusive layer, the boundary conditions are:

$$\hat{\psi}(x_A, y_s) = \psi_{sv,1}(x_A, y_s) \quad (\text{A13})$$

$$\lim_{\zeta \rightarrow \infty} \{\hat{\psi}(x, \zeta)\} = \lim_{y \downarrow y_1} \{\psi_{sv,2}(x, y)\} \quad (\text{A14})$$

$$\lim_{\zeta \rightarrow -\infty} \{\hat{\psi}(x, \zeta)\} = \lim_{y \uparrow y_2} \{\psi_{sv,1}(x, y)\} \quad (\text{A15})$$

Finding the solution of this heat equation is an elementary mathematical problem, which has already been derived long ago (e.g., Carslaw and Jaeger, 1959). The solution is the sum of two complementary error functions whose arguments are the same in magnitude but opposite in sign. The factor with which the arguments are multiplied depends on x and y such that the boundary conditions for the limiting case are met. The solution is:

$$\hat{\psi} = \frac{\left(\lim_{y \downarrow y_1} \psi_{sv,1}\right)}{2} \operatorname{erfc}\left(-\frac{y-y_0}{2\sqrt{\delta(x_A-x)}}\right) + \frac{\left(\lim_{y \uparrow y_2} \psi_{sv,2}\right)}{2} \operatorname{erfc}\left(\frac{y-y_0}{2\sqrt{\delta(x_A-x)}}\right) \quad (\text{A16})$$

The parameterizations of the upper and lower boundaries for the island's northern tip are:

$$y_1 = y_n + 2\sqrt{\delta(x_A - x)} \quad (\text{A17})$$

$$y_2 = y_n - 2\sqrt{\delta(x_A - x)} \quad (\text{A18})$$

For the southern tip, the solutions are:

$$\hat{\psi} = \frac{\left(\lim_{y \downarrow y_1} \psi_{sv,2}\right)}{2} \operatorname{erfc}\left(-\frac{y-y_0}{2\sqrt{\delta(x_A-x)}}\right) + \frac{\left(\lim_{y \uparrow y_2} \psi_{sv,1}\right)}{2} \operatorname{erfc}\left(\frac{y-y_0}{2\sqrt{\delta(x_A-x)}}\right) \quad (\text{A19})$$

$$y_1 = y_s + 2\sqrt{\delta(x_A - x)} \quad (\text{A20})$$

$$y_2 = y_s - 2\sqrt{\delta(x_A - x)} \quad (\text{A21})$$

From a mathematical point of view, it would be desired that the value of δ would reach zero, since then the layer thickness would be infinitely thin. The free boundary layer actually only serves as a tool to smoothen the transition between the two Sverdrup solution regimes, in a similar way as the Stommel boundary layer near a coast does. However, a constraint is put to the value of δ by the physics: the relative dependence of bottom friction to the beta effect in the input of vorticity determines the value of δ . It is given by the same equation as that for ℓ . However, since we are looking at a different situation, it has been chosen to put δ to a slightly lower value than ℓ . Assuming that bottom friction (water sliding along water) for the diffusive layer is slightly weaker than for the coastal Stommel boundary layers (water sliding along solid land), the thickness of the layer has been put equal to:

$$\delta = \frac{\ell}{5} \quad (\text{A22})$$

B. Madden-Julian Oscillation and equatorial Kelvin wave dynamics

The Madden-Julian Oscillation (MJO) is a dominant mode in the tropical atmosphere, with a temporal period ranging between 30 days and 90 days, first recognized by Madden and Julian (1971). It exists of a convection cell, whose strength oscillates with the given time periodicity and that is bordered by easterlies to the east and westerlies to the west. The MJO, travelling with a velocity of the order of 5 m/s, crosses all of the world oceans, but is found strongest over the Indian Ocean and the Pacific Ocean. The MJO is driven by many variables, like convection and wind velocity, but also feeds back on many of these same variables (Zhang, 2005; Wilson et al., 2013). Due to its interaction with convection and wind over the oceans, the Madden-Julian Oscillation is often connected to the imitation processes of Kelvin waves at the Equator and the coast near the Equator (Webber *et al.*, 2010; Yan *et al.*, 2012). Weaker MJO periods are linked to weaker equatorial Kelvin waves.

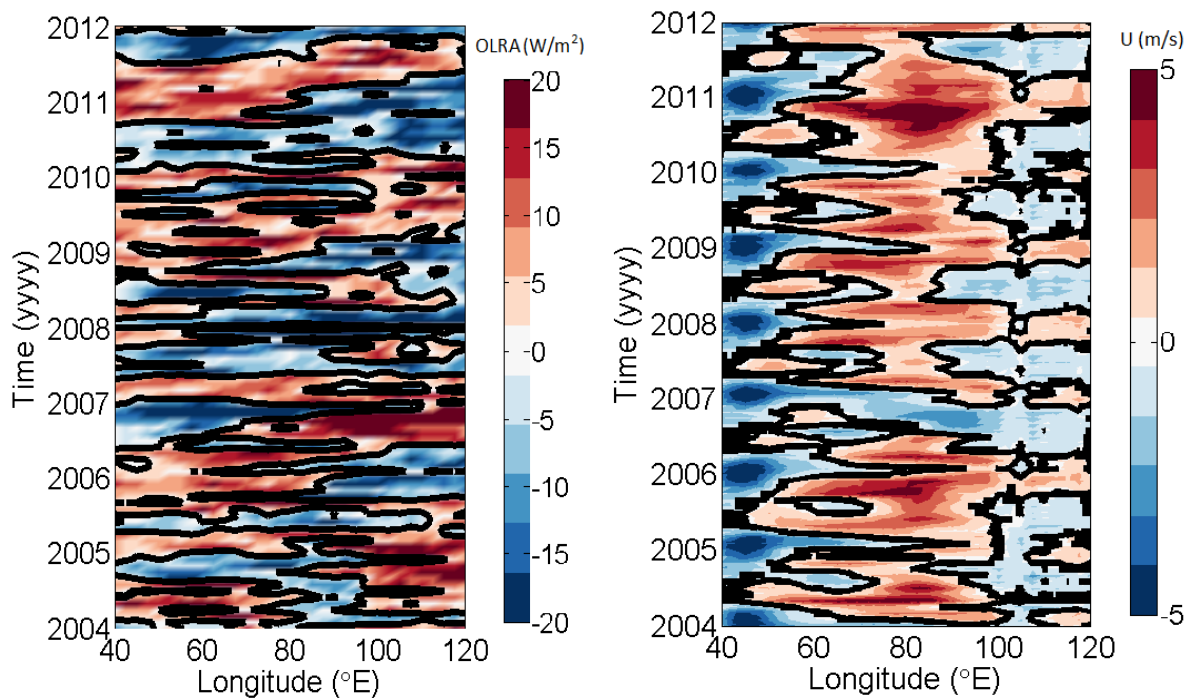


Figure B1 (left panel) Time in years versus longitude Hovmoller diagram of monthly mean outgoing longwave radiation anomalies (OLRA) in W/m^2 averaged between 5.5°N and 5.5°S . For each month of the year, the anomalies are calculated with respect to the 1983-2010 mean outgoing longwave radiation of the accompanying month. (right panel) Time in years versus longitude Hovmoller diagram of the monthly mean zonal wind averaged between 2.5°N and 2.5°S .

The strength of the MJO is depending on the strength of convection in the cell and the wind at its flanks. The convection can be represented by the strength of the outgoing longwave radiation (OLR). This can representation is valid since the more OLR can be observed, the less clouds are present and thus the less upward convection is occurring, meaning a weaker MJO convection cell.

Figure B1 shows the monthly OLR anomaly with respect to the 1981-2010 mean monthly outgoing longwave radiation and the monthly zonal wind velocity, both along the Equator. The left panel of Figure B1 is derived by combining the outgoing longwave radiation data of the *olr.mon.ltm.nc* dataset and the long-term mean outgoing longwave radiation data from the *olr.mon.mean.nc* dataset, which have both been downloaded from Earth System Research Laboratory (ESRL) [website](#). The datasets both contain data at a 2.5 degrees resolution in both horizontal directions. The right panel of Figure B1 is derived zonal wind data from the ERA-Interim [website](#), also at monthly temporal resolution and with a 2.5 degrees horizontal resolution. The figures show a negative OLR anomaly between mid-2006 to early to mid-2008 travelling along the Equator and westward winds mid-2006 to 2007. These observations are indicative for a weakened MJO.

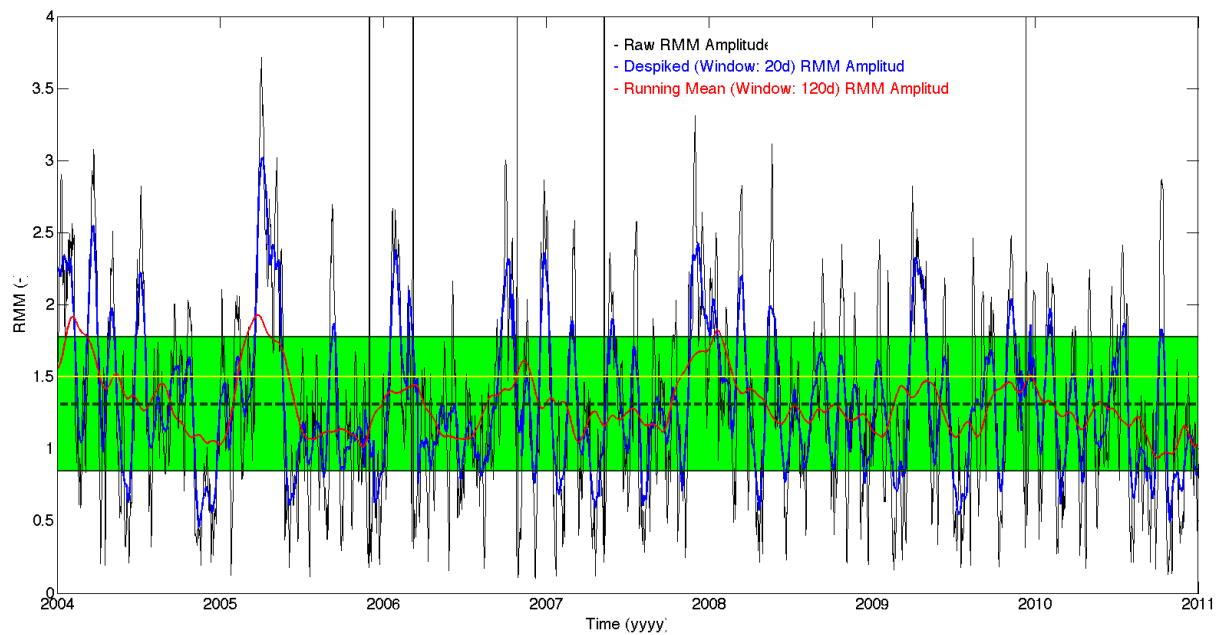


Figure B2 Madden Julian Oscillation index as a function of time in years derived according to Wheeler and Hendon (2004). Black indicates the original data, blue the data filtered via a running median and red the running mean of the running median filtered MJO index. The green band indicates the mean value (dark green dotted line) plus and minus the standard deviation of the raw data. Values below the yellow line (index equal to 1.5) are considered weak.

In the time since their discovery, scientists have created indices representing the strength of the MJO. Some of these are based on the method of Principle Component Analysis (PCA). One of the indices based on PCA is the Wheeler and Hendon (2004) (WH2004) index. If the magnitude of this index is large, then the convection is strong and the MJO is also strong. This index, downloaded with a daily resolution from the Australian Government Bureau for Meteorology [website](#), is shown in Figure B2.

Another index, based on Extended Empirical Orthogonal Functions, is defined by the Climate Prediction Centre (Gottschalck *et al.*, undated (visited on 15 June, 2016); Xu *et al.*, 2002). Positive values indicate enhanced convection, negative values suppressed convection. The pentad index values, downloaded from the CPC [website](#), are plotted in Figure B3.

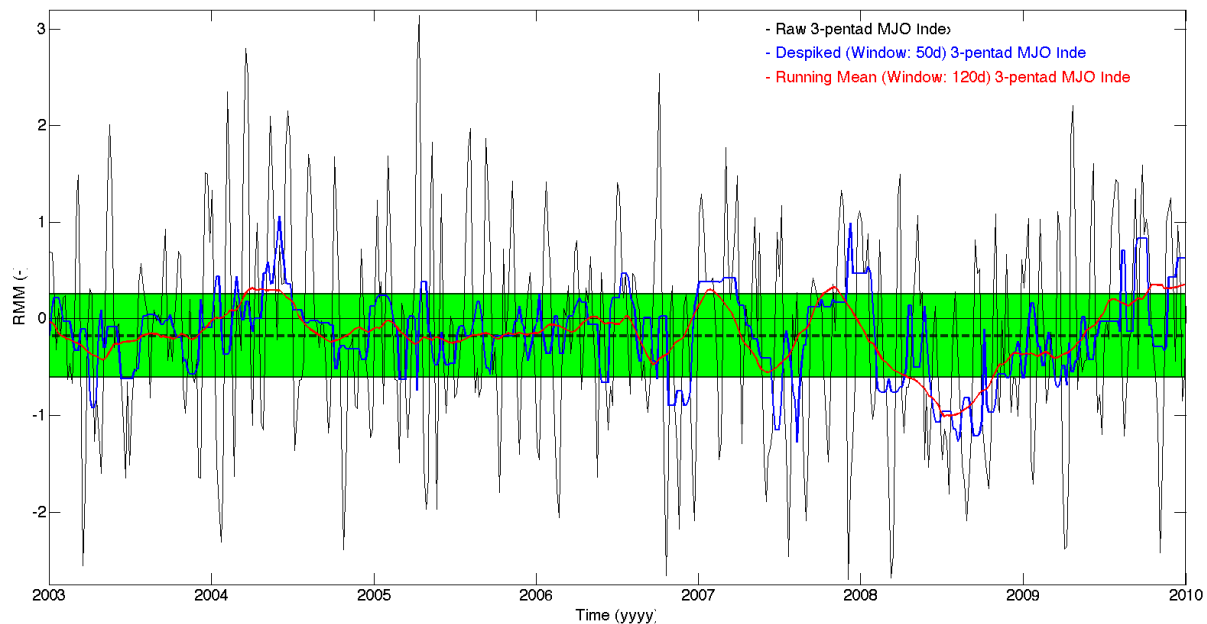


Figure B3 Madden Julian Oscillation index as a function of time in years derived by the Climate Prediction Centre. Black indicates the original data, blue the data filtered via a running median and red the running mean of the running median filtered MJO index. The green band indicates the mean value (dark green dotted line) plus and minus the standard deviation of the original data.

Figures B2 shows that in years with little Mozambique Channel/Makassar Strait transport (2003, 2004 and 2008), the WH2004 index shows large peaks, meaning that values are larger than the mean values plus one standard deviation. In years with increased transport, the opposite is observed. In 2006, the year of the transport transitions, this index does not even reach the mean value and in the two succeeding years it hardly gets above that value. This indicates very weak MJO activity.

The CPC MJO index in Figure B3 shows a similar pattern, but the pattern of this index is leading on WH2004 index by about a year. The CPC MJO index declines to values below zero in 2005 and stays like that for two years. These two years would thus be marked by weakened MJO activity.

The two indices seem to contradict in when the MJO starts to weaken: 2005 or 2006. They do however show that the MJO is weakened in 2006, which is the transition year of the Mozambique Channel throughflow and the Makassar Strait throughflow. Therefore, the indices seem to indicate that Kelvin waves initiated by MJO activity in 2006 are likely to be weaker than those in other years. Due to a more synchronous pattern, WH2004 index qualitatively seems to better match the transport patterns in the Mozambique Channel and Makassar Strait than the CPC MJO index does.

Appendix C: Island Rule applied to wind stress observations

In order to make a closer look to this rule useful, it must be so that the latitude of zero wind stress curl (θ_0) changes by the time the transports change. A graph showing the latitude of θ_0

as a function of time is made via daily Blended Sea Winds wind stress data with a 0.25° zonal and lateral resolution.

The wind stress data is part of the Blended Sea Wind dataset of the [National Centers for Environmental Information](#) (NCEI) (Zhang *et al.*, 2006a; Zhang *et al.*, 2006b; [NCEP website](#)). Wind stress components are calculated by scaling the NCEP Reanalysis 2 (NRA2) stress by the ratio of blended satellite wind speed of the NRA2 wind speed squared (for stress). Based on information from the NCEI [website](#) on the noisiness and extremely large outliers within the data, the wind stress is filtered first: absolute values larger than 10Pa, which leaves out less than 1% of the data, are removed.

Figure C1 shows long-term the latitude of zero wind stress curl as a function of longitude and time. The graph shows that θ_0 always lies very south at longitudes east of 70°E , with very small variations of this latitude in time. West of 45°E , the position is fluctuates a lot. Therefore, the zonal average θ_0 is further monitored for the longitudes 48°E - 68°E .

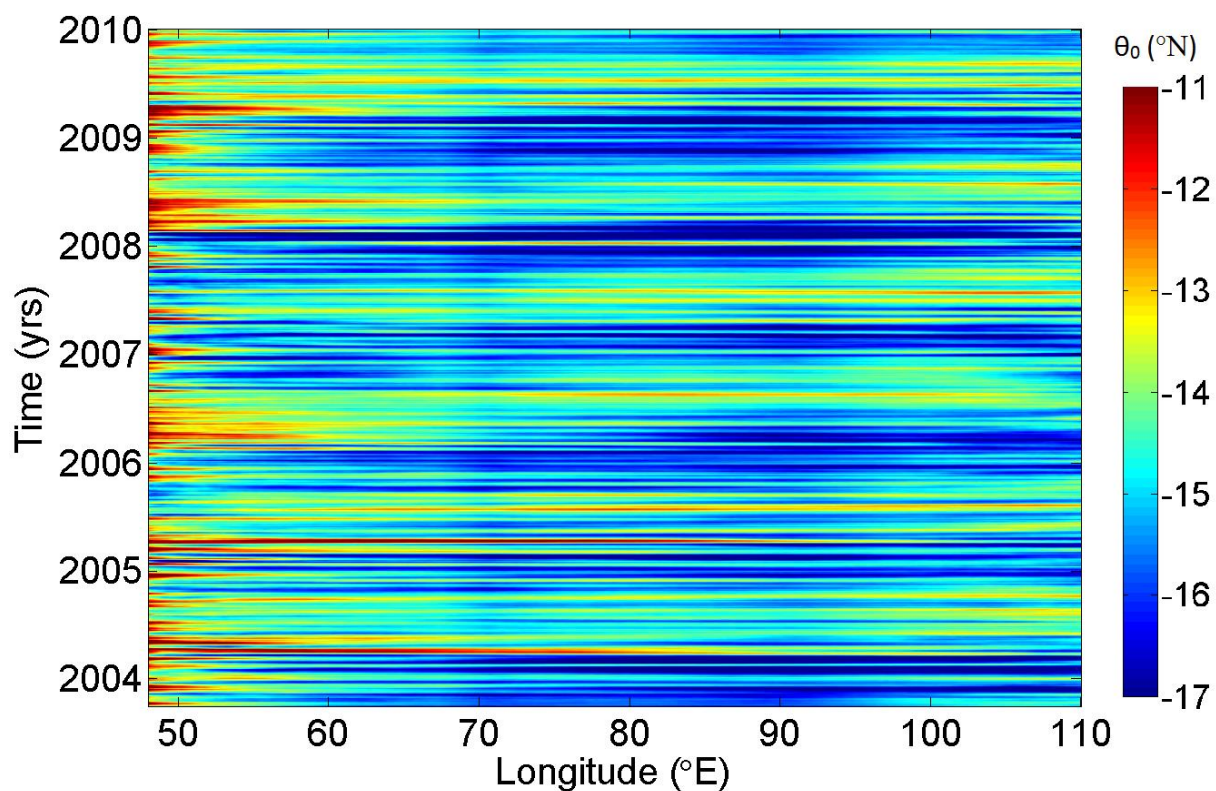


Figure C1 Longitude versus time Hovmoller diagram of the most northern latitude, in degrees north, where wind stress curl is zero (θ_0), as a function of time in years and longitude. Data whose magnitude is larger than 10Pa has been removed. The data has been filtered in time by a 210 day running mean.

Figure C2 shows the mean latitudinal position of the zero wind stress curl. The curve shows a rapid decline after May 2006 and although the signal seems to evolve back towards its previous trend, the strong southward shift holds at least up to 2010. It thus shows that the level of zero wind stress curl shifts to the south. This indicates the possibility that the wind induced

southward circulation around the island Madagascar will be decreased, which is an opposite observation to that expected based on the observed transport changes in the Mozambique Channel. It is thus worth the effort to look at the addition of the wind induced circulation around Madagascar to the total transport through the Mozambique Channel.

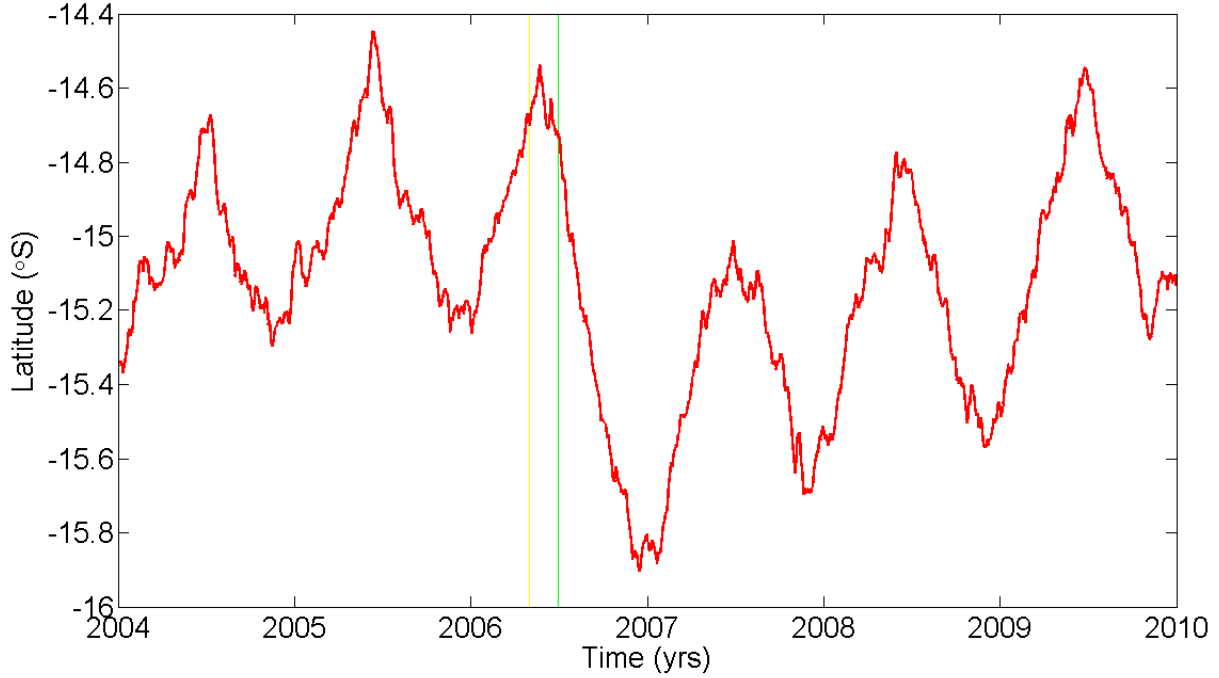


Figure C2 Latitude of zero wind curl averaged between [52.5°E, 60°E] as a function of time in years. The values are filtered by a 210 day running mean. The yellow line indicates the approximate time at which the Mozambique Channel transport starts to transit and the green line when the Makassar Strait transport starts to transit.

The dimensional form of the Island Rule presented in Section 2.1.3 is given by (Wajsowicz, (1992); the form presented by Godfrey (1989) gives transport along the eastern coast of an island, see Pedlosky *et al.* (1997)):

$$\psi_I = -\frac{1}{\rho_0(f_N - f_S)} \oint_{ABCD} \tau^{(l)} dl \quad (C1)$$

In Equation (C1), the terms f_N , f_S represent the Coriolis parameter at the latitude of the northern tip, θ_N and southern tip, θ_S of the island, respectively ($f_{N,S} = 2f_0 \sin(\theta_{N,S})$, see also Table 1).

The Island Rule is applied over five different trajectories, shown in Figure C3. The first one (indicated in blue) starts at the southern tip of Madagascar, follows the meridian of the island's southern tip up to the Australian coast, then follows the Australian coast up to the latitude of Madagascar's northern tip, runs back along the meridian of Madagascar's northern tip and loops back along Madagascar's western coast to the starting point. In two other cases, almost the same trajectory is followed. In one case, the curve is shorted at 90°E (green path) and in the other it starts and ends at 90°E (yellow path). This specific longitude is the line along which the Ninety East Ridge is located. This ridge could influence the transport around Madagascar since it forms

an obstacle for barotropic flow and baroclinic flows at depths greater than the tip of the ridge. The two loops can show in what extend it is of influence on the total flow. Another “loop” exists only of the two zonal transects (shown in red), to see in what extend the addition of the trajectories along the coast are of influence on the total MC transport. The last path (shown in black) exists only of the zonal lines west of 90°E to both exclude effects of the Ninety East Ridge and the coasts.

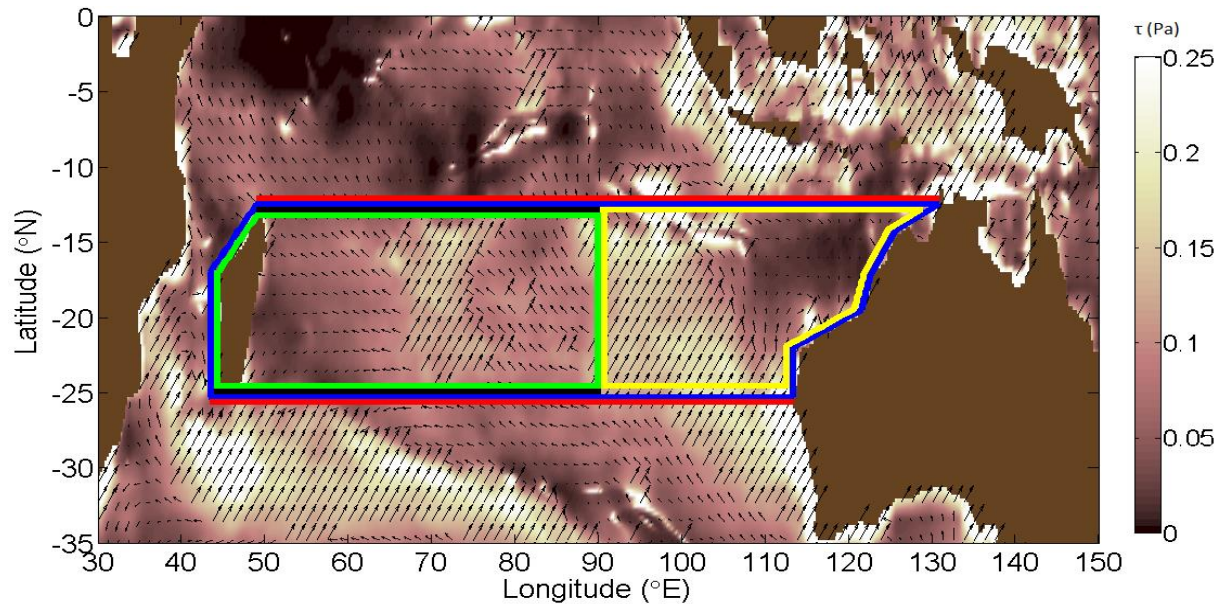


Figure C3 Longitude versus latitude map of the wind stress in Pa on March 31, 2006 (magnitude: given in colour; direction: given by the vectors, which scale with the magnitude of the wind stress). On the map the paths along which the Island Rule are applied is also shown. The Island Rule has been applied along five tracks. Three of them are closed curves: along the western coast of Madagascar towards the Australian mainland (blue), between Madagascar and the Ninety East Ridge (green) and between the Ninety East Ridge and the Australian mainland (yellow), respectively. For two of the paths, only the northern most and southern most zonal parts of the trajectories are taken into account. The first one extends between Madagascar and the Australian mainland (red), the second one between Madagascar and the Ninety East Ridge (black).

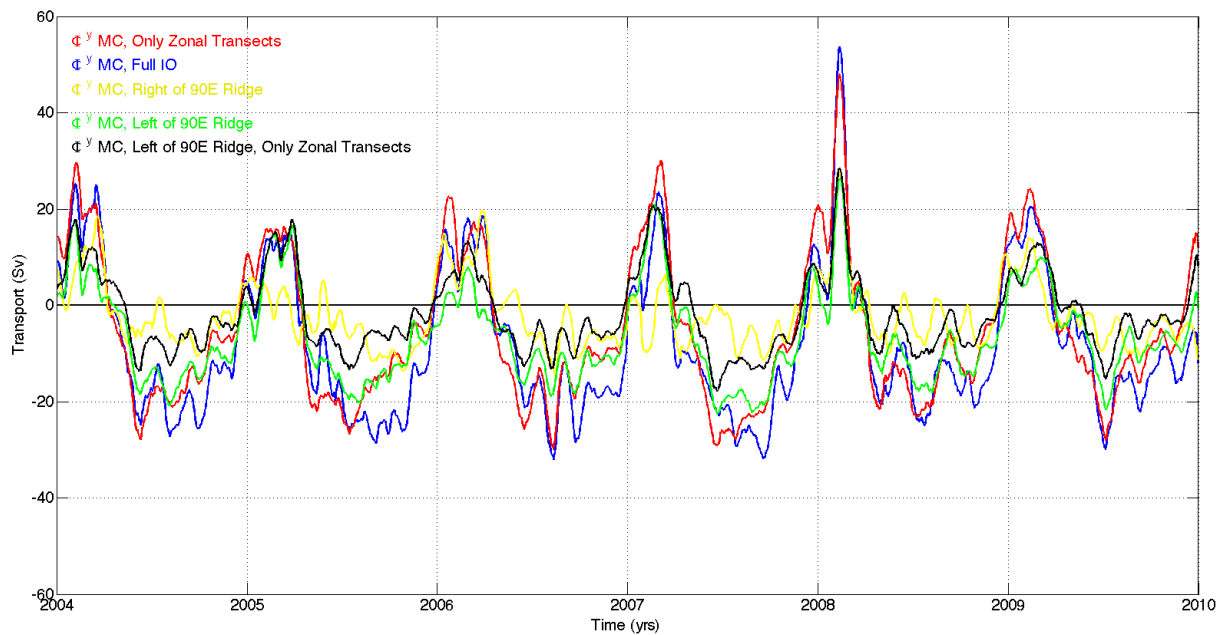


Figure C4 Meridional transport in Sverdrup as a function of time in years through the Mozambique Channel as calculated via the Island Rule, which is given in dimensional form by Equation (36), along the paths shown in Figure C3. Wind stress values smaller than -10 Pa and larger than 10 Pa are excluded from the calculations. To leave out small-scale oscillations, the wind stress has been filtered by a 30 days running mean before the Island Rule was applied.

Figure C4 shows the southward transport west of Madagascar as deduced from the Island Rule. As expected from the observed transport direction in the Mozambique Channel, the annual mean total Island Rule transport is southward. The figure indicates that the addition to the total Island Rule transport by the wind along the path following the island's and mainland's coast is generally smaller than that over the zonal transects. It also indicates that a larger portion of the transport is caused by winds west of the Ninety East Ridge than by the winds east of it, but still significant. The transport through the Mozambique Channel due to pressure differences between the tips of Madagascar represents the order of magnitude of observed transport well, but not its further characteristics.

Acknowledgements

For about two and a half years, IMAU has been like a home to me. It is an honour and a pleasure to be part of this institute. I enjoyed to experience its research activities and its scientific expansion, to meet students and academicians, to participate the half-monthly group meetings and randomly spread self-organized student meetings and to play at the badminton sessions and tournament. And of course, it was very special to be at the celebration of IMAU's 50th anniversary.

There are many people whom I owe many thanks. For having a project within the field of physical oceanographic research to graduate on at the first place, I am very thankful to my supervisor Will de Ruijter. Without his formulation of a thesis project, there would not have been a thesis within this field to work on at IMAU at all. Will certainly made a huge contribution in enabling me to successfully carry out this project, by combining his professionalism within

the research area with a high dose of humour and sobriety. I am happy to have had a supervisor with whom I was able to get both professionally and personally such a good bond.

The second person I wish to thank is Wim Ridderinkhof. Wim started as part-time supervisor at the time Will had gone abroad for a few weeks. Wim however kept on co-supervising me when Will returned and turned into my second fully incorporated supervisor. I am very thankful for his sharp and to the point advises and suggestions, which he always brought with a wink.

Thirdly, I wish to thank my secondary corrector Anna von der Heydt. As I did not have a daily supervisor, someone at IMAU had to volunteer for this job. Thanks for being that person, Anna!

As I only had meetings with Will and Wim once per two weeks, I had to “make clever use of the institute”, meaning that if I had questions I had to go visit the present IMAU people and see if someone could and wanted to help. Especially Michiel Baatsen, Lisa Hahn-Woernle, Fiona van der Burgt and Dewi le Bars have had spent a large piece of their time on me to keep me on track. I could also fall back on Christian Steger, Claudia Wieners and Jan Viebahn now and then for getting answers on several questions. Thank you all for answering my many questions and for your great support!

Special thanks are to Michael Kliphuis, who, at the beginning of my thesis time, learned me how to use several computer tools on the Mac PCs and to work with IMAU’s HOPF computer. After that, I was welcome if I had any general questions. Often, Paul Smeets got caught in the conversations. Thank you both for the sometimes hilarious but often also productive chitchats!

Talking about chitchats, I am granted many thanks to IMAU secretary Floor van Lee. Often it was about all day life subjects, but just as often the conversations had a clear goal concerning the planning and succession of the thesis. Thanks, Floor!

Where technique is used, issues are waiting to pop up. I owe IMAU’s technician team (Michel Bolder, Wim Boot, Mark Eijkelboom, Henk Snellen and especially Mac maintainer Marcel Portanger) for their support on all sorts of computer related issues that got by on my screen the past 9 months.

Also with the rest of IMAU’s staff, both from the Ocean, Coastal Dynamics, Ice and Climate, Atmospheric Chemistry and Atmospheric Dynamics, it has been very delightful to converse and interact. The colloquia, promotions and discussions on how IMAU works and grows have been a pleasure to me. Thanks for the wonderful time I had at the 6th floor of the BBG for the past two and a half years (seven years if including the Bachelor’s years at the BBL) during the lectures and tutorials, my time as Master student in IMAU’s scientific world and the social interactions in the coffee – and sometimes cake – room!

Of course, I had a large amount of buddies at Buys Ballot Laboratory room 6.01. The lunch walks, the student meetings in 6.47, the lunches in the coffee room, the gatherings at different sites in Utrecht and the corporation at the office – It’s just too much to make a complete list. Thank you, my generation of IMAU Student Room students: Brenda van Zalinghe, Tjebbe Hepkema, René van Westen, Stan Jakobs, Henri van den Pol, Yannos (Ioannis) Komis, Patrick Bunn, Truman Wright, Stef Boersen, Evelien Dekker, Klaas Lenstra, Anna Kruseman, Stijn Naus, Lennart van den Boogert, Thom Wolf and Selma de Leeuw. I am very granted to have

worked with a fantastic team in the Student Room. Each member has a very strong personality, a strong and social mind and the potential to turn what they see as their ideal prospects into reality.

Two students (currently) not studying at the UU that I am very thankful are Suzanne Thoen (Bachelor buddy) and Henk Jan Bragt (buddy since the primary school). Ever since I met them, they were very concerned with my study. They often talked with me about the progress and were of great support during my Master thesis time. And thanks that you were there during my presentation!

This entire work has been checked for typos and bad formulations by Lara van Zuilen just a few days before the deadline. I am very thankful she was willing to take his effort.

I also have had much support of advisors from IMAU and the beta sciences Bachelor's program. Especially noteworthy is the work performed by Joke van Dijk, Wim Westerveld, Geert-Jan, Aarnout van Delden and Roderik van de Wal. Their door was open if my progress tended to get halted and if necessary, something could always be arranged to keep my goals accessible. Thanks for your support concerning issues related to study and personal life.

I have had much help of people from many industries within the Utrecht University. Already since the beginning, I can count on people from the Julius Institute, security, reception, building maintenance and housekeeping to look after me. Thanks for feeling so concerned with my growth as a young scientist and me growing from being a just-18 boy to a young adult of 26.

Not to forget, the strongest army that is always at my side: my family. I thank my mom and dad, my sister Natasja and Rick Eekels for being there. Although they often had no clue on what my thesis was about – they were very honest about that – they have never let me down and supported me where they could. Thanks for the diner talks, the talks at the trips towards the UU, during shopping, while being at my grandparents – who I am of course also very thankful for all these years of support and interest – and just at any place and time we are together! I hope I can always count on your help. Without it, my world would just become one of science without a soul.

To conclude, I wish to thank obituary Michel van der Vorst, a great friend, support and coach.

References

Books

Conduction of Heat in Solids

H. S. Carslaw & J. C. Jaeger; Oxford Clarendon Press (1959), 2nd edition, 510 pp.

Introduction to Geophysical Fluid Dynamics Physical and Numerical Aspects

B. Cushman-Roisin and J.-M. Becker; Academic Press (2011), 2nd edition, 828 pp.

Dynamical Oceanography

H.A. Dijkstra; Springer-Verlag (2008), 407 pp.

Indian Ocean Oceanographic and Meteorological Data

Koninklijk Nederlands Meteorologisch Instituut. Royal Netherlands Meteorological Institute (1952), De Bilt, Netherlands, 2nd edition, number 135.

Ocean Circulation and Climate: A 21 Century Perspective

G. Siedler, S.M. Griffies, J. Gould & J.A. Church; Academic Press (2013), 904 pp.

Variability of the Mozambique Channel Throughflow

P. van der Werf; Institute for Marine and Atmospheric Research Utrecht, Faculty of Science, Department of Physics, Utrecht University, the Netherlands (2009), Doctoral Thesis. Available [online](#). ISBN 978-30-393-5251-9

Oceanographic Atlas of the International Indian Ocean Expedition

K. Wyrtki. National Science Foundation (1971), CRC Press, Reprint edition, 542 pp.

Articles

Seasonal Variation of the South Indian Tropical Gyre and the Indonesian Throughflow Front

B. Aguiar-González, L. Ponsoni, H. Ridderinkhof, H.M. van Aken, W.P.M. de Ruijter & L.R.M. Maas; Deep-Sea Research Part I, Vol. 110 (2016), 123-140. DOI: 10.1016/j.dsr.2016.02.004

ETOPO1 1 Arc-Minute Global Relief Model: Procedures, Data Sources and Analysis

C. Amante & B.W. Eakins; National Geophysical Data Center, Marine Geology and Geophysics Division, Boulder, Colorado, March 2009

Documentation of a Highly ENSO-Related SST Region in the Equatorial Pacific

A.G. Barnston, M. Cheliah & S.B. Goldenberg; Atmosphere-Ocean, Vol. 35 (3) (1997), 367-383. DOI: 10.1080/07055900.1997.9649597

Impact of the Indonesian Throughflow on Agulhas Leakage

D. Le Bars, H.A. Dijkstra & W.P.M. de Ruijter; Ocean Science, Vol. 9 (2013), 773-785. DOI: 10.5194/os-9-773-2013

On the Role of the Agulhas System in Ocean Circulation and Climate

L.M. Beal, W.P.M. De Ruijter, A. Biastoch, R. Zahn & SCOR/WCRP/IAPSO Working Group 136; Nature, Vol 472 (2011), 429-436. DOI: 10.1038/nature09983

Sea Level Variations at Tropical Pacific Islands Since 1950

M. Becker, B. Meyssignac, C. Letetrel, W. Llovel, A. Cazenave & T. Delcroix; Global and Planetary Change, Vol. 80-81 (2012), 85-98. DOI: 10.1016/j.gloplacha.2011.09.004

ERA Report Series 1 The ERA-Interim Archive Version 2.0

P., Berrisford, D. Dee, P. Poli, R., Brugge, K. Fielding, M. Fuentes, P. Källberg, S. Kobayashi, S. Uppala & A. Simmons; European Centre for Medium Range Weather Forecasts, Shinfield Park, Reading, Berkshire RG 9AX, United Kingdom (2011)

Diagnostic Model and Analysis of the Surface Currents in the Tropical Pacific Ocean

F. Bonjean & G.S.E. Lagerloef; Journal of Physical Oceanography, Vol. 32 (2002), 2938-2954. DOI: 10.1175/1520-0485(2002)032<2938:DMAAOT>2.0.CO;2

Control of Salinity on the Mixed Layer Depth in the World Ocean: 1. General description
C. de Boyer Montégut, J. Mignot, A. Lazar & S. Cravatte; Journal of Geophysical Research, Vol. 112 (2007), C06011. DOI:10.1029/2006JC003953

ARGO Profiles a Rare Occurrence of Three Consecutive Positive Indian ocean Dipole Events 2006-2008

W. Cai, A. Pan, D. Roemmich, T. Cowan, and X. Guo; Geophysical Research Letters, Vol. (2009) 36, L08701, doi:10.1029/2008GL037038

Projected Response of the Indian Ocean Dipole to Greenhouse Warming

W. Cai, X.-T. Zheng, E. Weller, M. Collins, T. Cowan, M. Lengaigne, W. Yu & T. Yamagata; Nature Geoscience, Vol. 6 (2013), 999-1007. DOI: 10.1038/NGEO2009

Volume Transport and Property Distributions of the Mozambique Channel

S.F. DiMarco, P. Chapman, W.D. Nowlin Jr., P. Hacker, K. Donohue, M. Luther, G.C. Johnson & J. Toole; Deep Sea Research II, Vol. 49 (2012), 1481-1511. DOI: 10.1016/S0967-0645(01)00159-X

Vertical Structure of Kelvin Waves in the Indonesian Throughflow Exit Passages

K. Drushka, J. Sprintall, S.T. Gille & I. Brodjonegoro; Journal of Physical Oceanography, Vol. 40 (2010), 1965-1987. DOI: 10.1175/2010JPO4380.1

Decadal Trends of the Upper Ocean Salinity in the Tropical Indo-Pacific Since Mid-1990s

Y. Du, Y. Zhang, M. Feng, T. Wang, N. Zhang & S. Wijffels; Nature: Scientific Reports, (2015), 5:16050. DOI: 10.1038/srep16050

Intraseasonal Variability in the South Equatorial Current of the East Indian Ocean

M. Feng & S. Wijffels; American Meteorology Society, Vol. 32 (2002), Issue 1, 265-277. DOI: 10.1175/1520-0485(2002)032<0265:IVITSE>2.0.CO;2

Impact of Indian Ocean Dipole and El Niño/Southern Oscillation Wind-Forcing on the Wyrтки Jets

C. Gnanaseelan, A. Deshpande, & M.J. McPhaden²; Journal of Geophysical Research, Vol 117 (2012), C08005. DOI: 10.1029/2012JC007918

Sverdrup Model of the Depth-Integrated Flow for the World Ocean Allowing for Island Circulations

J.S. Godfrey; Geophysical Astrophysical Fluid Dynamics, Vol. 45 (1989), pp. 89-112. DOI: 10.1080/03091928908208894

Makassar Strait Throughflow, 2004 to 2006

A.L. Gordon, R.D. Susanto, A. Ffield, B.A. Huber, W. Pranowo & S. Wirasantosa; Geophysical Research Letters, VOL. 35 (2008), L24605. DOI: 10.1029/2008GL036372

South China Sea Throughflow Impact on the Indonesian Throughflow

A.L. Gordon, B.A. Huber, E.J. Metzger, R.D. Susanto, H.E. Hurlburt, & T.R. Adi; Geophysical Research Letters, Vol. 39 (2012), L11602. DOI: 10.1029/2012GL052021

Monitoring the Indonesian Throughflow in Makassar Strait

A.L. Gordon & B. Huber; FY 2013 Annual Report, Lamont-Doherty Earth Observatory of Columbia University, Palisades, NY (2013), 9 pp.

Madden Julian Oscillation (MJO)

J. Gottschalck, V. Kousky, W. Higgins & M. L'Heureux; US National Weather Service, undated (available [online](#), visited on 15 June, 2016)

Argo Profiling Floats Bring New Era of In Situ Ocean Observations

J. Gould, S. Wijffels, H. Freeland, M. Ignaszewsky, X. Jianping, S. Pouliquen, Y. Desaubies, U. Send, K. Radhakrishnan, K. Takeuchi, K. Kom, M. Danchenkov, P. Sutton, B. King, B. Owens, S. Riser; Eos Earth and Space Science New, Vol. 85, No. 19 (2004), Pages 179 and 190–191. DOI: 10.1029/2004EO190002

Cruise Report LOCO-IW03 cruise LOCO03-Canary Basin R.V. Pelagia cruise 64PE208 06-19 March, 2003

H. van Haren; NIOZ, 30 pp., available [online](#)

Long-Term Observations of Transport, Eddies, and Rossby Waves in the Mozambique Channel

U. Harlander, H. Ridderinkhof, M.W. Schouten & W.P.M. de Ruijter; Journal of Geophysical Research, Vol. 114 (2009), C02003. DOI:10.1029/2008JC004846

Oceanic Precondition and Evolution of the 2006 IOD

T. Horii, H. Hase, I. Ueki, & Y. Masumoto; Geophysical Research Letters, Vol. 35 (2008), L03607. DOI: 10.1029/2007GL032464

Role of Equatorial Oceanic Waves on the Activation of the 2006 Indian Ocean Dipole

I. Iskandar; Institut Teknologi Bandung (ITB) Journal of Science, Vol. 44 A, No. 2 (2012), 113-128. DOI: 10.5614/itbj.sci.2012.44.2.2

Remote Sensing Using GNSS Signals: Current Status and Future Directions

S. Jin, G.P. Feng & S. Gleason; Advances in Space Research, 47 (2011), 1645–1653. DOI: 10.1016/j.asr.2011.01.036

Validation and Error Analysis of OSCAR Sea Surface Currents

E.S. Johnson, F. Bonjean, G.S.E. Lagerloef, J.T. Gunn & G.T. Mitchum; Journal of Atmospheric and Oceanic Technology, Vol. 24 (2007), 688-701. DOI: 10.1175/JTECH1971.1

Weakening of Spring Wyrтки Jets in the Indian Ocean During 2006–2011

S.S. Joseph, A.J. Wallcraft, T.G. Jensen, M. Ravichandran, S.S.C. Shenoi & S. Nayak; Journal of Geophysical Research, Vol 117 (2012), C04012. DOI: 10.1029/2011JC007581

Notes and Correspondence on Sverdrup Discontinuities and Vortices in the Southwest Indian Ocean

J.H. LaCasce & P.E. Isachsen; Journal of Physical Oceanography, Vol. 37 (2007), 2940-2950. DOI: 10.1175/2007JPO3652.1

The Current Status of the Real-Time In Situ Global Ocean Observing System For Operational Oceanography

D.M. Legler, H.J. Freeland, R. Lumpkin, G. Ball, M.J. McPhaden, S. North, R. Crowley, G.J. Goni, U. Send & M.A. Merrifield; *Journal of Operational Oceanography*, 8:sup2 (2015), s189-s200. DOI: 10.1080/1755876X.2015.1049883

OurOcean – An Integrated Solution to Ocean Monitoring and Forecasting

P. Li, Y. Chao, Q. Vu, L. Zhijin, J. Farrara, H. Zhang & X. Wang; *Oceans* (2006), 1-6. DOI: 10.1109/OCEANS.2006.306858

Regional and Interannual Variability in Sea Level Over 2002-2009 Based on Satellite Altimetry, Argo Float Data and GRACE Ocean Mass

W. Llovel, S. Guinehut & A. Cazenave; *Ocean Dynamics*, Vol. 60 (2010), 1193-1204. DOI: 10.1007/s10236-010-0324-0

Successful Prediction of the Consecutive IOD in 2006 and 2007

J.-J. Luo, S. Behera, Y. Masumoto, H. Sakuma & T. Yamagata; *Geophysical Research Letters*, Vol. 35, Issue 14 (2008), L14S02. DOI: 10.1029/2007GL032793

Volume Transports of the Wyrтки jets and Their Relationship to the Indian Ocean Dipole

M.J. McPhaden, Y. Wang & M. Ravichandran; *Journal of Geophysical Research: Oceans*, Vol. 120, Issue 8 (2015), 5302-5317. DOI: 10.1002/2015JC010901

Control of Salinity on the Mixed Layer Depth in the World Ocean: 2. Tropical Areas

J. Mignot, C. de Boyer Montégut, A. Lazar & S. Cravatte; *Journal of Geophysical Research*, Vol.112 (2007) C10010. DOI:10.1029/2006JC003954

A Wake Due to the Maldives in the Eastward Wyrтки Jet

M. Nagura & Y. Masumoto; *Journal of Physical Oceanography*, Vol. 45 (2015), 1858-1876. DOI: 10.1175/JPO-D-14-0191.1

2-Minute Gridded Global Relief Data (ETOPO2) v2

National Geophysical Data Center, 2006. 2-minute Gridded Global Relief Data (ETOPO2) v2. National Geophysical Data Center, NOAA. DOI:10.7289/V5J1012Q [September 2016 – July 2016] [[website](#)].

Coupled Ocean-Atmosphere Models

J.C.J. Nihoul; Elsevier Oceanographic Series 40, University of Liège, B5 Sart Tilman, B-4000 Liège, Belgium (1985), 767 pp.

A Link Between Low-Frequency Mesoscale Eddy Variability Around Madagascar and the Large-Scale Indian Ocean Variability

V. Palastanga, P.J. van Leeuwen & W.P.M. de Ruijter; *Journal of Geophysical Research*, Vol. 111 (2006), C09029. DOI: 10.1029/2005JC00381

Circulation Around Islands and Ridges

J. Pedlosky, L.J. Pratt, M.A. Spall & K.R. Helfrich; *Journal of Marine Research*, Vol. 55 (1997), 1199-1251. DOI: 10.1357/0022240973224085

Intraseasonal Kelvin Wave in Makassar Strait

K. Pujiana, A.L. Gordon & J. Sprintall; Journal of Geophysical Research: Oceans, Vol. 118 (2013), 2023–2034; DOI: 10.1002/jgrc.20069

Intraseasonal Variability in the Makassar Strait Thermocline

K. Pujiana, A.L. Gordon, J. Sprintall & D. Susanto; Journal of Marine Research, 67 (2009), 757–777. DOI: 10.1357/002224009792006115

ARGO Profiles Variability of Barrier Layer in the Tropical Indian Ocean and its Relationship with the Indian Ocean Dipole

Y. Qiu, W. Cai, L. Li, & X. Guo; Geophysical Research Letters, Vol. 39 (2012), L08605. DOI: 10.1029/2012GL051441

Buffering Effect and Its Related Ocean Dynamics in the Indonesian Throughflow Region

T. Qu, Y. Du, J.P. McCreary Jr., G. Meyers & T. Yamagata; Journal of Physical Oceanography, Vol. 38 (2007), 503–516. DOI: 10.1175/2007JPO3759.1

Generation and Termination of Indian Ocean Dipole Events in 2003, 2006 and 2007

S.A. Rao, J.-J. Luo, S.K. Behera & T. Yamagata; Climate Dynamics, Vol. 33 (2008), 751–767; DOI: 10.1007/s00382-008-0498-z

Observational Evidence for a Southern Hemisphere Oceanic Supergyre

K.R. Ridgway & J.R. Dun; Geophysical Research Letters, Vol. 34, L13612 (2007), DOI: 10.1029/2007GL030392

A Real-Time Global Sea Surface Temperature Analysis

R.W. Reynolds; Journal of Climate, Vol. 1 (1988), 75–86. DOI: 10.1175/1520-0442(1988)001<0075:ARTGSS>2.0.CO;2

An Improved In Situ and Satellite SST Analysis for Climate

R.W. Reynolds, N.A. Rayner, T.M. Smith, D.C. Stokes & W. Wang; Journal of Climate, Vol. 15 (2002), 1609–1625. DOI:

Seasonal and Interannual Variability in the Mozambique Channel From Moored Current Observations

H. Ridderinkhof, P.M. van der Werf, J.E. Ullgren, H.M. van Aken, P.J. van Leeuwen, & W.P.M. de Ruijter; Journal of Geophysical Research, Vol. 115 (2010), C06010. DOI: 10.1029/2009JC005619

Asymptotic Analysis of the Agulhas and Brazil Current Systems

W.P.M. de Ruijter; Journal of Physical Oceanography, Vol. 12 (1982), 361–373. DOI: 10.1175/1520-0485(1982)012<0361:AAOTAA>2.0.CO;2

Observations of the Flow in the Mozambique Channel

W.P.M. de Ruijter, H. Ridderinkhof, J.R.E. Lutjeharms, M.W. Schouten & C. Veth; Geophysical Research Letters, Vol. 29, No. 10, 1502 (2002). DOI: 10.1029/2001GL013714

Observations of the Inter-Ocean Exchange Around South Africa

W.P.M. de Ruijter, G.-J.A. Brummers, S.S. Drijfhout, J.R.E. Lutjeharms, F. Peters, H. Ridderinkhof & H. van Aken; *Eos Earth and Space Science*, Vol. 87, No. 9 (2006), Pages 97, 99 and 101. DOI: 10.1029/2006EO090002

A Dipole Mode in the tropical Indian Ocean

N.H. Saji, B.N. Goswami, P.N. Vinayachandran & T. Yamagata; *Nature*, Vol. 40 (1999), 360-363. DOI: 10.1038/43854

Eddy-resolving Ocean Circulation in the Asian–Australian Region Inferred From an Ocean Reanalysis Effort

A. Schiller, P.R. Oke, G. Brassington, M. Entel, R. Fiedler, D.A. Griffin, J.V. Mansbridge; *Progress in Oceanography*, 76 (2008) 334–365. DOI: 10.1016/j.pocean.2008.01.003

Pathways of Intraseasonal Variability in the Indonesian Throughflow Region

A. Schiller, S.E. Wijffels, J. Sprintall, R. Molcard, P.R. Oke; *Dynamics of Atmospheres and Oceans*, 50 (2010), 174–200. DOI: 10.1016/j.dynatmoce.2010.02.003

Seasonal Variation of the Indonesian Throughflow in Makassar Strait

T. Shinoda, W. Han, E.J. Metzger & H. E. Hurlburt; *Journal of Physical Oceanography*, Vol. 42 (2012), 1099-1123. DOI: 10.1175/JPO-D-11-0120.1

Wind- and Buoyancy-Forced Upper Ocean Circulation in Two-Strait Marginal Seas With Application to the Japan/East Sea

M.A. Spall; *Journal of Geophysical Research*, Vol. 107, No. C1 (2002). DOI: 10.1029/2001JC000966

INSTANT: A New International Array to Measure the Indonesian Throughflow

J. Sprintall, S. Wijffels, A.L. Gordon, A. Ffield, R. Molcard, R.D. Susanto, I. Soesilo, J. Sopaheluwakan, Y. Surachman & H.M. van Aken; *Eos Earth and Space Science*, Vol. 85, No. 39 (2004), Pages 369 - 376. DOI: 10.1029/2004EO390002

SSALTO/DUACS User Handbook: (M)SLA and (M)ADT Near-Real Time and Delayed Time Products

SSALTO/DUACS User Handbook (CNES, 2015); Reference: CLS-DOS-NT-06-034, Nomenclature: SALP-MU-P-EA-21065CLS, Issue: 4rev 4

Evaluation of the CMCC Eddy-Permitting Global Ocean Physical Reanalysis System (C-GLORES, 1982–2012) and its Assimilation Components

A. Storto, S. Masina & A. Navarra; *Quarterly Journal of the Royal Meteorological Society*, 142 (2016), 738–758. DOI:10.1002/qj.2673

Distance Between Points on the Earth's Surface

D. Surowski; Kansas State University (brought online in 2011). Available [online](#)

Variability of Indonesian Throughflow within Makassar Strait, 2004–2009

R.D. Susanto, A. Ffield, A.L. Gordon & T.R. Adi; *Journal of Geophysical Research*, Vol. 117 (2012), C09013. DOI: 10.1029/2012/JC008096

ITF Proxy from Satellite Altimeters and Gravimeters

R.D. Susanto & Y.T. Song; Journal of Geophysical Research: Oceans, Vol. 120, Issue 4 (2015), 2844-2855. DOI: 10.1002/2014JC010382

From Satellite Altimetry to Argo and Operational Oceanography: Three Revolutions in Oceanography

P.Y. Le Traon; Ocean Science, 9 (2013), 901–915. DOI: 10.5194/os-9-901-2013

In Situ Measured Current Structures of the Eddy Field in the Mozambique Channel

J.F. TERNON, M.J. Roberts, T. Morris, L. Hancke & B. Backeberg; Deep-Sea Research II, 100 (2014), 10–26. DOI: 10.1016/j.dsr2.2013.10.013

Transport Weighted Temperature and Internal Energy Transport of the Indonesian Throughflow

D. Tillinger & A.L. Gordon; Dynamics of Atmosphere and Oceans, Vol. 50 (2010), 224-232. DOI: 10.1016/j.dynatmoce.2010.01.002

The Hydrography of the Mozambique Channel From Six Years of Continuous Temperature, Salinity, and Velocity Observations

J.E. Ullgren, H.M. van Aken, H. Ridderinkhof, W.P.M. de Ruijter; Deep-Sea Research I, 69 (2012), 36–50. DOI: 10.1016/j.dsr.2012.07.003

First and Second Baroclinic Mode Responses of the Tropical Indian Ocean to Interannual Equatorial Wind Anomalies

V. Valsala; Journal of Oceanography, Vol. 64 (2008), 479-494. DOI: 10.1007/s10872-008-0041-1

Possible Interannual to Interdecadal Variabilities of the Indonesian Throughflow Water Pathways in the Indian Ocean

V. Valsala, S. Maksyutov & R. Murtugudde; Journal of Geophysical Research, Vol. 115 (2010), C10016. DOI: 10.1029/2009JC005735

Effects of Drake Passage on a Strongly Eddying Global Ocean

J.P. Viebahn, A.S. von der Heydt, D. Le Bars & H.A. Dijkstra; Paleoceanography, Vol. 31, Issue 5 (2016), 564-581. DOI: 10.1002/2015PA002888.

Indian Ocean Response to Anomalous Conditions in 2006

P.N. Vinayachandran, J. Kurian & C.P. Neema; Geophysical Research Letters, Vol. 34 (2007), L15602. DOI: 10.1029/2007GL030194

The Circulation of the Depth-Integrated Flow Around an Island With Application to Indonesian Throughflow

R.C. Wajswicz; Journal of Physical Oceanography, Vol. 23 (1992), 1470-1484. DOI: 10.1175/1520-0485(1993)023<1470:TCOTDI>2.0.CO;2

A dynamical ocean feedback mechanism for the Madden–Julian Oscillation

B.G.M. Webber, A.J. Matthews & K.J. Heywood; Quarterly Journal of the Royal Meteorological Society, Vol 136 (2010, Part A), 740–754. DOI:10.1002/qj.604

Impact of Interbasin Exchange on the Atlantic Overturning Circulation

W. Weijer, W.P.M. de Ruijter, H.A. Dijkstra & P.J. van Leeuwen; Journal of Physical Oceanography, Vol. 29 (1999), 2265–2284. DOI: 10.1175/1520-0485(1999)029<2266:IOIEOT>2.0.CO;2

Observation and Origin of an Interannual Salinity Anomaly in the Mozambique Channel

P.M. van der Werf, M.W. Schouten, P.J. van Leeuwen, H. Ridderinkhof & W.P.M. de Ruijter; Journal of Geophysical Research, Vol. 114 (2009), C03017. DOI: 10.1029/2008JC004911

An All-Season Real-Time Multivariate MJO Index: Development of an Index for Monitoring and Prediction

M.C. Wheeler & H.H. Hendon; American Meteorological Society, Vol. 132 (2004), 1917–1932. DOI: 10.1175/1520-0493(2004)132<1917:AARMMI>2.0.CO;2

Observations of the Madden Julian Oscillation During Indian Ocean Dipole Events

E.A. Wilson, A.L. Gordon & D. Kim; Journal of Geophysical Research, Vol. 118 (2013), 2588–2599. DOI: 10.1002/jgrd.50241

Influences of the Madden Julian Oscillations on Temperature and Precipitation in North America during ENSO-Neutral and Weak ENSO Winters

Y. Xue, W. Higgins & V. Kousky; *Proceedings of a Workshop on Prospects for Improved Forecasts of Weather and Short-Term Climate Variability on Subseasonal (2 Week to 2 Month) Time Scales*, Mitchellville, MD, NASA, 4 pp. (2002)

The Kelvin Wave Processes in the Equatorial Indian Ocean During the 2006–2008 IOD Events

D. Yan, L. Kai, Z. Wei & Y. Wei-Dong; Atmospheric and Oceanic Science Letters, Vol. 5, No. 4 (2012), 324–328. DOI: 10.1080/16742834.2012.11447007

Assessment of Composite Global Sampling: Sea Surface Wind Speed

H.-M. Zhang, J. J. Bates & R.W. Reynolds; *Geophysical Research Letters*, Vol. 33, L17714 (2006a); DOI: 10.1029/2006GL027086

Blended and Gridded High Resolution Global Sea Surface Wind Speed and Climatology From Multiple Satellites: 1987–Present.

H.-M. Zhang, R.W. Reynolds & J.G. Bates; *14th Conference on Satellite Meteorology and Oceanography*, Atlanta, GA, American Meteorological Society, Paper 100004 (2006b). Available [online](#)